# Impact of Satellite Fragmentations in GEO Graveyard Orbits

MSc Thesis

L. Roelen

August 9, 2016

Delft University of Technology

TU Delft Delft University of Technology

Challenge the future

# IMPACT OF SATELLITE FRAGMENTATIONS IN GEO GRAVEYARD ORBITS

MSc THESIS

by

**L. Roelen**

in partial fulfilment of the requirements for the degree of

**Master of Science**
in Aerospace Engineering

at Delft University of Technology
to be defended publicly on Friday August 26, 2016 at 14:00.

| | | |
|---|---|---|
| Supervisor: | ir. R. Noomen | |
| Thesis committee: | Prof. dr. ir. P. N. A. M. Visser, | TU Delft |
| | Ir. R. Noomen, | TU Delft |
| | Ir. P. P. Sundaramoorthy, | TU Delft |

An electronic version of this thesis is available at `http://repository.tudelft.nl/`.

TU Delft Delft University of Technology

# PREFACE

This report describes the work done for the thesis project (AE5810, 42 ECTS) of the Aerospace Engineering Master with the profile Space Exploration at Delft University of Technology. This thesis deals with the problem of space debris in the geostationary orbit. More specifically, it investigates the behaviour of debris from satellite fragmentations in GEO graveyard orbits and risk to active geostationary satellites. The work mainly consisted of developing a simulation program, using this to simulate various fragmentation scenarios and analysing the results. In preparation for this thesis a literature study was performed, the report of which contains more background information on the models used in the simulation software and the reasons why certain models were chosen (Roelen, 2015).

I would like to express my gratitude to my thesis supervisor Ron Noomen, for his useful advice and guidance during our weekly meetings throughout the project. I would also like to thank my fellow students on the $9^{th}$ floor of our faculty, since working amongst them helped me to be more motivated during the beginning of my thesis, when I was still figuring out how to program the simulation software.

Liselot Roelen

Delft, August 9, 2016

# ABSTRACT

At their end of life, geostationary satellites are moved to a graveyard orbit about 300 km above the geostationary orbit (GEO), to prevent them from being able to collide with active GEO satellites. Although this graveyard orbit appears to be a safe location for obsolete spacecraft, if satellite fragmentations (due to explosions or collisions) would occur in the graveyard orbit, fragments can be produced that are able to cross the geostationary orbit and pose a threat to operational satellites. These fragments can have higher area-to-mass ratios than satellites, which makes their eccentricities vary more due to solar radiation pressure. In addition to velocity changes due to a fragmentation, this can cause such fragments to eventually cross the geostationary orbit. This thesis investigates the risk of such occurrences and also investigates whether alternative graveyard orbits could more effectively keep debris from fragmentations away from GEO.

To perform the research a C++ program was developed to simulate explosions and collisions and propagate the fragments over a long period of time. For the simulation of fragmentations the NASA standard satellite breakup model was used, along with a $\Delta V$ distribution modification for low-velocity collisions which are typical to GEO. For the orbit propagation an averaged orbit dynamics model based on Milankovitch orbital elements was used. This model allows for very fast computation while still providing sufficiently accurate results. The program is able to propagate the orbit of a single fragment over a 100-year period within 5 seconds of computation time, while the simulation of a fragmentation and propagation of about 2000 fragments takes between 1.5 and 2 hours. Throughout the propagation, GEO crossings by the fragments are computed, which are defined as fragments passing within 50 km of GEO.

The fragmentation simulation includes generation of random number for some of the fragments' characteristics, which affects the mass, area-to-mass ratio (AMR) and $\Delta V$ of the fragments. Because of this, each simulation will be different if a different seed number is used in the random number generator. After several runs, the resulting total masses of the fragments turned out to be very inconsistent. Masses varied from 850 to 1300 kg for explosions and 1000 to 1600 kg for collisions, while a 1000 kg mass was intended. These variations are mostly due to fragments larger than 1 m, which are not accurately modelled by the AMR distribution. These fragments are therefore excluded from simulations. Only fragments between 1 cm and 1 m are considered.

A standard explosion and collision case with a graveyard orbit 300 km above GEO were investigated. The explosion simulation resulted in a total of 24424 fragments between 1 cm and 1 m, which made 6.24E7 GEO crossings over a 100-year period. In the collision simulation 46756 fragments were produced and the total number of GEO crossings was 17.0E7. A sensitivity analysis was performed as well, where input parameters were changes from the standard cases and the results compared to each other. For explosions, the most important parameters were ones that affect the initial velocity direction. For example if the inclination was changed from 0 to 15° weighted crossings were reduced by about 20%. Changing the initial date by 3 months caused a relatively large difference of 22% in the total number of crossings. For collisions the collision velocity is very important. In the graveyard orbit a maximum collision velocity of about 810 m/s is possible, while any velocity over 283 m/s results in a catastrophic collision where the entire satellite is fragmented.

Different potential graveyard orbits were compared to each other, mainly by comparing the number of GEO crossings by fragments. Higher-altitude graveyard orbits were found to greatly reduce the number of crossings. When a graveyard orbit 2000 km above GEO is used, this reduces crossings by explosion fragments by 83% compared to the standard case. Crossings by collision fragments are reduced by 95%. However a significantly higher $\Delta V$ would be required to bring a satellite to a higher orbit, which may not be practically feasible as it would take away from the orbit maintenance $\Delta V$ and reduce the operational lifetime of a satellite. Based on the results a new graveyard orbit at 1000 km above GEO is recommended. This still reduces crossings by 61 and 78%, while it is not as expensive as the 2000 km option. However further research is recommended, to investigate the long-term effects of using such an alternative graveyard orbit on the evolution of the GEO debris population and on the risk that an active satellite is critically damaged by debris.

# CONTENTS

# LIST OF ABBREVIATIONS

| Abbreviation | Meaning |
|---|---|
| AMR | Area-to-mass ratio |
| CARDC-SBM | China Aerodynamics Research and Development Center - Spacecraft Breakup Model |
| CFRP | Carbon fibre reinforced plastic |
| CT | Correlated targets |
| DELTA | Debris Environment Long-Term Analysis |
| ESA | European Space Agency |
| GEO | Geostationary Earth orbit |
| GFRP | Glass fibre reinforced plastic |
| HAMR | High area-to-mass ratio |
| LEO | Low Earth orbit |
| MODEST | Michigan Orbital Debris Survey Telescope |
| NASA | National Aeronautics and Space Administration |
| RAAN | Right ascension of the ascending node |
| RNG | Random number generator |
| RK | Runge-Kutta |
| SRP | Solar radiation pressure |
| Tudat | TU Delft Astrodynamics Toolbox |
| TU Delft | Delft University of Technology |
| UCT | Uncorrelated targets |

# LIST OF SYMBOLS

Table 1: Latin Symbols

| Symbol | Parameter | Unit |
|---|---|---|
| $a$ | semi-major axis | m |
| $\boldsymbol{a}$ | acceleration by perturbations vector | $m/s^2$ |
| $A$ | cross-sectional area | $m^2$ |
| $A/M$ | area-to-mass ratio | $m^2/kg$ |
| $\boldsymbol{b}$ | Laplace vector | $m^3/s^2$ |
| $C$ | dimensional gravity field coefficient | $m^2$ |
| $C_R$ | reflectivity | - |
| $d$ | fragment diameter | m |
| $\boldsymbol{d}$ | position vector relative to Earth | m |
| $\boldsymbol{d_e}$ | position vector of Earth relative to Sun | m |
| $e$ | eccentricity | - |
| $\boldsymbol{e}$ | eccentricity vector | - |
| $E$ | eccentric anomaly | rad |
| $\boldsymbol{F}$ | solar radiation pressure force vector | N |
| $h$ | scaled angular momentum | – |
| $\boldsymbol{h}$ | scaled angular momentum vector | – |
| $H$ | angular momentum | $m^2/s$ |
| $\boldsymbol{H}$ | angular momentum vector | $m^2/s$ |
| $i$ | inclination | rad |
| $J$ | dimensionless gravity field coefficient | - |
| $l$ | mean longitude | rad |
| $L$ | true longitude | rad |
| $L_c$ | characteristic length of a fragment | m |
| $M$ | mean anomaly | rad |
| $m$ | mass of a fragment from an explosion or collision | kg |
| $m_e$ | ejected mass from a collision | kg |
| $m_{proj}$ | collision projectile mass | kg |
| $m_{tar}$ | collision target mass | kg |
| $m_t$ | total mass of fragments from a collision | kg |
| $n$ | mean motion | rad/s |
| $N$ | number of fragments | - |
| $N$ | normal distribution function | |
| $\hat{\boldsymbol{p}}$ | vector aligned with Earth's rotation pole | - |
| $r$ | radial distance from central body to satellite | m |
| $r_L$ | Laplace radius | m |
| $S$ | scaling factor used in fragment size distribution | - |
| $t$ | time | s |
| $T_s$ | Earth's orbital period | s |
| $\boldsymbol{v}$ | velocity vector | m/s |
| $v$ | collision velocity | m/s |

Table 2: Greek Symbols

| Symbol | Parameter | Unit |
|---|---|---|
| $\Delta V$ | velocity change | m/s |
| $\epsilon$ | angle between equatorial plane and ecliptic plane | rad |
| $\theta$ | true anomaly | rad |
| $\Lambda$ | SRP Perturbation angle | rad |
| $\mu$ | gravitational parameter | $m^3/s^2$ |
| $\mu$ | mean of normal distribution | - |
| $\rho$ | reflectivity | - |
| $\sigma$ | standard deviation of normal distribution | - |
| $\Upsilon$ | Vernal Equinox | - |
| $\phi$ | angle between Laplace plane and equatorial plane | rad |
| $\omega$ | argument of perigee | rad |
| $\bar{\omega}$ | longitude of perigee | rad |
| $\Omega$ | right ascension of ascending node | rad |

Table 3: Subscripts and notations

| Symbol | Definition |
|---|---|
| $\square_2$ | $J_2$, oblateness gravity field coefficient |
| $\square_{2,2}$ | $J_{2,2}$, ellipticity gravity field coefficient |
| $\square_3$ | $J_3$ gravity field coefficient |
| $\square_{A/M}$ | area-to-mass ratio |
| $\square_e$ | Earth |
| $\square_m$ | Moon |
| $\square_p$ | perturbing body |
| $\square_s$ | Sun |
| $\square_{srp}$ | solar radiation pressure |
| $\square^{R/B}$ | upper stage |
| $\square^{S/C}$ | spacecraft |
| $\square^T$ | transpose of a matrix or vector |
| $\hat{\square}$ | unit vector |
| $\bar{\square}$ | averaged parameter |
| $\dot{\square}$ | time-derivative |

Table 4: Constants

| Symbol | Parameter | Value |
|---|---|---|
| $\mu$ | gravitational parameter of Earth | $3.986\,004\,41 \cdot 10^{14}$ $m^3/s^2$ |
| $P_{saros}$ | sidereal period of lunar nodal regression | 6788.3 days |
| $P_\Phi$ | solar constant | $1.021 \cdot 10^{17}$ kg $m/s^2$ |
| $R_e$ | mean equatorial radius of Earth | 6378.1363 km |

# 1

# INTRODUCTION

The geostationary orbit (GEO) currently contains about 427 operational satellites (more than one per degree) and is becoming more crowded over time (Johnston, 2016). Many of the satellites are commercial communications satellites, meaning there is a financial importance to keeping this orbit safe from debris as much as possible. Orbits of GEO satellites do not naturally decay over time and there is currently no feasible method to completely remove these satellites from orbit once their mission is over. To prevent accumulation of space debris from defunct satellites, guidelines have been made to dispose GEO satellites at their end-of-life into a graveyard orbit a few hundred km above GEO. In 1997 an international consensus was reached for a minimum altitude increase of 235 plus a term related to solar radiation pressure (SRP), depending on the spacecraft characteristics (Jehn et al., 2005).

For some time it had been assumed that the current guidelines on disposal orbits are sufficient to protect the geostationary ring. However later discoveries (for example by Schildknecht et al. (2004)) have shown an unexpected population of high area-to-mass (HAMR) debris, which is thought to originate from non-functional geostationary satellites. These objects are strongly affected by SRP and develop large variations in eccentricity over time, which enables them to intrude into the GEO environment even if are initially released from satellites in the graveyard orbit (Rosengren et al., 2014). HAMR objects are currently an important research topic in an effort to improve understanding of the space debris problem in GEO.

Debris from satellite fragmentations (explosions or collisions) in the GEO graveyard orbit could also pose a threat to geostationary satellites, as such events produce many fragments of varying area-to-mass ratios. These fragments might be able to intrude into the GEO environment in a way similar to HAMR debris. The purpose of this research is to quantify the risk to active GEO satellites caused by such fragments, including uncertainties therein. The main research question is: "Can debris from satellite fragmentations in the GEO graveyard orbit over time intrude into the GEO environment, thereby posing a threat to active GEO satellites?". Additionally the research investigates whether alternative graveyard orbits could be more effective at keeping such debris away from GEO. Note that the research focusses on the results of single fragmentation events, not taking into account the probability of such events occurring or effects on the long-term evolution of the entire GEO debris population. To perform the research a simulation program has been developed to simulate satellite fragmentations and propagate the orbits of the debris that is created. This report describes the work done during the project.

The structure of the report is as follows. Chapter 2 describes characteristics of space debris in and near GEO and relevant past research in this area. Chapter 3 describes the orbital dynamics model that has been used in the simulation software to propagate orbits of fragments, while Chapter 4 discusses the fragmentation model that is used to simulate the characteristics of fragments that are produced in a fragmentation event. Chapter 5 describes the simulation software and its validation, after which Chapters 6 and 7 present the results of respectively explosion and collision simulations that have been obtained. Finally Chapter 8 gives conclusions regarding the research objective and provides recommendations for further research.

# 2

# SPACE DEBRIS NEAR GEO

This chapter discusses the problem of space debris in and near GEO. Section 2.1 describes orbit characteristics of objects in and near the geostationary ring. After that, Section 2.2 elaborates on the recent discoveries of HAMR objects and the differences in their orbit evolution compared to that of intact satellites. Finally Section 2.3 discusses a possible alternative disposal orbit in the Laplace plane.

## 2.1. GEO CHARACTERISTICS

GEO is a circular orbit 35786 km above the Earth's equator, where the orbital period is equal to the rotation period of the Earth, allowing GEO satellites to stay above the same point on the Earth's surface. Orbits of uncontrolled objects (such as disposed satellites) in GEO gradually change over time due to perturbation forces, while active GEO satellites are kept in constant orbits through orbit maintenance manoeuvres. The most important perturbation forces for GEO orbits are irregularities in the Earth's gravity field, gravitational attraction by the Moon and Sun, and solar radiation pressure. Perturbations have an effect on eccentricity, changing the range of altitudes of the perturbed orbit. There are also changes in the inclination and ascending node, which define the orientation of the orbit.

### 2.1.1. ALTITUDE

Jehn et al. (2005) investigated altitude behaviour of five disposed GEO satellites in graveyard orbits by simulating their orbit evolution. The satellites' area-to-mass ratios (AMR) were estimated by assuming a reflection coefficient, $C_R$, of 1.5 and fitting a model to observational data. The AMR values varied between 0.0113 and 0.0138 $m^2$/kg. Simulations were done for AMR values of 0.01 and 0.02 $m^2$/kg. Even for the high AMR value of 0.02 $m^2$/kg the simulations showed that the altitude of the perigee always stayed at least 215 km above GEO over a 1000-year period. A plot of this simulation is given in Fig. 2.1. Based on these results the current guidelines for re-orbiting satellites at their end-of-life seem sufficient to protect the geostationary orbit. However this is not including the recently discovered HAMR objects which are discussed in Section 2.2.

### 2.1.2. ASCENDING NODE - INCLINATION OBSERVATIONS

The evolution of the right ascension of the ascending node, $\Omega$, and inclination, $i$, of uncontrolled GEO objects follows a distinct pattern which can be recognized in several observations. This is visible in Fig. 2.2, which contains observations made by MODEST, the Michigan Orbital Debris Survey Telescope (Matney et al., 2006). Fig. 2.2a uses $\Omega$ and $i$ as coordinates for the plot, while Fig. 2.2b uses a polar representation. In the polar representation $i$ is given by the radial distance from (0,0), while $\Omega$ is the counter-clockwise angle from the positive x-axis direction.

The plot shows many objects with near-zero inclination, these represent the operational GEO satellites which are kept at this inclination through orbit maintenance manoeuvres. Additionally many objects are close to the line between $(\Omega, i)$ = (90,0) and (0,15). A similar pattern can be seen on the right-hand side of the plot between (270,0) and (360,15). This pattern can also be recognized in two-line elements (TLE) data, as shown in Fig. 2.3. These kind of plots are often also made with $\Omega$ and $i$ as polar coordinates such as in Fig. 2.2b, where the objects create a circular pattern.

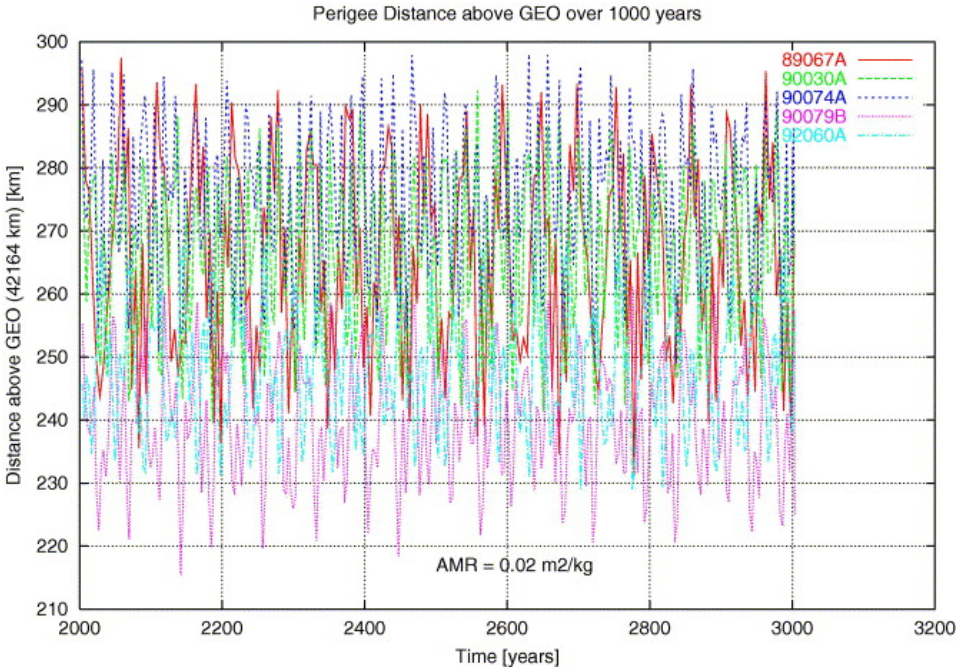


Figure 2.1: Simulation of long-term evolution of perigee altitude of the disposed GEO satellites Sirius I, Asiasat I, Thor 1, Eutelsat II F1 and Hispasat 1A with an area-mass ratio of 0.02 $m^2$/kg. Perturbation forces included were lunisolar gravitational perturbation, SRP and gravity field terms $J_{22}$, $J_{31}$, $J_{32}$, $J_{33}$, $J_{41}$ and $J_{42}$ (Jehn et al., 2005).

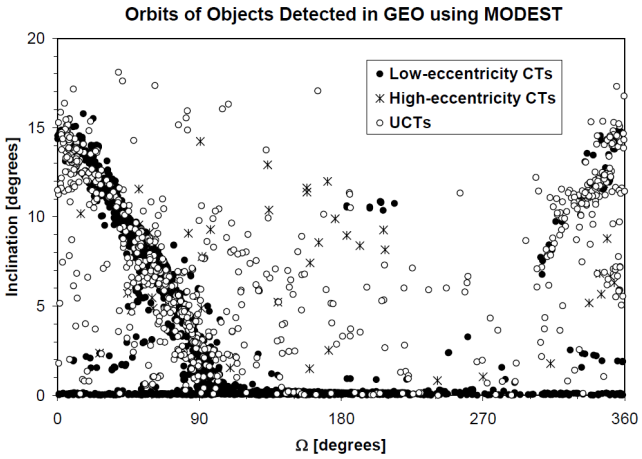


(a) RAAN-inclination plot

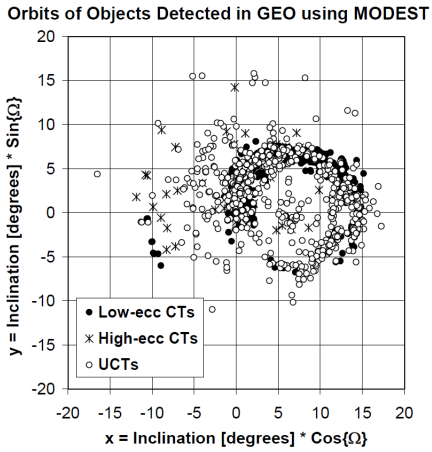


(b) Polar RAAN-inclination plot

Figure 2.2: Inclination and right ascension of ascending node of objects near GEO detected by MODEST (Matney et al., 2006). The abbreviations CT (correlated targets) and UCT (uncorrelated targets) denote correlation with tracked satellites.

### 2.1.3. PRECESSION AND THE LAPLACE PLANE

The evolution of ascending node and inclination is caused by the Earth's oblateness as well as perturbations by the gravitational forces of the Sun and Moon. The Earth's oblateness causes an orbit with a non-zero inclination to precess about the Earth's rotation axis. This is known as the $J_2$-effect, which is also very important for satellites in LEO. Gravitational forces by the Sun and Moon can cause a similar kind of precession. This is negligible in LEO, however it is very important for GEO satellites, as with increasing distance from Earth the Earth's gravity reduces and therefore third body gravitational perturbations become relatively larger. For the lunisolar perturbations though, the precession is about the poles of the orbital planes of the Sun and Moon.

The motion of the orbit pole therefore consists of precession about three separate axes. There is an equilibrium plane between the plane through the Earth's equator and the ecliptic where these average out and the precession is minimized, similar to how the equatorial plane is an equilibrium plane for precession due to $J_2$.

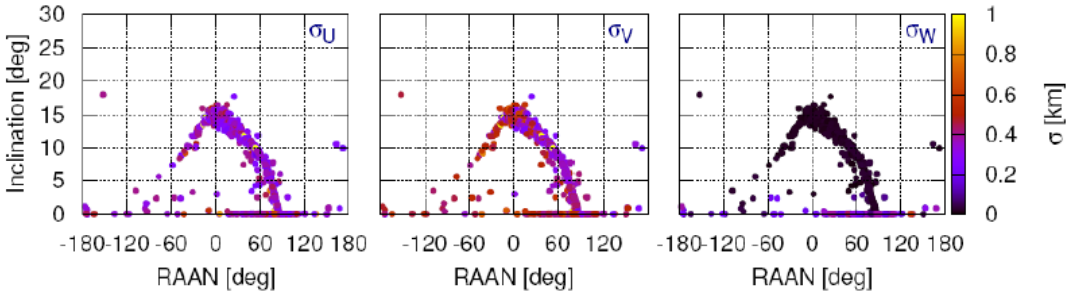


Figure 2.3: GEO objects in TLE catalog of January 1st 2008 with estimated position uncertainties (Leloux, 2012).

This plane is called the Laplace plane and its orientation is illustrated in Fig. 2.4. In this figure $\hat{\boldsymbol{h}}_L$ is the pole of the Laplace plane and $\hat{\boldsymbol{h}}$ the pole of an arbitrary orbit with small inclination with respect to the Laplace plane. Due to perturbations $\hat{\boldsymbol{h}}$ will move in a circle around $\hat{\boldsymbol{h}}_L$, similar to the circular pattern in Fig. 2.2b.

The inclination of the Laplace plane depends on a planet's characteristics and the distance to the planet's center. In the GEO region the Laplace plane is inclined at about 7.4° with respect to the equator (see also Fig. 2.8). Orbits which are inclined with respect to the Laplace plane will precess with a constant inclination about the pole of the Laplace plane. This is similar to how LEO orbits precess about the Earth's rotation pole with constant inclination relative to the equator, as for these orbits the precession effects of the Sun and Moon can be neglected. For satellites in GEO the period of precession is roughly 53 years (Rosengren et al., 2014).

This precession of the orbit pole about the Laplace pole also explains the circular pattern seen in the polar RAAN-inclination plot of Fig. 2.2b. The center of the circle is at about 7.4° inclination. Additionally, the long period of 53 years explains why in Fig. 2.2a there are less objects in the region between 270 and 360° than between 0 and 90°. These are the objects that would be in the second half of this 53-year period, and there are simply not that many satellites that have been launched into GEO that long ago.

Note that different references actually mention slightly different inclination values for the Laplace plane. Rosengren et al. (2014) use 7.2°, referring to (Allan and Cook, 1963). Friesen et al. (1993) use 7.4° and also mention that earlier they thought it was 7.3°, since some old figures in the paper still used this value. Since (Friesen et al., 1993) is the most recent original reference, this value is assumed to be the correct one and is used in this report.

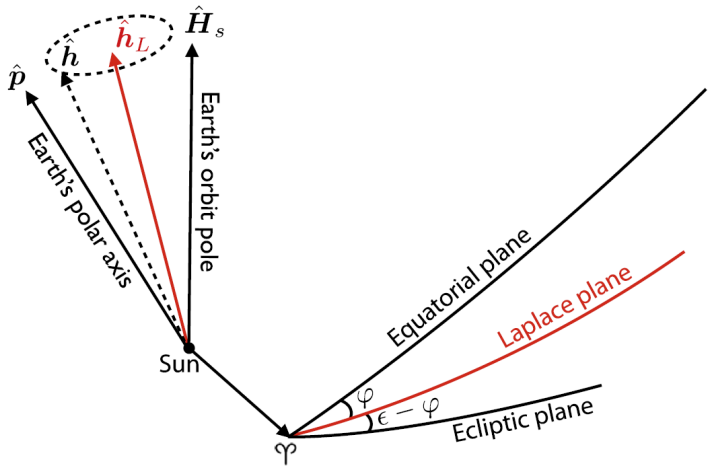


Figure 2.4: Geometry of the Laplace plane equilibrium (Rosengren et al., 2014).

### 2.1.4. EVOLUTION OF A DEBRIS CLOUD

Another interesting example showing the orbit evolution of objects near GEO is found in Pardini and Anselmo (2005), who have simulated an explosion of a satellite in GEO and propagated the resulting debris cloud. Some of their results are shown in Fig. 2.5, where the $\Omega$-$i$ motion of such a cloud of debris is plotted over a period of 72 years. These plots show a similar motion in $\Omega$-$i$ as found from actual observations and the objects also have a roughly 53-year period.

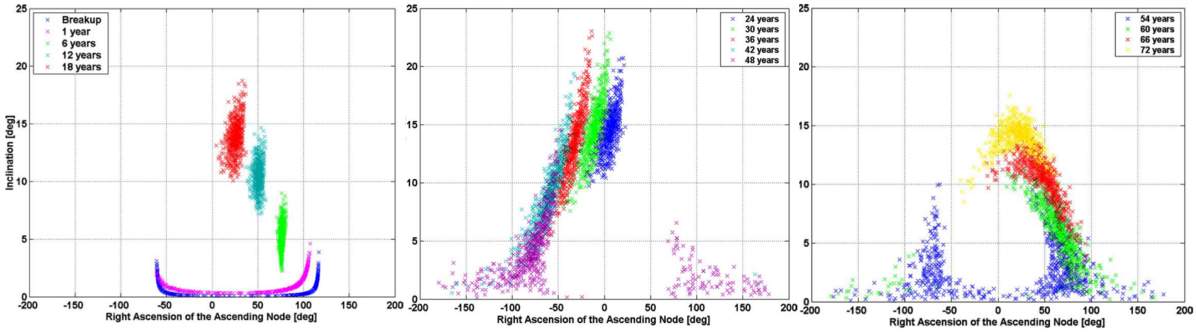


Figure 2.5: Propagation of a debris cloud resulting from fragmentation of a GEO satellite, from 0 to 18 years (left), 24 to 48 years (middle) and 54 to 72 years (right) (Pardini and Anselmo, 2005).

## 2.2. HIGH AREA-MASS RATIO OBJECTS

HAMR debris was first discovered by Schildknecht et al. (2004). SRP is the largest perturbation force for these objects, because is increases with higher AMR values, and it causes HAMR objects to develop high values of eccentricity with an approximately 1-year period, as shown in Fig. 2.6. The eccentricity evolution is shown for different values of $\Lambda$, which is the SRP perturbation angle. This parameter is sometimes used in literature to characterize HAMR objects. The parameter indicates how strongly an object is affected by SRP, with a value from 0° to at most 90°.

If GEO objects would develop an eccentricity of above 0.849, their orbit will intersect with the Earth's surface and the object will impact the Earth and be removed from orbit. This happens for objects with an SPR perturbation angle ($\Lambda$) above 29° (Rosengren and Scheeres, 2014). SRP perturbation angle is a parameter which increases for larger values of AMR, but it also takes into account other parameters, as shown in Eq. 2.1. $V_{lc}$ is the local circular velocity in m/s, $H_s$ is the specific angular momentum of the Earth's orbit around the Sun. The parameters $a$, $\mu$ and $e$ are semi-major axis, gravitational parameter and eccentricity, while the subscripts $_s$ and $_e$ denote parameters related to the Sun and Earth. $C_R$ is the reflectivity and $A/m$ the area-to-mass ratio in $m^2$/kg. $P_\Phi$ is a solar constant which equals approximately $1.021 \cdot 10^{17}$ kg m/s$^2$. In plots such as Fig. 2.6 often AMR is also used instead of $\Lambda$, since they have a similar meaning when AMR is the only parameter that is changed in the analysis.

$$\tan\Lambda = \frac{3\beta}{2V_{lc}H_s} = \frac{3\beta}{2}\sqrt{\frac{a}{\mu\mu_s a_e(1-e_e^2)}}, \qquad \beta = C_R(A/m)P_\Phi \tag{2.1}$$

HAMR debris is thought to originate from defunct satellites in the geostationary region and observed HAMR objects have apparent AMR values up to 30 $m^2$/kg, which is much higher than AMR values of intact satellites of only 0.01 to 0.02 $m^2$/kg. Orbits of HAMR debris are highly perturbed by SRP, irregularities in the Earth's gravity field and third body perturbations by the Sun and Moon (Rosengren and Scheeres, 2013).

## 2.3. THE LAPLACE PLANE AS ALTERNATIVE DISPOSAL ORBIT

The Laplace plane, introduced in Section 2.1.3, has been investigated as alternative disposal orbit. This usage was first suggested in 1992 by Friesen et al.. One of the advantages that was found is that the relative velocities of satellites in this orbit are smaller than in the conventional disposal orbit, which means that a collision between satellites in this orbit would create less debris. Since satellites have a very low AMR, their orbits will remain close to circular. The relative velocity between satellites in a disposal orbit is then mostly due to

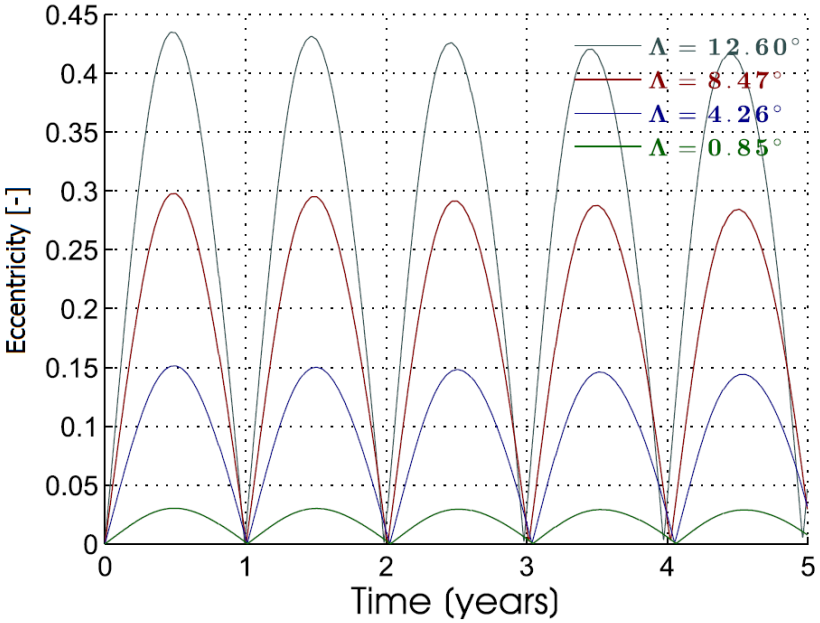


Figure 2.6: Eccentricity evolution of GEO orbit taking into account SRP, J2 and lunisolar perturbations with the Moon's orbit assumed to be in the ecliptic plane (Rosengren and Scheeres, 2013).

differences in inclination. In the conventional graveyard orbit satellites can reach inclinations between 0 and 15°, while near the Laplace plane their inclination differences would be at most 2.4°. This results in smaller relative velocities in such a Laplace disposal orbit. The inclination variations in the Laplace plane graveyard can be reduced further by slightly adjusting the initial inclination and RAAN to be in phase with lunar nodal regression as described by Friesen et al. (1993).

However for a Laplace disposal orbit, both an altitude change and inclination change would be required. The inclination change is needed to go from GEO to the Laplace plane, and the altitude change because if satellites only have a different inclination they will still cross GEO once every orbit. The inclination change is very costly in $\Delta V$: for example an altitude change of 300 km requires a $\Delta V$ of 10.9 m/s, while an inclination change of 7.4° requires 397 m/s. This makes the Laplace plane not attractive for use as a disposal orbit. However the recent discoveries of HAMR debris have renewed interest in this option.

Ignoring the required transfer and only considering the orbit evolution of debris after the transfer, Rosengren et al. (2014) investigated whether the Laplace plane would be suitable as disposal orbit to contain HAMR debris. The conventional graveyard is not capable of this because HAMR debris develops high eccentricities, but if the debris would have a different inclination in addition to the eccentricity, the chances of debris crossing GEO might be reduced. However the Laplace plane is an equilibrium plane for gravitational forces ($J_2$ and lunisolar), not including SRP which is very important for HAMR debris. This is why Rosengren et al. (2014) investigated the behaviour of objects with different $\Lambda$ values released in the Laplace plane.

In addition to strongly reduced relative encounter velocities of satellites, it was found that a Laplace disposal orbit is indeed able to keep the inclinations of HAMR debris different from the GEO inclination of 0°. Additionally, it may be possible to use an orbit at a slightly lower inclination than the Laplace plane. This would reduce the amount of required $\Delta V$ while still ensuring that objects will not go far below their initial inclination.

The orbit evolutions of HAMR objects in a conventional and Laplace disposal orbit are compared in Fig. 2.7. The evolution over time of $\Omega$ and $i$ is plotted. The left figure represents a conventional disposal orbit, where objects start at 0° inclination. As the orbits start to become inclined they will also have a right ascension of the ascending node (since RAAN has no physical meaning when inclination is 0°). For all objects $\Omega$ starts at about 90° and develops to about -90°. The inclination first increases and then goes back to zero. The maximum inclination depends on $\Lambda$. When $\Lambda$ is close to 0° the maximum is about 15°. This is in agreement with the maximum found from observations of disposed GEO satellites, which can be seen in Figs. 2.2a and

2.3. As Λ increases the maximum inclination also increases up to about 45° for a Λ of 40°.

The right figure shows a similar plot for objects with an orbit starting in the Laplace plane (the black dot). The orbit evolution is similar in that the inclination increases from the initial value up to a maximum and then comes back to the initial value. For this figure the maximum inclination also increases for higher Λ values. However the highest value is at about 38°, which is lower than that of the left figure. Also, the inclination changes for small Λ values are very small to negligible. The inclinations are always at or above 7.4°.

Rosengren et al. (2014) also investigated whether there is a different equilibrium plane for objects with higher AMR values, since they do not stay at a constant inclination when starting at 7.4°. They found that this is indeed the case and the inclination of the plane increases with higher AMR. They call this equilibrium plane the modified Laplace plane and its inclination is plotted versus semi-major axis for different AMR values in Fig. 2.8. For an AMR of 25 $m^2$/kg the modified Laplace plane inclination is 18° at GEO altitude. This plot also shows that for LEO the Laplace plane is very close to the equatorial plane, as $J_2$ is the most important perturbation force there, while with increasing distance from Earth it approaches the inclination of the ecliptic.

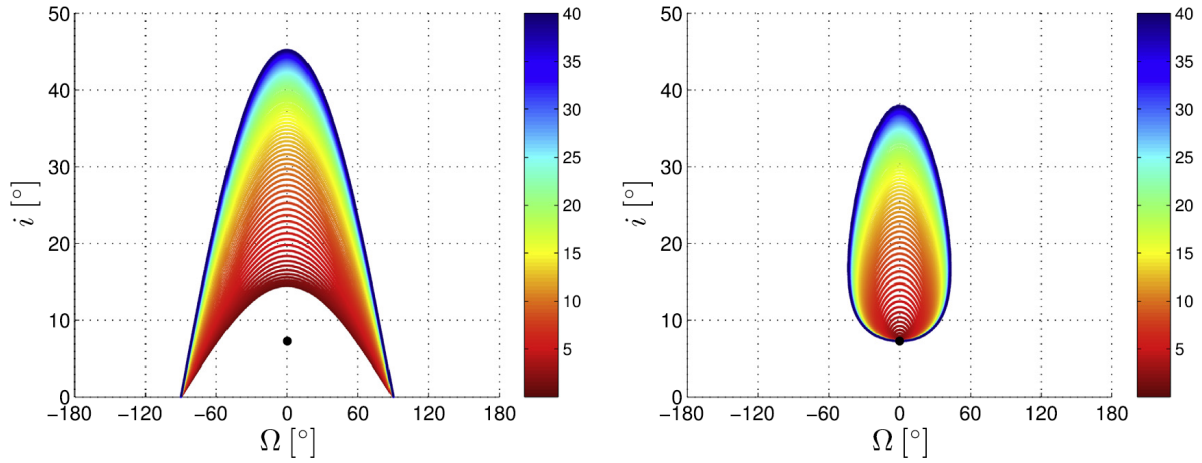


Figure 2.7: Evolution of the orbital planes of HAMR objects, starting in GEO (left) and in the Laplace plane at GEO altitude (right). The colorbar indicates the value of Λ, the SRP perturbation angle [°], which is higher when perturbations by SRP are stronger. The black dot indicates the Laplace plane. For this simulation the Moon orbit was assumed to be in the ecliptic plane (Rosengren et al., 2014).

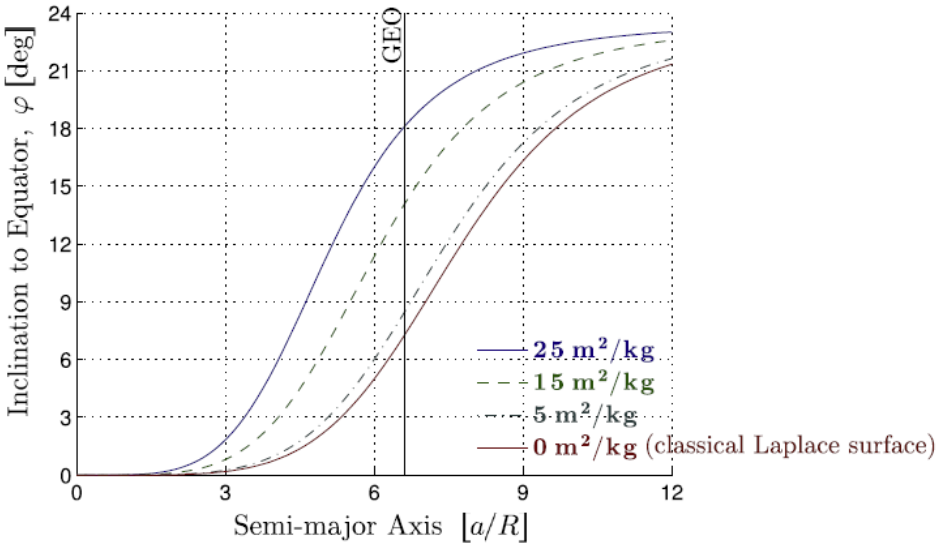


Figure 2.8: Inclination of the classical Laplace plane (with AMR = 0 $m^2$/kg) and several modified Laplace planes (for AMR = 5, 10 and 15 $m^2$/kg) plotted versus the semi-major axis of an orbit (Rosengren et al., 2014).

# 3

# ORBIT PROPAGATION MODEL

To simulate the long-term orbit evolution of debris from fragmentation events an orbit propagator was developed. This chapter describes the orbit dynamics model used for the propagator. An averaged orbit dynamics model based on Milankovitch elements was chosen, which is described by Rosengren and Scheeres (2013) and Rosengren and Scheeres (2014) and was developed for investigating the behaviour of HAMR debris. With Milankovitch elements the eccentricity vector and angular momentum vector are used as orbital elements. This is quite unconventional, however the model presented by Rosengren and Scheeres allows for very fast numerical integrations while still providing results that are sufficiently accurate for the purpose of this thesis. This chapter only describes the most important elements of the model that were actually implemented in the propagator. For a more detailed discussion the reader is referred to the literature study that was performed in preparation for the thesis (Roelen, 2015).

Section 3.1 describes the reference frame used by the orbit propagator. Section 3.2 gives an overview of the orbital elements that are relevant for this research, as well as orbital element transformations that were used for the computation of some of the results. Section 3.3 contains force models based on Milankovitch elements for the perturbation forces included in the propagator, after which Section 3.4 explains the averaged perturbation equations in Lagrange form. Section 3.5 describes a method that was used to compute GEO crossings from the propagation results. Finally Section 3.6 explains the choice of the integrator that is used in the propagator.

## 3.1. REFERENCE FRAME

Many of the equations in this chapter use position vectors relative to the Earth. For example the position vector between the Earth and the Sun is required in the computation of SRP perturbations. Also this research deals with objects orbiting the Earth, therefore a geocentric inertial coordinate system is used, as illustrated by Fig. 3.1. The origin is at the centre of the Earth, while the $x$-axis is pointing in the direction of the vernal equinox, denoted by $\Upsilon$. The $z$-axis is aligned with the Earth's spin axis and the $y$-axis is simply perpendicular to the other two axes. This is a common reference system that is also used in most of the literature reviewed for this thesis. While the reference system is usually not explicitly mentioned in articles, it can be deduced from for example the Laplace plane orientation. The specific reference system used in the propagator is J2000, which is defined with the mean equinox at 12:00 on 1 January 2000.

## 3.2. ORBITAL ELEMENTS

The propagator uses Milankovitch elements for the numerical integration of orbits, however most of the results in this report are presented using Kepler elements. Therefore both of these elements as well as transformations between them are described in this section.

### 3.2.1. KEPLER ELEMENTS

The Kepler elements are well known and commonly used to describe orbits, since they give good insight into the shape of an orbit. The elements are the semi-major axis $a$, the eccentricity $e$, the inclination $i$, the

argument of perigee $\omega$ and the right ascension of the ascending node $\Omega$. The last element can be either the true anomaly $\theta$, the eccentric anomaly $E$ or the mean anomaly $M$. In this report $\theta$ is always used. The Kepler elements are depicted in Fig. 3.1.

Kepler elements are not suitable for perturbation computations of orbits in the geostationary region, because there will be singularities when orbits have zero or near-zero inclination or eccentricity. It is possible to use modified equinoctial elements that do not have these singularities, however with these the orbital dynamics equations become more complicated. The model created by Rosengren and Scheeres which is based on Milankovitch elements also has no singularities, while the equations are much simpler and the use of averaged dynamics reduces computation time because larger step sizes are possible during integration.

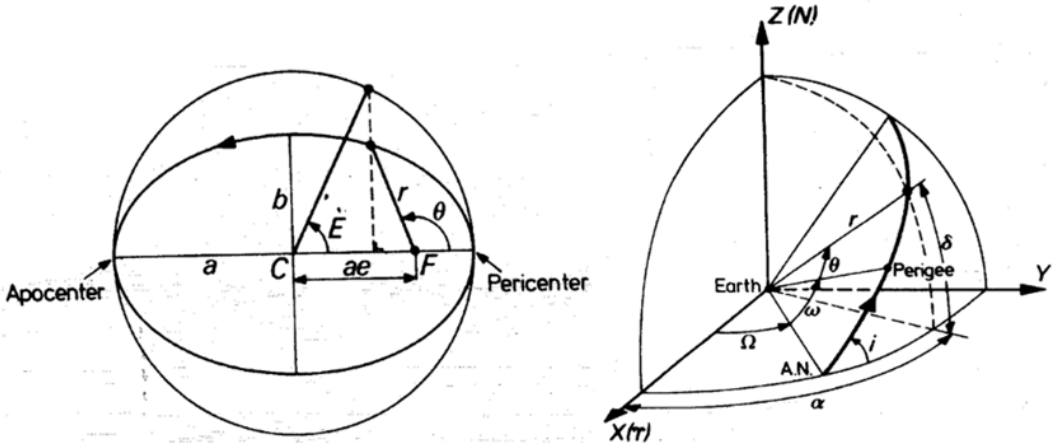


Figure 3.1: Kepler orbital elements (Wakker, 2010a)

### 3.2.2. MILANKOVITCH ELEMENTS

Milankovitch elements consist of the angular momentum and eccentricity vectors, as defined by Eqs. 3.1 and 3.3. $\boldsymbol{H}$ is the angular momentum vector, which is perpendicular to the orbit plane. The magnitude of $\boldsymbol{H}$ is given by Eq. 3.2, where $\mu$ is the gravitational parameter of the central body. This report only considers Earth orbits, therefore $\mu$ will always have the value of the Earth's gravitational parameter. $\boldsymbol{e}$ denotes the eccentricity vector, which points to the perigee of an orbit (Rosengren et al., 2014).

$$\boldsymbol{H} = \boldsymbol{r} \times \boldsymbol{v} \tag{3.1}$$

$$H = \sqrt{\mu a(1-e^2)} \tag{3.2}$$

$$\boldsymbol{e} = \frac{1}{\mu}\boldsymbol{v} \times \boldsymbol{H} - \frac{\boldsymbol{r}}{|\boldsymbol{r}|} \tag{3.3}$$

Note that even though the angular momentum and eccentricity vector together contain 6 elements, these are not yet sufficient to describe orbits due to the fact that they are not fully independent of each other. This is because the vectors are orthogonal to each other: $\boldsymbol{H} \cdot \boldsymbol{e} = 0$. Another way to understand this is that $\boldsymbol{H}$ and $\boldsymbol{e}$ describe the shape and orientation of an orbit, but do not include the position of the satellite within the orbit.

For this reason one more parameter is required which defines the satellite position, similar to e.g. the true anomaly for Kepler orbits. For Milankovitch elements the true longitude $L$ or mean longitude $l$ is used. The true longitude is the angle from the vernal equinox to the ascending node plus the angle from the ascending node to the position of the satellite in orbit, defined by Eq. 3.4.

$$L = \Omega + u = \varpi + \theta \tag{3.4}$$

In this equation $u = \omega + \theta$ is the argument of latitude and $\varpi = \Omega + \omega$ the longitude of the perigee. The mean longitude is defined by Eq. 3.5. Note that the original literature uses $\theta$ for the argument of latitude rather than

$u$, and $f$ for the true anomaly. This is changed in this report because it is conventional at TU Delft to use $\theta$ for true anomaly and $u$ for the argument of latitude.

$$l = \varpi + M \tag{3.5}$$

Milankovitch elements can be computed from Kepler elements using Eqs. 3.6 and 3.7, where the hat symbol indicates unit vectors and $\boldsymbol{x}$, $\boldsymbol{y}$ and $\boldsymbol{z}$ are the Cartesian coordinate system vectors. $\boldsymbol{h}$ is the scaled angular momentum vector, defined by Eq. 3.8 (Rosengren et al., 2014).

$$\boldsymbol{H} = H\hat{\boldsymbol{h}} = H((\sin i \sin\Omega)\hat{\boldsymbol{x}} - (\sin i \cos\Omega)\hat{\boldsymbol{y}} + (\cos i)\hat{\boldsymbol{z}}) \tag{3.6}$$

$$\begin{aligned} \boldsymbol{e} &= e\hat{\boldsymbol{e}} \\ &= e[(\cos\omega\cos\Omega - \cos i \sin\omega \sin\Omega)\hat{\boldsymbol{x}} + (\cos\omega\sin\Omega + \cos i \sin\omega\cos\Omega)\hat{\boldsymbol{y}} + (\sin i \sin\omega)\hat{\boldsymbol{z}} \end{aligned} \tag{3.7}$$

$$\boldsymbol{h} = \boldsymbol{H}/\sqrt{\mu a} \tag{3.8}$$

### 3.2.3. CARTESIAN COORDINATE TRANSFORMATIONS

For the computation of GEO crossings the Cartesian position and velocity vectors are used, therefore it is necessary to make transformations to these from the Milankovitch or Kepler elements. This is also necessary in the fragmentation model, to add a $\Delta V$ from a fragmentation to a fragment's velocity. This section describes the equations for such orbital element transformations, which are taken from (Wertz, 2009).

To find the position in Cartesian coordinates, from Kepler elements, Eqs. 3.9 and 3.10 can be used.

$$\begin{pmatrix} x \\ y \\ z \end{pmatrix} = \begin{pmatrix} l_1 & l_2 \\ m_1 & m_2 \\ n_1 & n_2 \end{pmatrix} \begin{pmatrix} \xi \\ \eta \end{pmatrix}; \qquad \begin{pmatrix} \xi \\ \eta \end{pmatrix} = \begin{pmatrix} r\cos\theta \\ r\sin\theta \end{pmatrix} \tag{3.9}$$

$$\begin{aligned} l_1 &= \cos\Omega\cos\omega - \sin\Omega\sin\omega\cos i \\ l_2 &= -\cos\Omega\sin\omega - \sin\Omega\cos\omega\cos i \\ m_1 &= \sin\Omega\cos\omega + \cos\Omega\sin\omega\cos i \\ m_2 &= -\sin\Omega\sin\omega + \cos\Omega\cos\omega\cos i \\ n_1 &= \sin\omega\sin i \\ n_2 &= \cos\omega\sin i \end{aligned} \tag{3.10}$$

The velocity in Cartesian components can be computed by Eq. 3.11.

$$\begin{aligned} \dot{x} &= \frac{\mu}{H}[-l_1\sin\theta + l_2(e+\cos\theta)] \\ \dot{y} &= \frac{\mu}{H}[-m_1\sin\theta + m_2(e+\cos\theta)] \\ \dot{z} &= \frac{\mu}{H}[-n_1\sin\theta + n_2(e+\cos\theta)] \end{aligned} \tag{3.11}$$

To convert from Cartesian coordinates to Kepler elements, Eqs. 3.12 to 3.17 are used. Most of these equations contain $\boldsymbol{e}$ and $\boldsymbol{h}$, which are the Milankovitch elements. These equations can therefore also be used to transform Milankovitch elements to the Kepler elements $i$, $\Omega$, $\omega$ and $\theta$. $e$ can be found by taking the magnitude of the eccentricity vector and $a$ can be computed using Eq. 3.2.

$$r = \|\boldsymbol{r}\|; \qquad V = \|\boldsymbol{V}\|; \qquad \boldsymbol{H} = \boldsymbol{r}\times\boldsymbol{V}; \qquad \boldsymbol{N} = \begin{pmatrix} 0 \\ 0 \\ 1 \end{pmatrix} \times \boldsymbol{H} \tag{3.12}$$

$$a = 1/\left(\frac{2}{r} - \frac{V^2}{\mu}\right) \tag{3.13}$$

$$\boldsymbol{e} = \frac{\boldsymbol{V} \times \boldsymbol{H}}{\mu} - \frac{\boldsymbol{r}}{r}; \qquad e = \|\boldsymbol{e}\| \tag{3.14}$$

$$i = \text{acos}\left(\frac{H_Z}{\|\boldsymbol{H}\|}\right) \tag{3.15}$$

$$N_{xy} = \sqrt{N_x^2 + N_y^2}; \qquad \Omega = \text{atan2}\left(\frac{N_y}{N_{xy}}, \frac{N_x}{N_{xy}}\right) \tag{3.16}$$

$$\begin{aligned} \omega &= sign * \text{acos}(\hat{\boldsymbol{e}} \cdot \hat{\boldsymbol{N}}) \qquad (sign = +1 \text{ if } (\hat{\boldsymbol{N}} \times \boldsymbol{e}) \cdot \boldsymbol{H} > 0; \quad 1 \text{ otherwise}) \\ \theta &= sign * \text{acos}(\hat{\boldsymbol{r}} \cdot \hat{\boldsymbol{e}}) \qquad (sign = +1 \text{ if } (\hat{\boldsymbol{e}} \times \boldsymbol{r}) \cdot \boldsymbol{H} > 0; \quad 1 \text{ otherwise}) \end{aligned} \tag{3.17}$$

## 3.3. FORCE MODELS

This section discusses the models of the perturbation forces that are taken into account by the propagator. Since the discovery of HAMR objects there have been several studies investigating the evolution of HAMR object orbits, which have used different perturbation forces. Liou and Weaver (2005) used an averaged model which included perturbations by the Earth's gravity field up to the $4^{\text{th}}$ zonal harmonic, low-order lunisolar gravitational attraction and SRP taking into account the Earth's shadow effect. They compared the results to those obtained using a $7^{\text{th}}$ degree and order non-averaged model. Their research showed that for HAMR objects in GEO long-term orbit evolution is dominated by major perturbations, and not higher-order terms.

Additionally Chao (2006) studied orbit evolution through analytically averaged equations. Chao investigated the effects of doubly-averaged lunisolar attraction and singly-averaged SRP. However the equations of motion were written using classical Kepler elements, which has singularities near zero inclination and eccentricity.

Rosengren and Scheeres (2013) have contributed to this area of research by developing a simpler model than the one used by Liou and Weaver, which also has no singularities. The perturbation forces taken into account in this model are $J_2$, lunisolar gravitational attraction and solar radiation pressure. The model has been compared to a $4^{\text{th}}$ degree and order model, showing that it is sufficient to only use $J_2$ and neglect the higher order gravity field terms. This section describes the force models of Rosengren and Scheeres. The force models were not used for the majority of the computations, as the averaged dynamics equations of Section 3.4 were used, however they were used for some of the software validation computations.

### 3.3.1. THE EARTH-MOON-SUN SYSTEM

Many of the forces depend on the relative positions of the Earth, Sun and Moon. The vectors that are used to express these positions are depicted in Fig. 3.2. While Rosengren and Scheeres (2013) describe a simple Keplerian orbit model that could be used for the computation of the positions of the Sun and Moon relative to Earth, it is also possible to use ephemerides data for higher-accuracy positions. For the orbit propagator NASA's SPICE ephemerides have been used because of the higher accuracy. There is also a Tudat Spice Interface included in the Tudat C++ libraries, which means no separate code needed to be developed for this. The simulation times are still very fast (about 3 seconds for a 100 year-orbit propagation), therefore it is not necessary to use the simpler Keplerian model.

### 3.3.2. SOLAR RADIATION PRESSURE

SRP acceleration is affected by not only the area-to-mass ratio and reflectivity of an object, but also its shape and orientation. Choosing an object shape is therefore an important part of modelling SRP perturbations. For the orbit propagator the cannonball model is used, where objects are assumed to be a perfect sphere. With this model the direction of SRP acceleration is in a straight line away from the Sun.

The SRP acceleration is then defined by Eq. 3.18. This equation uses the assumption that $r << d_s$ and neglects the effects of the Earth's shadow and Earth-albedo radiation pressure, which are both small for GEO.

$$\boldsymbol{a}_{srp} = -\frac{\beta}{d_s^2}\hat{\boldsymbol{d}}_s, \qquad \beta = C_R(A/m)P_\Phi \tag{3.18}$$

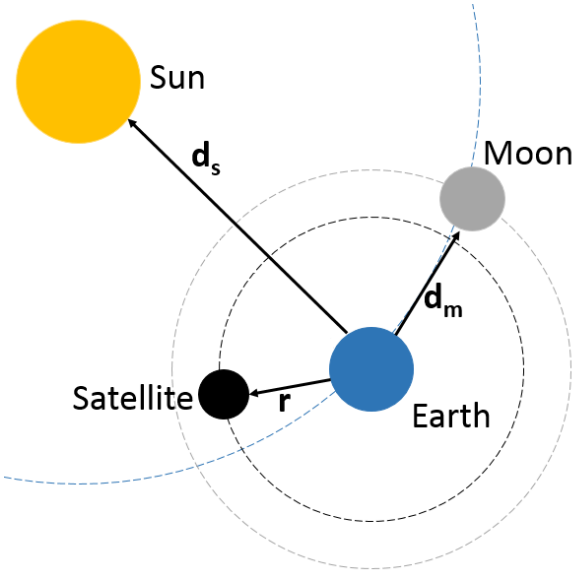


Figure 3.2: Position vectors of the Earth-Moon-Sun system. Note that sizes and distances are not to scale, also vectors are in reality between the centres of the bodies.

### 3.3.3. EARTH GRAVITATIONAL PERTURBATIONS

The most important terms of the Earth's gravity field which affect HAMR debris orbits are $J_2$ and $J_{2,2}$. The acceleration by these terms is given in vector expressions in Eq. 3.19, where the unit vectors $\hat{\boldsymbol{p}}$, $\hat{\boldsymbol{q}}$ and $\hat{\boldsymbol{s}}$ are assumed to be aligned with the Earth's maximum, intermediate and minimum axes of inertia. Note that only the vector $\hat{\boldsymbol{p}}$ will remain in the averaged model, which is aligned with the Earth's rotation pole.

$C_{20} = -J_2 R_e^2$ is the dimensional oblateness gravity field coefficient, $R_e$ the mean equatorial radius of the Earth and $C_{22}$ the dimensional ellipticity gravity field coefficient (Rosengren and Scheeres, 2013). The values of $J_2$ and $J_{2,2}$ are respectively 1082.6357 $10^{-6}$ and 1.8155628 $10^{-6}$ (Wakker, 2010b).

$$\boldsymbol{a}_2 = \frac{3\mu C_{20}}{2r^4}\{[1-5(\hat{\boldsymbol{r}}\cdot\hat{\boldsymbol{p}})^2]\hat{\boldsymbol{r}} + 2(\hat{\boldsymbol{r}}\cdot\hat{\boldsymbol{p}})\hat{\boldsymbol{p}}\} - \frac{3\mu C_{22}}{r^4}\{5[(\hat{\boldsymbol{r}}\cdot\hat{\boldsymbol{s}})^2 - (\hat{\boldsymbol{r}}\cdot\hat{\boldsymbol{q}})^2]\hat{\boldsymbol{r}} - 2[(\hat{\boldsymbol{r}}\cdot\hat{\boldsymbol{s}})\hat{\boldsymbol{s}} - (\hat{\boldsymbol{r}}\cdot\hat{\boldsymbol{q}})\hat{\boldsymbol{q}}]\} \tag{3.19}$$

### 3.3.4. LUNISOLAR GRAVITATIONAL ATTRACTION

The perturbations by the Sun and Moon's gravity are modelled as third-body perturbations. It is assumed that the distance between the satellite and the Earth is small compared to the distance between Earth and the third bodies ($r/d_p << 1$). The perturbing acceleration is then approximated by Eq. 3.20, where the subscript $p$ refers to the perturbing third body (Sun or Moon) and $\boldsymbol{d}$ is the position vector relative to the Earth.

$$\boldsymbol{a}_p = \frac{\mu_p}{d_p^3}[3(\boldsymbol{r}\cdot\hat{\boldsymbol{d}}_p)\hat{\boldsymbol{d}}_p - \boldsymbol{r}] \tag{3.20}$$

## 3.4. AVERAGED ORBIT DYNAMICS

For each of the force models described in Section 3.3 this section presents the averaged Lagrange perturbation equations. For averaging to be valid it is assumed that perturbation forces are sufficiently small that orbit perturbations over a single orbital revolution are small and average out over small periods. Rosengren and Scheeres (2013)) have described how to derive these equations and summarized the results for the forces relevant to HAMR debris in GEO.

### 3.4.1. AVERAGED SRP DYNAMICS

The Lagrange planetary equations for SRP are shown in Eqs. 3.21 and 3.22.

$$\dot{\boldsymbol{h}}_{srp} = \frac{3a_{srp}}{2}\sqrt{\frac{a}{\mu}}\hat{\boldsymbol{a}}_{srp} \times \boldsymbol{e} \tag{3.21}$$

$$\dot{\boldsymbol{e}}_{srp} = \frac{3a_{srp}}{2}\sqrt{\frac{a}{\mu}}\hat{\boldsymbol{a}}_{srp} \times \boldsymbol{h} \tag{3.22}$$

### 3.4.2. AVERAGED $J_2$ DYNAMICS

From the Earth's gravitational perturbations only $J_2$ dynamics are included in the averaged model. For geostationary satellites $J_{2,2}$ is also very important, as they stay above the same point on the Earth and continuously experience the same acceleration due to $J_{2,2}$. For graveyard orbits this is less important, as the orbital period is slightly different from the Earth's rotation period. Lemaitre et al. (2009) discovered a resonance effect which can cause chaotic behaviour for HAMR objects in GEO. However, this phenomenon is limited to a very narrow range of semi-major axes (hundreds of meters) and therefore not relevant for graveyard orbits. With the averaging method used by Rosengren and Scheeres (2013) it is also not possible to describe perturbations due to $J_{2,2}$, therefore the $J_{2,2}$ effect is not included in the model. One of the validation simulations described in Section 5.2 does compare the difference of including $J_{2,2}$ in a non-averaged simulation. The averaged equations of motion for the $J_2$ effect are given by Eqs. 3.23 and 3.24.

$$\dot{\boldsymbol{h}}_2 = \frac{3nC_2}{2a^2h^5}(\hat{\boldsymbol{p}} \cdot \boldsymbol{h})\hat{\boldsymbol{p}} \times \boldsymbol{h} \tag{3.23}$$

$$\dot{\boldsymbol{e}}_2 = \frac{3nC_2}{4a^2h^5}\{[1 - \frac{5}{h^2}(\hat{\boldsymbol{p}} \cdot \boldsymbol{h})^2]\boldsymbol{h} + 2(\hat{\boldsymbol{p}} \cdot \boldsymbol{h})\hat{\boldsymbol{p}}\} \times \boldsymbol{e} \tag{3.24}$$

### 3.4.3. AVERAGED THIRD-BODY DYNAMICS

The averaged equations of motion for third-body perturbations are shown in Eqs. 3.25 and 3.26. Note that in these equations the vectors should be row vectors, while $^T$ denotes the transpose of a vector, which is then a column vector.

$$\dot{\boldsymbol{h}}_p = \frac{3\mu_p}{2nd_p^3}\hat{\boldsymbol{d}}_p(5\boldsymbol{e}^T\boldsymbol{e} - \boldsymbol{h}^T\boldsymbol{h}) \times \hat{\boldsymbol{d}}_p \tag{3.25}$$

$$\dot{\boldsymbol{e}}_p = \frac{3\mu_p}{2nd_p^3}[\hat{\boldsymbol{d}}_p(5\boldsymbol{e}^T\boldsymbol{h} - \boldsymbol{h}^T\boldsymbol{e}) \times \hat{\boldsymbol{d}}_{\boldsymbol{p}} - 2\boldsymbol{h} \times \boldsymbol{e}] \tag{3.26}$$

### 3.4.4. AVERAGED EQUATIONS OF MOTION

The averaged equations of motion for all perturbations combined are made by simply adding up the separate equations for the individual perturbations, as stated by Eqs. 3.27 and 3.28. The propagator is programmed such that the separate perturbations can be switched on or off, by including or excluding their equations from the sum of the combined perturbations. An RK4 integrator is used to integrate the equations of motion and compute how the orbital elements change over time.

$$\dot{\boldsymbol{h}} = \dot{\boldsymbol{h}}_{srp} + \dot{\boldsymbol{h}}_2 + \dot{\boldsymbol{h}}_s + \dot{\boldsymbol{h}}_m \tag{3.27}$$

$$\dot{\boldsymbol{e}} = \dot{\boldsymbol{e}}_{srp} + \dot{\boldsymbol{e}}_2 + \dot{\boldsymbol{e}}_s + \dot{\boldsymbol{e}}_m \tag{3.28}$$

## 3.5. GEO CROSSINGS

The orbit propagator also includes a GEO crossings computation. This computation checks whether an object passes within a certain distance to GEO (the distance can be set as input), which is then counted as a crossing. The total number of crossings throughout the integration is summed up and provided for every step in the output data. This section describes the method used to compute the GEO crossings.

### 3.5.1. COMPUTATION

At each time-step a computation is done to check whether a GEO crossing is possible within one orbit revolution with the orbital elements at that time-step. For an accurate result the step-size should be set equal to the orbital period, since crossings could be counted multiple times with smaller step-sizes or overlooked with larger step-sizes. Since the orbit propagator uses averaged orbit dynamics, the exact position of an object within its orbit (usually defined by the true anomaly) is not known. Only the elements $a$, $e$, $i$, $\omega$ and $\Omega$ can be derived from the Milankovitch elements ($\boldsymbol{h}$ and $\boldsymbol{e}$) that are used in the orbit propagation.

However, an object will pass through all possible true anomalies each orbital revolution. Therefore the check is done by setting two true anomaly values, at which the object intersects the equatorial plane, and for these true anomalies the distance to GEO is computed. These values are $\theta = -\omega$ and $\theta = \pi - \omega$. The radial distance is computed through Eq. 3.29. The GEO radius is then subtracted to find the distance to GEO at which the object intersects the equatorial plane. If the distance is within the set minimum distance, it is counted as a crossing. In the standard cases this is set to 50 km. Since there are two equatorial plane intersections, for each revolution there are either 0, 1 or 2 crossings. These crossings are added up throughout the integration to find the total number of crossings. The crossings number can be used to assess the effectiveness of various GEO disposal orbits, as the number should be preferably low.

$$r = \frac{a(1-e^2)}{1+e\cos\theta} \tag{3.29}$$

### 3.5.2. CATASTROPHIC AND WEIGHTED CROSSINGS

When a crossing is found, a computation is done to check whether a collision with the propagated object and a GEO satellite would be catastrophic. These are referred to as catastrophic crossings. Of course a crossing only has a small chance of resulting in a collision, but if there would be a collision one can compute whether that would be catastrophic. The crossings are also weighted based on the fragment mass they would produce in the event of a collision.

To find whether a crossing is a catastrophic crossing the following method is used: the Keplerian state of the crossing is converted to a Cartesian state. The x- and y-coordinates are used to compute the true anomaly of an object in GEO at the crossing position, through an atan2 function. The Keplerian state of the GEO object is then also converted to Cartesian state. The Cartesian velocities are subtracted to find the collision velocity. The kinetic energy of the collision is then computed as $E_k = \frac{1}{2}mV^2$, where $m$ refers to the mass of the impacting object (the one that is being propagated). The kinetic energy is then divided by the mass of the target object (e.g. a satellite in GEO). A target mass of 1000 kg is assumed. If the ratio of impact energy to target mass is 40 J/g or higher, the collision is catastrophic. This limit for catastrophic collisions is defined in the NASA standard satellite breakup model, which is described in Ch. 4.

For each crossing a weighted crossing value is also computed, which is equal to the fragment mass that would be created in a collision divided by total mass of an intact GEO satellite. A catastrophic crossing has a weight of 1, as a collision would fragment an entire GEO satellite, while for non-catastrophic collisions the fragment mass is computed using Eq. 4.3. This is divided by the total mass (set to 1000 kg) to find the weighted value. The propagator produces in total 3 crossing values for each time-step: total number of crossings, total catastrophic crossings and total weighted crossings.

## 3.6. INTEGRATOR

Initially it was decided to use a DOPRI8 integrator, as discussed in (Roelen, 2015). The reasons for this were that it is one of the integrators included in Tudat, it is efficient for large step-sizes and it is a variable step-size integrator, which means it uses the largest step-size possible while keeping the results within a specified error tolerance. An efficient integrator is desired since long-term orbit propagation can require long computation times.

However the GEO crossings computation was not initially planned, and for this it is actually more convenient to have a constant step-size equal to the orbital revolution. This way the crossing computation can be done at every time-step without having to interpolate the results. With the DOPRI8 integrator step-sizes of several days were possible, while objects near GEO have an orbital period of only one day. DOPRI8 requires more

computations per time-step than lower-order integrators, therefore it is less efficient when using time-steps that are smaller than necessary. The variable step-size component was also no longer necessary. Therefore in the end an RK4 integrator was used, which is still accurate when using step-sizes equal to one orbital revolution and faster than DOPRI8 for the same step-size.

# 4

# FRAGMENTATION MODEL

Fragmentation events are events that cause a satellite to breakup into fragments, such as collisions and explosions. Fragmentation models (often also called breakup models) typically provide distributions of the mass, $\Delta V$ and cross-sectional area of fragments. These parameters are required for the orbit propagation of fragments, and the mass is required for modelling consequences of potential collisions by the fragments. A group of fragments from a single source is also called a debris cloud.

Different space agencies have developed their own space debris models. Models are made not only for fragmentations, but also for orbit propagation and long-term evolution of the entire debris population, taking into account fragmentation probabilities. Examples are ESA's DELTA (Debris Environment Long-Term Analysis) (ESA, 2013), the Chinese CARDC-SBM (China Aerodynamics Research and Development Center - Spacecraft Breakup Model)(Shengwei et al., 2014) and the NASA standard satellite breakup model (Liou, 2012).

The NASA model seems to be the most commonly discussed in literature, while relatively little information is available on the other models. It would also take a large amount of time to thoroughly investigate all models, therefore the NASA model was chosen for the simulation software and is discussed in this chapter. According to Liou (2012) the model compares well with other space agencies' models. Section 4.1 describes a classical version of the NASA model, which was last updated in 1990. The currently most recent model is described in Section 4.2 and is called the *NASA Standard Satellite Breakup Model* (Johnson et al., 2001). Section 4.3 describes suggested modifications to the NASA model for low-velocity collisions (Hanada, 2000), which are typical for GEO and therefore these modifications have been included in the simulation software.

## 4.1. CLASSICAL MODEL

The classical explosion model was used by Pardini and Anselmo (2005) to simulate satellite explosions in geostationary orbit. This section describes some of the classical equations for both explosions and collisions, and shows results that were obtained by Pardini and Anselmo using these equations.

### 4.1.1. MASS DISTRIBUTION

Su and Kessler (1985) studied the evolution of the debris environment in LEO, for which they modelled both explosions and collisions. For explosions a mass distribution equation was derived based on a ground-based experiment and observed explosions in orbit. The ground-based experiment provided information about smaller-sized fragments that cannot be observed in orbit due to radar limitations. The resulting equation is shown in Eq. 4.1, where $N(m)$ represents the cumulative number of fragments with a mass larger than $m$. $m_t$ is the total exploding mass.

$$N(m)^{EXP} = \begin{cases} 0.171 m_t e^{-0.6502\sqrt{m}}, & m \geqslant 1.936\,\text{kg} \\ 0.869 m_t e^{-1.8202\sqrt{m}}, & m < 1.936\,\text{kg} \end{cases} \tag{4.1}$$

A comparison between results from Eq. 4.1 and an observed spacecraft explosion is shown in Fig. 4.1. For smaller fragments the difference between the model and observations increases. This is assumed to be caused by detectability limitations of the ground-based radar system.

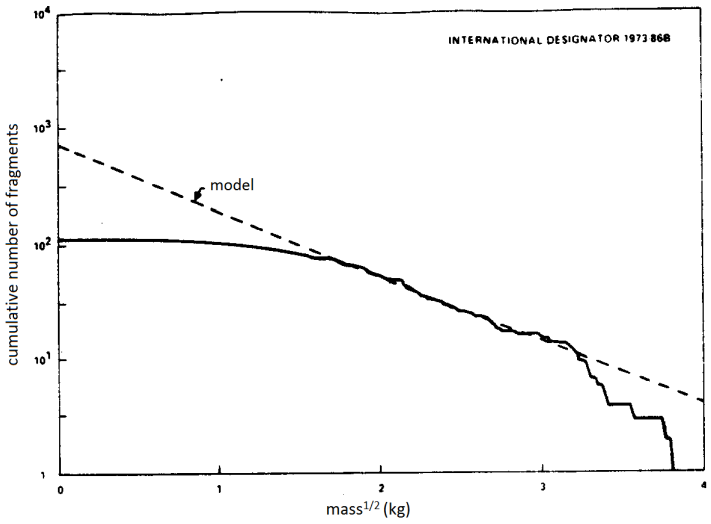


Figure 4.1: Cumulative number of explosion fragments versus the square root of the fragment mass. The dashed line shows the number estimated by Eq. 4.1, while the solid line shows observed fragments from the second stage of the Delta rocket for satellite NOAA 3 (Su and Kessler, 1985).

Su and Kessler also modelled collision fragmentations. Generally in collision models a distinction is made between a catastrophic and a non-catastrophic event. A collision is catastrophic when the colliding objects are entirely fragmented, which can happen for example when two satellites collide with each other at a 90° angle, resulting in a very large collision velocity. A non-catastrophic collision can occur when the mass of one of the objects is very small, such as a HAMR debris object colliding with a GEO satellite, or when the collision velocity is very low. The smaller object is referred to as a projectile and the larger object the target. During a non-catastrophic collision the projectile is assumed to be fragmented, and some mass from the target is ejected in addition to the projectile mass.

The ejected mass for a non-catastrophic collision is given by Eq. 4.2, where $m_e$ is the ejected mass and $m_{proj}$ the projectile mass. The symbol $v$ represents the collision velocity (in m/s) which is normalized by a constant factor. Su and Kessler used a factor 1, meaning $v$ is the actual collision velocity. This equation for the ejected mass is also used in the current NASA model (Liou, 2012).

$$m_e = (v/1000)^2 m_{proj} \tag{4.2}$$

A collision is assumed to be catastrophic when $m_e \geqslant 0.1 m_{tar}$, where $m_{tar}$ is the target mass. The total mass $m_t$ of fragments is the sum of the ejected mass and the projectile mass as defined by Eq. 4.3.

$$\begin{array}{lcll} m_t & = & m_{tar} + m_{proj} & \text{catastrophic} \\ m_t & = & m_e + m_{proj} = m_{proj}(1 + (v/1000)^2) & \text{non} - \text{catastrophic} \end{array} \tag{4.3}$$

The number of fragments with mass larger than $m$ is then given by Eq. 4.4 (Su and Kessler, 1985). The velocity distribution of fragments was not well known yet at the time. Su and Kessler assumed a velocity of 10 to 30 m/s for non-catastrophic collision, with random variation independent of fragment size. For catastrophic collision a range of 5 to 15 m/s was used for larger fragments.

$$N(m)^{COL} = 0.4478 \left( \frac{m}{m_t} \right)^{-0.7496} \tag{4.4}$$

### 4.1.2. FRAGMENT DIAMETER AND MASS RELATION

Reynolds (1990) wrote a review of the activities of the NASA orbital debris program at the time, which included satellite breakup models. The paper includes not only Eqs. 4.1 and 4.4 for the fragments number and mass distribution, but also equations for the velocity of fragments and the relation between fragment mass and diameter.

The mass of a fragment in kg, $m$, is related to the fragment diameter in m, $d$ by Eq.4.5 (Reynolds, 1990).

$$m = \begin{cases} 47.2d^{2.26}, & d \geqslant 0.01\text{m} \\ 1.40 \cdot 10^3 d^3, & d < 0.01\text{m} \end{cases} \tag{4.5}$$

If fragment shapes are assumed to be spherical, the fragment cross-sectional area can also be used instead of the diameter, resulting in Eq. 4.6 (Pardini and Anselmo, 2005).

$$m = \begin{cases} 62.013A^{1.13}, & A \geqslant 8.04 \cdot 10^{-5}\,\text{m}^2 \\ 2030.33A^{1.5}, & A < 8.04 \cdot 10^{-5}\,\text{m}^2 \end{cases} \tag{4.6}$$

Fig. 4.2 shows the area-to-mass ratio distribution of objects with a diameter of at least 10 cm, from a simulated explosion of a 2000 kg geostationary satellite. The minimum object size of 10 cm was chosen by Pardini and Anselmo because this is roughly the smallest size of objects that can be observed from Earth. The results of the simulation could then be compared to observations. Note that the number of fragments plotted here is not the cumulative number, but rather the number of objects within a certain AMR bin. For example, there are 450 objects with an AMR between 0 and 0.05 $\text{m}^2/\text{kg}$. Because only objects with diameters of at least 10 cm are shown, it seems as if there are fewer objects for higher AMR values. However there were also many cm and mm sized objects that are not shown in this plot, which will may have larger AMR values.

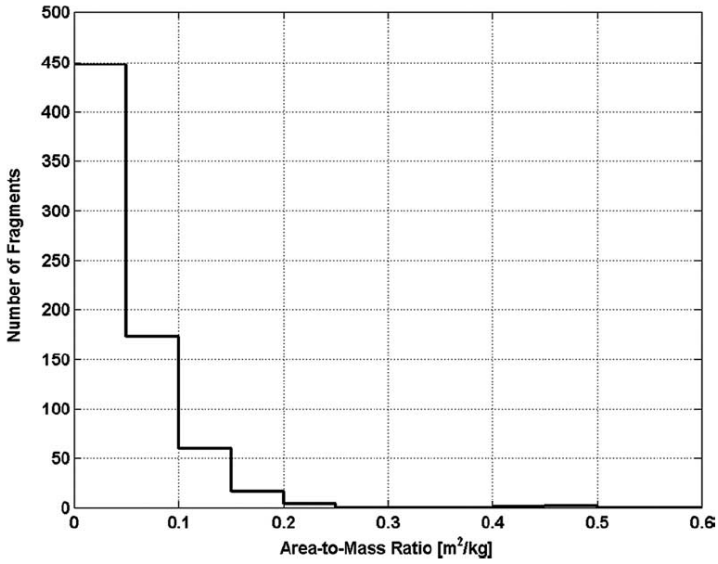


Figure 4.2: Distribution of area-to-mass ratio for debris with $d \geqslant 10$ cm, from simulated satellite explosion in GEO (Pardini and Anselmo, 2005).

### 4.1.3. FRAGMENT VELOCITY DISTRIBUTION

The average velocity distribution of fragments from a collision is given by (Reynolds,1990) as Eq. 4.7.

$$\log(\overline{\Delta V}) = \begin{cases} 0.875 - 0.0676\left(\log\frac{d}{d_m}\right)^2 & d \geqslant d_m \quad \text{with} \quad d_m = 9.9083 \cdot 10^{-8} m_{proj}^{1/3} (v/1000)^{2/3} \\ 0.875 & d < d_m \end{cases} \tag{4.7}$$

Although the above equation requires a collision velocity and projectile mass, it was used by Pardini and Anselmo (2005) to simulate explosions (without a collision) by assuming values for these parameters. Using $m_{proj} = 15$ kg and $v = 10$ km/s resulted in Eq. 4.8, where $\overline{\Delta V}$ is only a function of the fragment diameter.

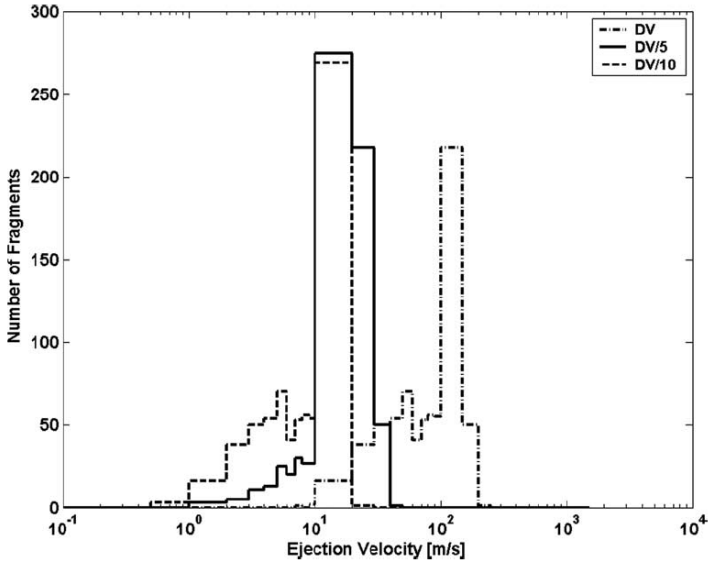


Figure 4.3: Distribution of ejection velocities for debris with $d \geqslant 10$ cm, from simulated satellite explosion in GEO (Pardini and Anselmo, 2005).

$$\log(\overline{\Delta V}) = -0.0676(\log d)^2 - 0.804 \log d - 1.514 \tag{4.8}$$

These equations only give an average velocity distribution. In reality not all objects with the same diameter will have exactly the same velocity. Because of this a random variation is added to $\overline{\Delta V}$ as shown in Eq. 4.9 (Pardini and Anselmo,2005), where $y$ is a random number between zero and one. The $\Delta V$ can be added in a random direction to the initial velocity (before the explosion) to find the final velocity of each fragment.

$$\Delta V = \begin{cases} \overline{\Delta V}(0.1 + 0.6\sqrt{3y}, & 0.00 \leqslant y < 0.75 \\ \overline{\Delta V}(1.3 - 0.6\sqrt{1-y}), & 0.75 \leqslant y < 1.00 \end{cases} \tag{4.9}$$

The velocity distribution of the same debris of which the AMR is plotted in Fig. 4.2 is displayed in Fig. 4.3. Different lines are plotted for the nominal $\Delta V$ (which is called DV in the figure) and the nominal $\Delta V$ divided by 5 and 10. For each line a peak is visible with the largest number of fragments, and the $\Delta V$ of the other fragments is spread from about 0.1 to 1.3 times the $\Delta V$ of the peak. This is the result of the distribution by Eq. 4.9.

## 4.2. NASA STANDARD SATELLITE BREAKUP MODEL

This section describes the most recent NASA fragmentation model, which is the one used in the simulation software. Some significant differences with respect to the previous model are that the fragment size distribution is based on characteristic length (such as diameter for a sphere) rather than mass. Also the area and velocity relations with characteristic length are given as a normal distribution, rather than a single value belonging to a given characteristic length. Additionally this model better estimates the number of fragments smaller than 10 cm, which was underestimated by the classical model. The model is described in (Liou, 2012) and (Johnson et al., 2001).

A comparison of the mass distribution of small fragments is shown in Fig. 4.4. For the standard model the distribution of fragments between 1 mm and 8 cm is plotted. Since the model uses different equations for these than for larger fragments, only the size up to 8 cm is plotted. The area-mass distribution in this model is a normal distribution, but the mean of this distribution was used to create the plot. For the classical model masses up to 10 kg were included, because this model uses a single equation for all sizes. The comparison shows that there is indeed a very large difference, up to about 10 times for the smallest fragments.

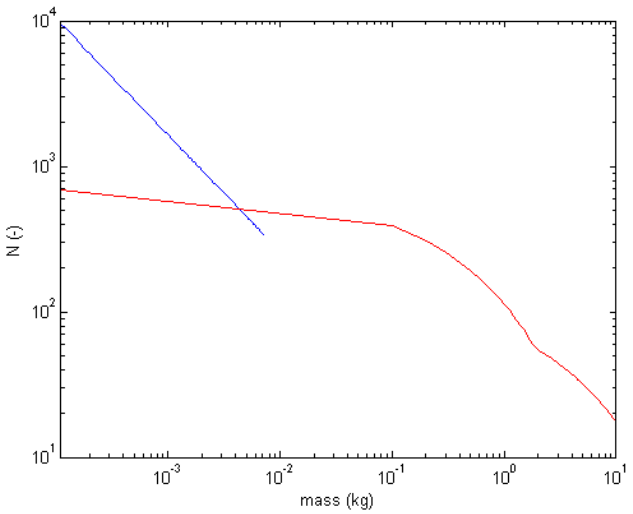


Figure 4.4: Comparison of fragment mass distribution between classical model (red line) and current NASA standard model (blue line).

### 4.2.1. SIZE DISTRIBUTIONS

The fragment size distribution for explosions is given by Eq. 4.10, where $S$ is a unit-less scaling factor depending on the type of explosion and $L_c$ is the characteristic length in m. $N(L_c)$ refers to the number of fragments with a characteristic length larger than $L_c$. According to Liou (2012) there are 6 different scaling factors, however the different groups are not described.

Johnson et al. (2001) mentions that a scaling factor of 1 appears valid for upper stage explosions with masses of 600-1000 kg, but different explosions such as those caused by battery malfunctions or explosions of satellites may require different scaling factors. A comparison of the size distribution by Eq. 4.10 and observed fragments from upper stage breakups is shown in Fig. 4.5.

$$N(L_c)^{EXP} = S \cdot 6 \cdot L_c^{-1.6} \tag{4.10}$$

For collisions a different size distribution is used, as defined by Eq. 4.11. $m_t$ is the total fragment mass, which is still defined in the same way as in the classical model, with Eq. 4.3. A catastrophic collision is now assumed to occur when the ratio of impact energy to target mass is larger than 40 J/g. A catastrophic and non-catastrophic collision use the same size distribution equation, the difference is only in the computation of $m_t$.

$$N(L_c)^{COL} = 0.1 \cdot (m_t)^{0.75} \cdot L_c^{-1.71} \tag{4.11}$$

### 4.2.2. AREA-TO-MASS DISTRIBUTIONS

AMR distributions were developed for both upper stages and spacecraft. Also a separate distribution was derived for objects larger than 11 cm and for those smaller than 8 cm. There is a gap between 8 and 11 cm, for which no separate distribution is derived. A function is used to bridge the gap, but the actual function is not described by Johnson et al. (2001). Therefore in the simulation software developed here the distribution for fragments larger than 11 cm is used for fragments larger than 9.5 cm, while the other distribution is used for fragments smaller than 9.5 cm. The same AMR distribution is used for both explosions and collisions. The equations for >11 cm were derived from observed fragments in orbit, while the equations for <8 cm were derived based on impact tests on Earth, since these fragments are too small to be detected in orbit.

The AMR distribution of upper stage fragments with $L_c \geqslant 11$ cm is given by Eq. 4.12. In this equation $N$ refers to a normal distribution, with a mean $\mu$ and standard deviation $\sigma$.

$$D_{A/M}^{R/B}(\lambda_c, \chi) = \alpha^{R/B}(\lambda_c) N(\mu_1^{R/B}(\lambda_c), \sigma_1^{R/B}(\lambda_c), \chi) + (1 - \alpha^{R/B}(\lambda_c)) N(\mu_2^{R/B}(\lambda_c), \sigma_2^{R/B}(\lambda_c), \chi) \tag{4.12}$$

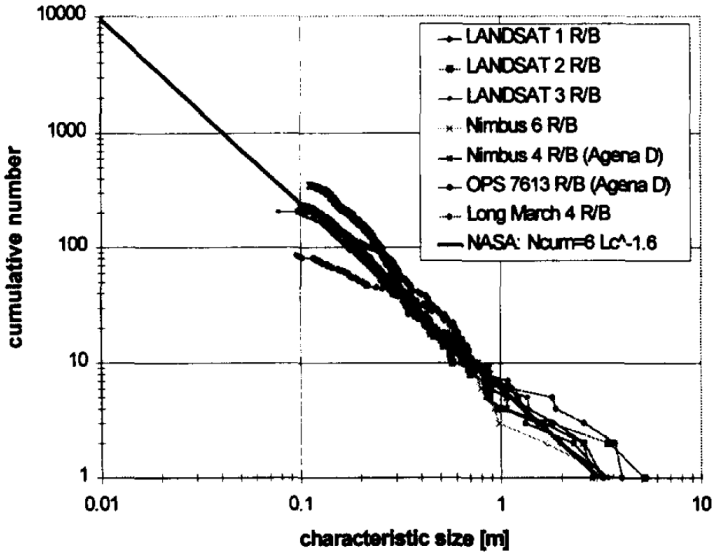


Figure 4.5: Fragment size distributions from seven upper stage breakups and NASA breakup model with $S = 1$ (Johnson et al., 2001).

where $\lambda_c = \log_{10}(L_c)$
$\chi = \log_{10}(A/M)$ is the variable in the distribution
$N$ = the normal distribution function: $N(\mu,\sigma,\chi) = \frac{1}{\sigma\sqrt{2\pi}} e^{-\frac{(\chi-\mu)^2}{2\sigma^2}}$

$$\alpha^{R/B} = \begin{cases} 1 & \lambda_c \leqslant -1.4 \\ 1 - 0.3571(\lambda_c + 1.4) & -1.4 < \lambda_c < 0 \\ 0.5 & \lambda_c \geqslant 0 \end{cases}$$

$$\mu_1^{R/B} = \begin{cases} -0.45 & \lambda_c \leqslant -0.5 \\ -0.45 - 0.9(\lambda_c + 0.5) & -0.5 < \lambda_c < 0 \\ -0.9 & \lambda_c \geqslant 0 \end{cases}$$

$$\sigma_1^{R/B} = 0.55$$

$$\mu_2^{R/B} = -0.9$$

$$\sigma_2^{R/B} = \begin{cases} 0.28 & \lambda_c \leqslant -1.0 \\ 0.28 - 0.1636(\lambda_c + 1) & -1.0 < \lambda_c < 0.1 \\ 0.1 & \lambda_c \geqslant 0.1 \end{cases}$$

A similar distribution for spacecraft fragments is shown in Eq. 4.13. In Fig. 4.6 such a distribution function is plotted together with data of observed spacecraft fragments with sizes between 11.2 cm and 35 cm.

$$D_{A/M}^{S/C}(\lambda_c,\chi) = \alpha^{S/C}(\lambda_c) N(\mu_1^{S/C}(\lambda_c), \sigma_1^{S/C}(\lambda_c), \chi) + (1 - \alpha^{S/C}(\lambda_c)) N(\mu_2^{S/C}(\lambda_c), \sigma_2^{S/C}(\lambda_c), \chi) \tag{4.13}$$

$$\alpha^{S/C} = \begin{cases} 0 & \lambda_c \leqslant -1.95 \\ 0.3 + 0.4(\lambda_c + 1.2) & -1.95 < \lambda_c < 0.55 \\ 1 & \lambda_c \geqslant 0.55 \end{cases}$$

$$\mu_1^{S/C} = \begin{cases} -0.6 & \lambda_c \leqslant -1.1 \\ -0.6 - 0.318(\lambda_c + 1.1) & -1.1 < \lambda_c < 0 \\ -0.95 & \lambda_c \geqslant 0 \end{cases}$$

$$\sigma_1^{S/C} = \begin{cases} 0.1 & \lambda_c \leqslant -1.3 \\ 0.1 + 0.2(\lambda_c + 1.3) & -1.3 < \lambda_c < -0.3 \\ 0.3 & \lambda_c \geqslant 0.3 \end{cases}$$

$$\mu_2^{S/C} = \begin{cases} -1.2 & \lambda_c \leqslant -0.7 \\ -1.2 - 1.333(\lambda_c + 0.7) & -0.7 < \lambda_c < -0.1 \\ -2.0 & \lambda_c \geqslant -0.1 \end{cases}$$

$$\sigma_2^{S/C} = \begin{cases} 0.5 & \lambda_c \leqslant -0.5 \\ 0.5 - (\lambda_c + 0.5) & -0.5 < \lambda_c < -0.3 \\ 0.3 & \lambda_c \geqslant -0.3 \end{cases}$$

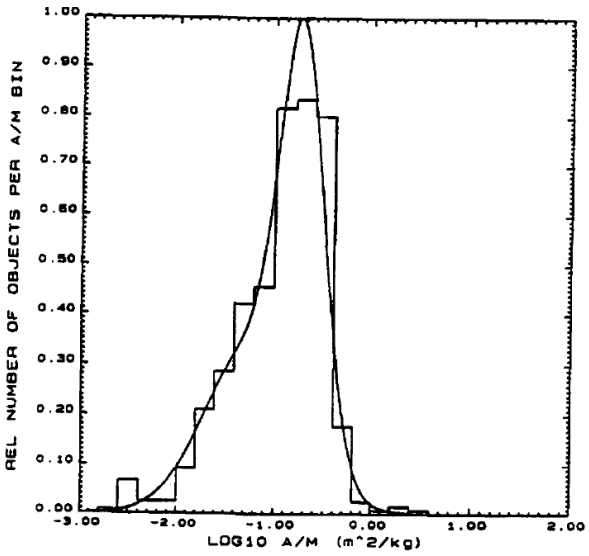


Figure 4.6: Fragment AMR distribution function (Eq. 4.13, the smooth curve in the plot) matched to observed debris with characteristic lengths between 11.2 and 35 cm (Johnson et al., 2001).

For objects with $L_c \leqslant 8$ cm the model has a single distribution function for both spacecraft and upper stages. This distribution is given by Eq. 4.14

$$D_{A/M}^{SOC}(\lambda_c, \chi) = N(\mu^{SOC}(\lambda_c), \sigma^{SOC}(\lambda_c), \chi) \tag{4.14}$$

$$\mu^{SOC} = \begin{cases} -0.3 & \lambda_c \leqslant -1.75 \\ -0.3 - 1.4(\lambda_c + 1.75) & -1.75 < \lambda_c < -1.25 \\ -1.0 & \lambda_c \geqslant -1.25 \end{cases}$$

$$\sigma^{SOC} = \begin{cases} 0.2 & \lambda_c \leqslant -3.5 \\ 0.2 + 0.1333(\lambda_c + 3.5) & \lambda_c > -3.5 \end{cases}$$

The average cross-sectional area, $A$ is modelled as Eq. 4.15.

$$\begin{array}{ll} A = 0.540424 L_c^2 & L_c < 0.00167 \text{ m} \\ A = 0.556945 L_c^2 & L_c \geqslant 0.00167 \text{ m} \end{array} \tag{4.15}$$

The mass of a fragment can be found by simply dividing the area by the area-to-mass ratio, as shown in Eq. 4.16.

$$M = \frac{A}{(A/M)} \tag{4.16}$$

### 4.2.3. $\Delta V$ DISTRIBUTIONS

For the $\Delta V$ of fragments there are also distribution functions, similar to those for the area-to-mass ratio. The distributions for explosion fragments and collision fragments are given by Eqs. 4.17 and 4.18 respectively. An example ejection velocity distribution for upper stage explosions is shown in Fig. 4.7.

$$D_{\Delta V}^{EXP}(\chi, \nu) = N(\mu^{EXP}(\chi), \sigma^{EXP}(\chi), \nu) \tag{4.17}$$

$$\begin{aligned}
&\chi = \log(A/M) \\
&\nu = \log(\Delta V) \\
&\mu^{EXP} = \text{mean} = 0.2\chi + 1.85 \\
&\sigma^{EXP} = \text{standard deviation} = 0.4
\end{aligned}$$

$$D_{\Delta V}^{COL}(\chi, \nu) = N(\mu^{COL}(\chi), \sigma^{COL}(\chi), \nu) \tag{4.18}$$

$$\begin{aligned}
&\mu^{COL} = 0.9\chi + 2.9 \\
&\sigma^{COL} = 0.4
\end{aligned}$$

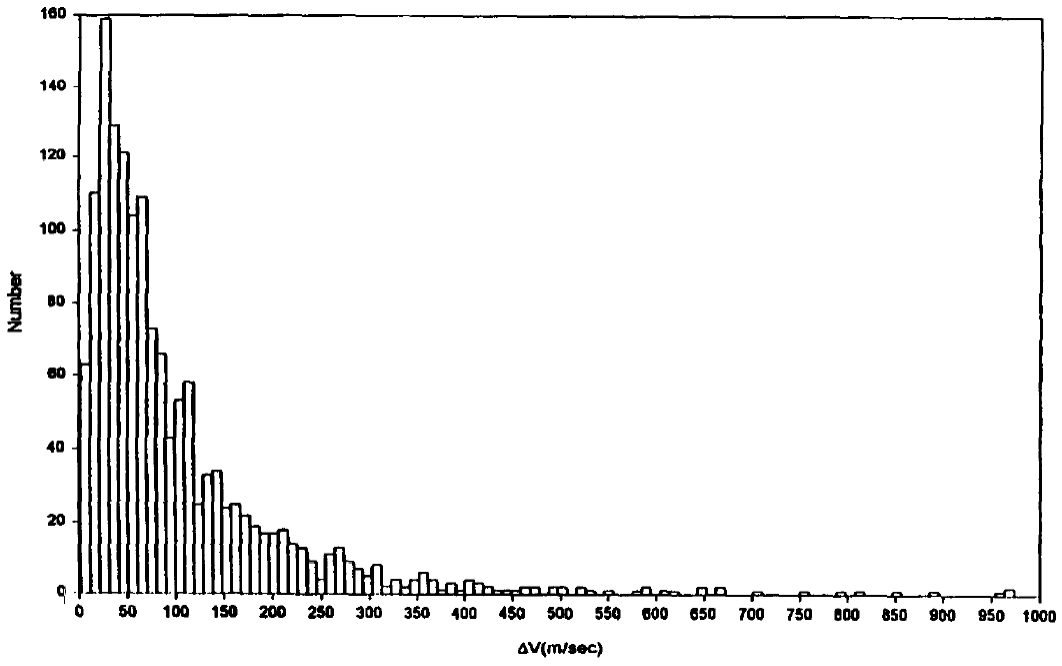


Figure 4.7: Ejection velocity distribution of 1486 observed fragments from Delta, Ariane and Cosmos upper stages (Johnson et al., 2001).

## 4.3. MODIFIED LOW-VELOCITY COLLISION MODEL

This section describes possible modifications to the NASA standard breakup model, for collisions with low velocities. Hanada (2000) compared results of low-velocity impact tests with the NASA standard breakup model. The impact tests were done at velocities <300 m/s which are typical for GEO, while the NASA model is based on LEO collisions with collision velocities of 3.0 to 7.6 km/s, typically referred to as hyper-velocity (Hanada and Liou, 2008). The tests used a simulated spacecraft wall as target.

The reason for investigating low-velocity impacts is that in GEO collision velocities between intact satellites are much smaller than in LEO. Satellites in GEO can reach up to 15° inclination, while they all have approximately circular orbits. The circular velocity is also lower than in LEO. This results in a collision velocity of at most 810 m/s. Collisions with upper stages in GTO can reach up to 1500 m/s.

The results of a comparison with the NASA model were the following (Hanada, 2000; Hata et al., 2003; Hanada et al., 2005):

- The size distribution function (Eq. 4.11) describes a correct trend, but requires a scaling factor to not underestimate the number of fragments. Eq. 4.19 is suggested as modified size distribution.
- The AMR as function of $L_c$ (Eq. 4.15) matches well with the test results.
- The AMR distribution model has some differences with respect to the test results, but these could be due to different materials used in the test. Therefore no modification are suggested to this distribution.
- The $\Delta V$ distribution of the model differs from the results. A different mean and standard deviation are suggested as shown in Eq. 4.20.

$$N(L_c)^{COL} = 0.6 \cdot (m_t)^{0.75} \cdot L_c^{-1.71} \tag{4.19}$$

$$\begin{aligned} \mu &= 0.45\chi + 1.45 \\ \sigma &= 0.27 \end{aligned} \tag{4.20}$$

Later more experiments were done to compare low-velocity and hyper-velocity impacts. (Hanada and Liou, 2008) discusses an impact test with two identical micro-satellites. One is impacted at low velocity (1.5 km/s) and the other at hyper-velocity (4.4 km/s). The results show a similarity in mass distribution for low-velocity and hyper-velocity impacts, which suggests it may be possible to develop a distribution model that is applicable for both low-velocity and hyper-velocity. However such a model has not yet been developed. The paper also does not compare results to the NASA standard breakup model.

More impact tests with micro-satellites are described in (Hanada et al., 2009a) and (Hanada et al., 2009b). These papers also compare results with the NASA model. Micro-satellites were used with layers of CFRP (Carbon Fibre Reinforced Plastic) and GFRP (Glass Fibre Reinforced Plastic). These materials are relatively new and were not yet used in the tests on which the current NASA model is based. It was concluded that the size distribution matched well with the NASA model, but there were significant differences in the mass distribution. Again no model changes have been suggested yet.

Since this thesis is concerned with satellite fragmentations near GEO the suggested low-velocity modifications of Eqs. 4.19 and 4.20 were tested in the simulation software. The size distribution however resulted in very low total masses. therefore in the end only the modification for the $\Delta V$ distribution was included.

## 4.4. IRIDIUM 33 - COSMOS 2251 COLLISION

The NASA standard breakup model does not include modelling the direction of the $\Delta V$ of fragments; it only includes the distribution of the $\Delta V$ magnitude. It might be that fragments are typically ejected in a random direction, similar to an explosion, or perhaps the distribution is affected by the velocity direction of the colliding objects. On February 10, 2009 the Iridium-Cosmos collision occurred, which was the first known catastrophic collision between satellites in orbit. Analyses such as Kelso (2009) and Tan et al. (2013) have investigated this collision and computed the $\Delta V$ distribution of fragments based on observations. These results could provide insight into what kind of distribution may be used in the fragmentation simulation.

A 3D plot of the relative velocities of the fragments (derived from observations) was created by (Kelso, 2009) as shown in Fig. 4.8. The velocities were computed based on TLE data. Fragments were discovered over time after the collision and were propagated backwards to find the velocities at the time of the collision. Some had to be propagated backwards several months, which reduces the accuracy of the velocity results. Therefore only fragments were included of which the position, after the backwards propagation, was within 100 km of the parent object. This left 206 of the 406 catalogued Iridium fragments and 553 of the catalogued Cosmos

fragments. The directions of the velocities seem quite random, although some are concentrated along the flight path for both Iridium and Cosmos.

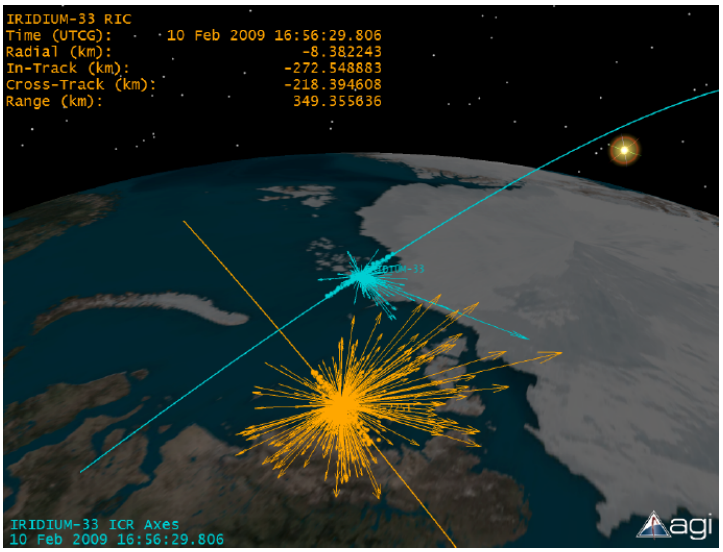


Figure 4.8: 3D plot of relative velocities of fragments from Iridium 33-Cosmos 2251 collision, computed based on TLE data. The yellow vectors represent the Cosmos fragments, and the blue ones the Iridium fragments. The velocities are relative to the velocity of the original satellites before breakup. Iridium 33 was moving from the lower left to upper right and Cosmos 2251 from upper left to lower right (Kelso, 2009).

Another analysis was done by Tan et al. (2013), who included 383 Iridium fragments and 924 Cosmos fragments, which were all fragments catalogued in the first 168 days after the collision occurred. They computed the components of the relative velocity of fragments in down-range, cross-range and radial directions and found Gaussian patterns (i.e. normal distributions) in all of them. Plots of the results from the Iridium fragments are shown in Fig. 4.9, while similar plots of Cosmos and also histogram plots showing the normal distributions for both satellites can be found in Appendix A. It was found that the distributions are slightly shifted in the direction of the velocity of the incoming satellite, for example in Fig. 4.9 (left) Cosmos is coming in from the upper right quadrant, and the highest number of fragments is in the opposing lower left quadrant. Also for Iridium there are slightly more fragments with negative radial velocity, while for Cosmos there are slightly more with positive radial velocity. The authors suggest that this might mean the upper part of Iridium impacted the lower part of Cosmos, however this is not certain.

In conclusion, it is clear that the velocity direction of the colliding satellites (and possible also the point of impact) affects the $\Delta V$ distributions of the fragments. However such effects are currently not included in the fragmentation simulation model. Also there are still fragments going in every direction, just slightly more towards one direction. These are only the results of a single collision, so it is not certain this will be the case for all collision situations. Additionally this is a hyper-velocity collision, results might be different for lower velocity collisions in GEO. Since there are not enough data to model the effect of the velocity direction of the satellites, the $\Delta V$ direction of the fragments is modelled to be completely random in the simulation software. However the sensitivity analysis discussed in Section 7.2 does include one scenario where a non-uniform $\Delta V$ direction distribution is used.

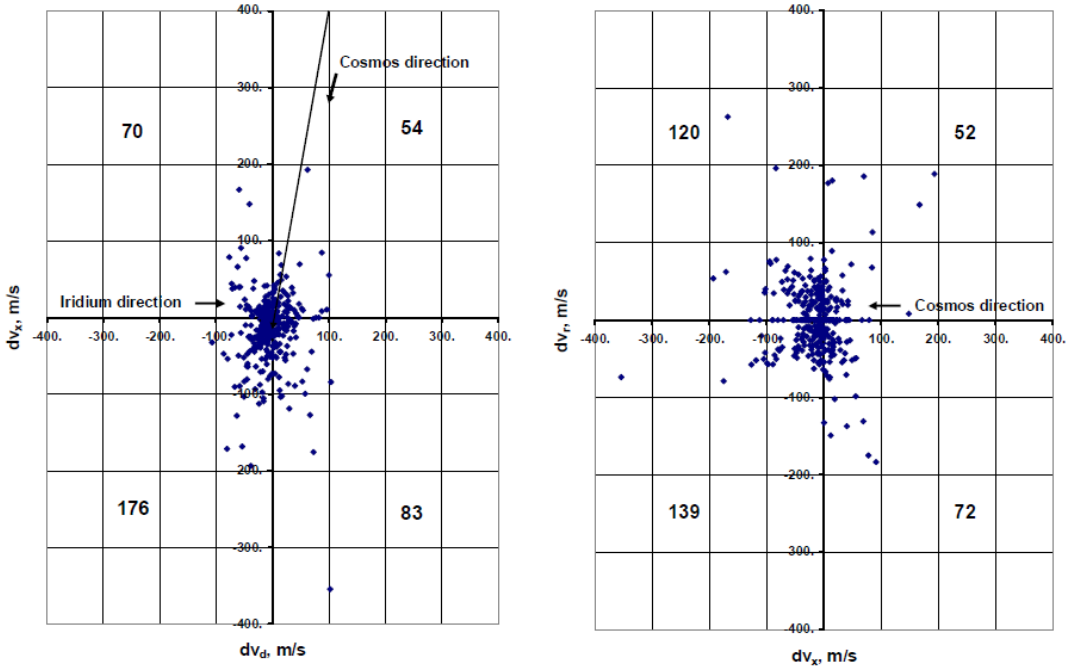


Figure 4.9: Iridium-33 fragments $\Delta V$ in down-range ($dv_d$), cross-range ($dv_x$) and radial ($dv_r$) directions. The directions of the colliding satellites and the number of fragments in each quadrant is also shown (Tan et al., 2013).

# 5

# SOFTWARE

This chapter describes the software that was developed to simulate satellite fragmentations and propagate the resulting debris clouds. Section 5.1 provides an overview of the software that was developed, after which Sections 5.2 and 5.3 describe the validation process for respectively the orbit propagation and fragmentation simulation programs. Section 5.4 discusses the tuning of some of the software parameters and routines.

## 5.1. SOFTWARE OVERVIEW

The perform the simulations required for this thesis, several C++ applications were developed. First an orbit propagator was developed that is able to propagate a single object. This was validated, as discussed in Section 5.2, before it was implemented in a larger program that simulates an explosion and propagates the orbits of the resulting fragments. A separate program was made for collisions, which is very similar to the explosion program except for a few functions, such as the $L_c$ and $\Delta V$ distributions, which have different versions for explosions and collisions. A flowchart that gives an overview of the fragmentation simulation programs is shown in Fig. 5.1.

The flowchart describes the order in which computations are done and also which functions are required at different points throughout the simulation. Sometimes functions from Tudat (TU Delft Astrodynamics Toolbox) have been used. Tudat is a set of C++ libraries containing functions for various astrodynamics applications, developed by the staff and students of the *Astrodynamics and Space Missions* research group at Delft University of Technology. More information on Tudat can be found at `http://tudat.tudelft.nl/projects/tudat/wiki`. When functions from Tudat as well as functions from the Boost libraries are used, this is indicated in the flowchart. For the Sun and Moon ephemerides, which are necessary in the computation of SRP and third-body perturbations, the SPICE ephemerides are used, through the Tudat Spice Interface.

### 5.1.1. INPUT SETTINGS

The software has various input settings that can be modified by the user to handle different simulation scenarios. These input settings are also used to define different test cases, such as the ones shown in Table 6.1. The input settings are explained briefly in this section. Some of the inputs are specific to explosions or collisions, these are referred to as either 'explosion input' or 'collision input'.

- **Orbital Elements** of the intact spacecraft just before the collision/explosion occurs: semi-major axis, eccentricity, inclination, argument of periapsis, right ascension of the ascending node and true anomaly.
- **Seed** of the random number generator (RNG). When the same seed value is used, every simulation will have the same string of (pseudo-)random numbers, which means the exact same results will be computed. The seed number should be changed every time if completely random simulations are desired. Not specifying a seed number results in a standard value being used, which is the same each time.
- $\boldsymbol{L_c}$ **lower limit**: Limit value below which no fragments are simulated. The number of included fragments will become higher the lower this limit is.

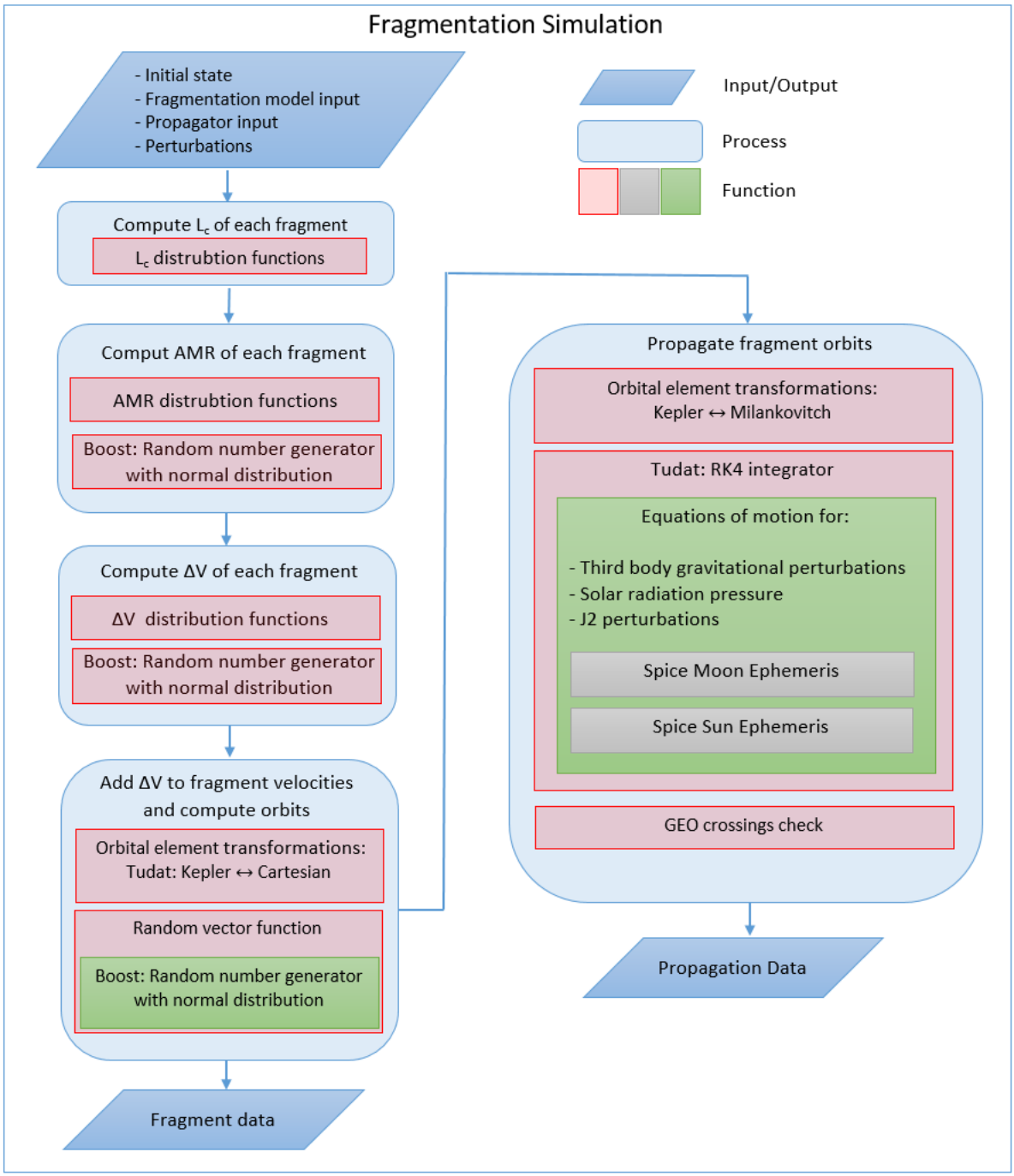


Figure 5.1: Flowchart of fragmentation simulation.

- ***$L_c$* small fragment**: Fragments with a characteristic length above the lower limit but below the small fragment value are considered small fragments. The small fragment factor is applied to these fragments.

- ***$L_c$* upper limit**: Limit value above which fragments are not included in propagation. The fragments above this limit are still generated and saved in the fragment data output, however their orbits are not propagated.

- ***S*, scaling factor**: Explosion input that is used in the $L_c$ distribution function for explosions. A higher scaling factor results in more fragments and therefore a higher total mass. An appropriate scaling factor should be chosen depending on the mass of the exploding object.

- **Small fragment factor**: This input can be used to specify that only a part of the small fragments is included in the propagation, which can reduce computation time when there is a very large number of small fragments. For example if the small fragment factor is set to 20, only every $20^{\text{th}}$ fragment is included. If all fragments should be included, either the small fragment factor can be set to 1 or the small fragment $L_c$ can be set equal to the lower limit.

- **Intact satellite mass**: Collision input that is used in the $L_c$ distribution function for collisions, similar to the scaling factor input for explosions.

- **Projectile mass**: Collision input that specifies the mass of an object that collides with the 'intact satellite mass'. Both masses and the collision velocity are used to compute whether a collision is catastrophic and if not, the total mass of the fragments is computed. Note that although a collision would result in fragments of both objects, only the fragmentation of the 'intact satellite mass' is simulated. To also simulate the fragmentation of the projectile mass the simulation can be repeated with the two masses interchanged in the input settings.

- **Collision velocity**: Collision input that specifies the relative velocity between the colliding objects.

- $\boldsymbol{C_R}$: Reflectivity

- **Target mass**: Mass of hypothetical GEO satellite that is used to compete whether fragments that cross GEO could cause a catastrophic collision if they were to collide with a GEO satellite. This mass is also used in the computation of weighted crossings.

- **Crossing distance**: The crossing distance is used to compute whether fragments make GEO crossings. This is done by assessing the distance between the point where an orbit intersects the equatorial plane and the closest point on the geostationary orbit. If the distance is smaller than the specified crossing distance, it is counted as a crossing. Fragments are integrated with step-sizes equal to one orbital revolution and at every step crossings are computed.

- **Start date**: The date at which the fragmentation occurs and therefore the date at which the orbit propagation starts. The date is relevant for the positions of the Moon and Sun relative to Earth.

- **Duration**: The duration over which the fragments are propagated.

- **Perturbations**: Each perturbation force can be separately switched on or off. The included perturbation forces are $J_2$, third body gravitational perturbations by the Sun, third body gravitational perturbations by the Moon and solar radiation pressure.

### 5.1.2. OUTPUT

Output files with different types of data. First two files are created after the fragment characteristics are computed. One file is created containing the fragment data for all fragments with $L_c$ above the lower limit, and another containing the fragment data for only the fragments that are included in the propagation. For each fragment the following parameters are written in the output file: characteristic length, AMR, area, mass, $\Delta V$, x/y/z components of a unitvector in the $\Delta V$ direction and the Kepler elements.

There are also output files containing propagation data. One file is saved before the propagation and one after every year of propagation, each containing the data for all fragments at that point in time. Such a file contains for each fragment the Kepler elements, the scaled Milankovitch elements (which are the ones used by the integrator) and the total number of crossings, weighted crossings and catastrophic crossings.

### 5.1.3. RANDOM UNIT VECTORS FOR $\Delta V$ DISTRIBUTION

For the $\Delta V$ distribution it is necessary to generate random directions in which the $\Delta V$ is added to the initial velocity. In the software this is done by generating random unit vectors, with a uniform distribution over a sphere. The vectors are created through the following method:

1. Create a random vector by generating x-, y- and z-components with a normal distribution with mean = 0 and standard deviation = 1. This generates vectors with uniform distribution over a sphere.

2. Check if the norm is < 0.0001 and if so, generate a new random vector to replace the initial one. This prevents problems with dividing by small numbers when normalizing the vector.

3. Normalize the vector. The vector is now a unit vector with random direction and creating many vectors will result in a uniform distribution over a sphere.

## 5.2. VALIDATION OF ORBIT PROPAGATOR

This section describes the validation process of the orbit propagator. The software is validated by comparing results obtained using the software to results of other research, to ensure that the software is working correctly. Note that initially a DOPRI8 integrator was used, which is why the step-sizes are longer than 1 day. At the end of the validation the results of using an RK4 integrator were compared to the DOPRI8 results and the RK4 integrator was chosen.

### 5.2.1. ORBITAL ELEMENT TRANSFORMATIONS

For most of the orbital elements transformation functions are already included in Tudat. However the equations of motion that are used in this thesis are based on Milankovitch elements, which are unconventional and are not included in Tudat. Therefore two new functions were developed to convert from Kepler to Milankovitch elements and back.

These functions are tested by setting an initial state with Kepler elements, then converting to Milankovitch elements, back to Kepler elements and again to Milankovitch elements. If the functions are working correctly, the elements should be the same before and after transformation. If they are the same, this does not fully guarantee that there are no errors in the code, but it is unlikely, as the error would have to be the same for both transformations, while they use different functions.

The results of the test are shown in Table 5.1. Both the Kepler and Milankovitch elements are the same before transformation as after transformation, except for the true anomaly. However this is intended, since the Milankovitch elements used here do not contain an element for the position, as it is not used in averaged dynamics. Therefore, the true anomaly is set to 0 when converting from Milankovitch to Kepler elements. The results can also be used to verify that the norm of the eccentricity vector from the Milankovitch elements is equal to the eccentricity in Kepler elements, and the norm of the angular momentum vector is equal to the angular momentum computed from the Kepler elements.

Table 5.1: Results of orbital element transformation test. The test was performed by starting with an initial orbit in Kepler elements, then transforming subsequently to Milankovitch, back to Kepler, and again to Milankovitch elements.

| **Kepler elements** | $a$ (m) | $e$ (-) | $i$ (°) | $\omega$ (°) | $\Omega$ (°) | $\theta$ (°) |
|---|---|---|---|---|---|---|
| before transformation | 16378136.3 | 0.20000000 | 35.000000 | 80.000000 | 110.000000 | 250.00000 |
| after transformation | 16378136.3 | 0.20000000 | 35.000000 | 80.000000 | 110.000000 | 0.0000000 |
| **Milankovitch elements** | $H_x$ ($m^2$/s) | $H_y$ ($m^2$/s) | $H_z$ ($m^2$/s) | $e_x$ (-) | $e_y$ (-) | $e_z$ (-) |
| before transformation | 4.26691e+010 | 1.55303e+010 | 6.48487e+010 | -0.16349 | -0.0225468 | 0.112973 |
| after transformation | 4.26691e+010 | 1.55303e+010 | 6.48487e+010 | -0.16349 | -0.0225468 | 0.112973 |

Another test was done by taking an initial Kepler state with zero inclination and eccentricity, and converting to Milankovitch elements. The resulting eccentricity vector components should be zero and the angular momentum vector should only have a z-component. The results are shown in Table 5.2 and are as expected.

Table 5.2: Results of orbital element transformation test with 0 inclination and eccentricity.

| **Kepler elements** | $a$ (m) | $e$ (-) | $i$ (°) | $\omega$ (°) | $\Omega$ (°) | $\theta$ (°) |
|---|---|---|---|---|---|---|
| before transformation | 1.63781e+007 | 0.00000 | 0.00000 | 80.000 | 110.000 | 250.000 |
| **Milankovitch elements** | $H_x$ ($m^2$/s) | $H_y$ ($m^2$/s) | $H_z$ ($m^2$/s) | $e_x$ (-) | $e_y$ (-) | $e_z$ (-) |
| after transformation | 0.00000 | 0.00000 | 8.07981e+010 | 0.00000 | 0.00000 | 0.00000 |

### 5.2.2. J2 PERTURBATIONS

The J2 perturbations were tested by propagating an orbit with the following settings:

- Initial orbit: circular, geosynchronous altitude, 20° inclination
- Perturbations: $J_2$
- Start date: January 1, 1900
- Interval: 70 years
- Stepsize: 2 days

A non-zero inclination was chosen since otherwise there are no perturbations due to $J_2$. All orbital elements except for Ω stayed constant, which is expected. Some of the results are shown in Fig. 5.2. There were very small discrete changes in the semi-major axis, which are probably caused by round-off errors. These changes do not significantly affect the results, as the magnitude is of the order $10^{-10}$ km. Ω reduces at a constant rate, starting at 0° and ending at 37.697°, for a total change of -322.303° over 70 years.

The change in Ω due to $J_2$ over a single orbital revolution can also be estimated using Eq. 5.1 (Wakker, 2010b). Using this equation, the change in Ω over 70 years would be -322.284°, a difference of only 0.019° compared to the results found using the orbit propagator.

$$\Delta\Omega_{2\pi} = -3\pi J_2 \frac{R^2}{r^2} \cos i \tag{5.1}$$

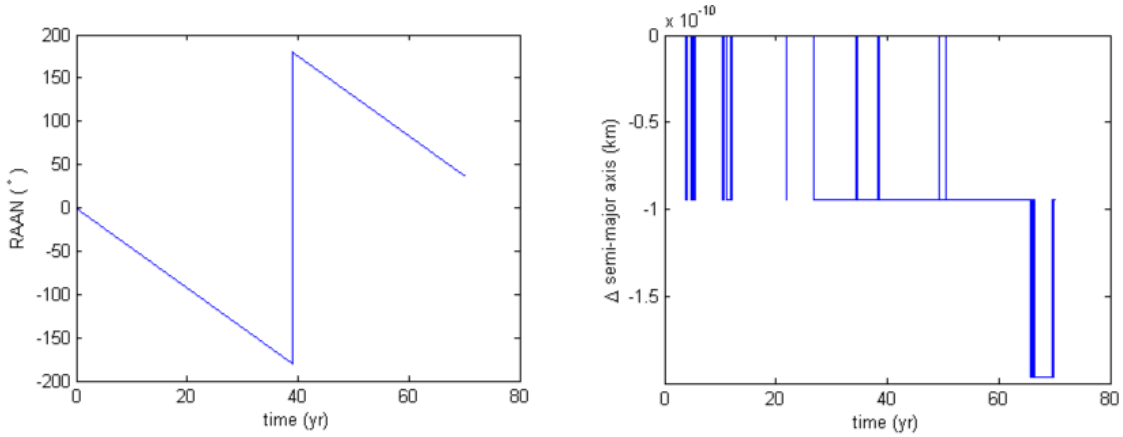


(a) Ω evolution

(b) Semi-major axis difference from initial value

Figure 5.2: Results of 70-year orbit propagation of an object starting in an orbit with geostationary altitude and 20° inclination, with only $J_2$ perturbations

### 5.2.3. THIRD-BODY PERTURBATIONS BY SUN AND MOON

The third-body perturbations were tested by propagating an orbit with the following settings:

- Initial orbit: geostationary orbit
- Perturbations: $J_2$ and third-body Sun and Moon
- Start date: January 1, 1900
- Interval: 70 years
- Stepsize: 2 days

Both $J_2$ and third-body perturbations are included, so that the results can be compared to the orbit evolution of intact GEO satellites (which are not strongly affected by SRP) and also results of similar research with these perturbations. The inclination and RAAN evolutions are plotted in Fig. 5.3. The other orbital elements stayed constant. The inclination increases to about 15° over 53 years, which is similar to the behaviour known from

non-operational geostationary satellites (see Fig. 2.2 for example). The RAAN is slowly reducing from about 100° to -100° in the first 50 years. It then decreases very rapidly, while the inclination is reaching a minimum, until it is close to 100° again and then repeats the pattern. In Fig. 2.2 most objects with non-zero inclination are also in the RAAN range between -100 and 100°.

The change in semi-major axis is shown in Fig. 5.4. The semi-major axis is actually supposed to stay constant, due to the averaged dynamics model that is used, but there is a small integration error that is growing over time. The value reaches up to about $10^{-6}$ km which is not problematic.

The inclination-RAAN evolution was also plotted, which can be found in Fig. 5.5. This plot looks similar to one from a different study, shown in Fig. 5.6, where the same averaged dynamics model was used.

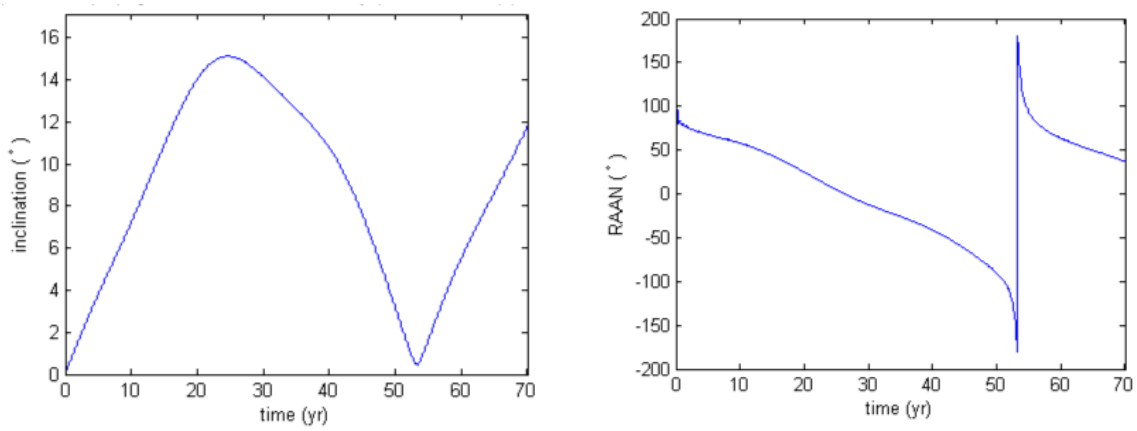


(a) inclination evolution

(b) Ω evolution

Figure 5.3: Results of 70-year orbit propagation of an object starting in geostationary orbit, with $J_2$ and third-body (Sun and Moon) perturbations.

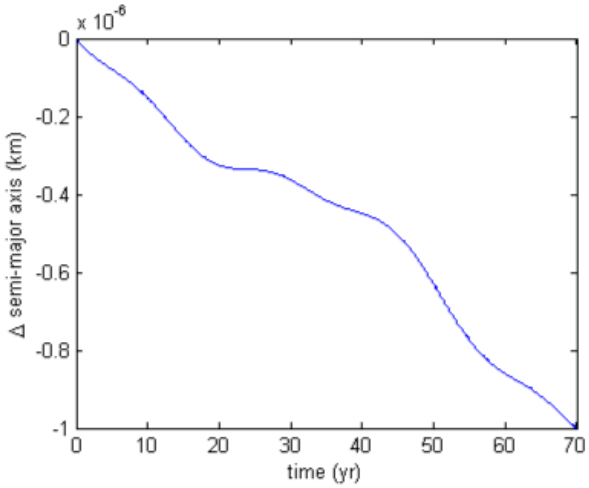


Figure 5.4: Semi-major axis difference from initial value, resulting from 70 year orbit propagation of object starting in geostationary, with J2 and third body (Sun and Moon) perturbations

### 5.2.4. $J_2$, THIRD-BODY AND SRP PERTURBATIONS

Two tests were done with the inclusion of all perturbation forces. First the results obtained using the averaged model were compared to results obtained using a non-averaged model. The same integrator was used, but with a different state vector and equations of motion. For the non-averaged computation the state vector was Cartesian, with the position coordinates and velocity components. The equations of motion were the velocity

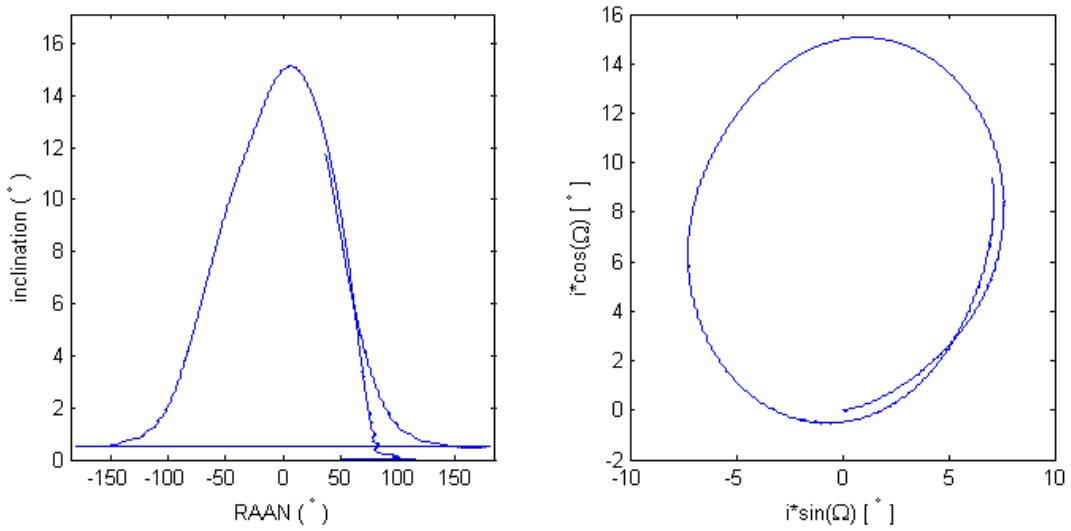


Figure 5.5: Inclination-RAAN evolution, resulting from 70 year orbit propagation of object starting in geostationary, with J2 and third body (Sun and Moon) perturbations

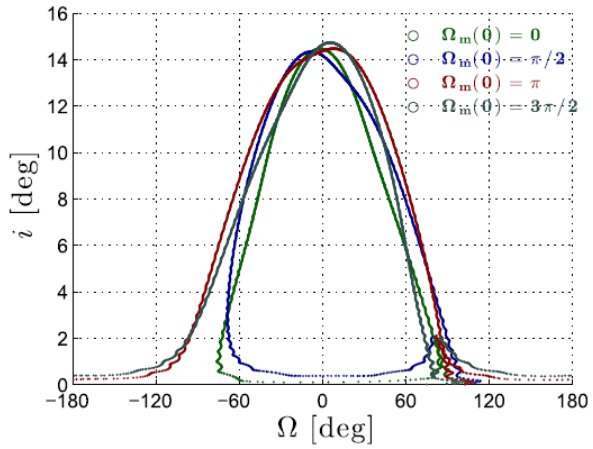


Figure 5.6: Inclination-RAAN evolution from other research, computed with the averaged dynamics model that is also used in this thesis. The results are from a 54 year orbit propagation with J2 and third body (Sun and Moon) perturbations. Note that the results look similar to those shown in Fig. 5.5. In this figure multiple plots are shown for different initial values of $\Omega_m$, which result from different starting dates (Rosengren and Scheeres, 2013).

(for the derivative of the position) and acceleration functions (for the derivative of the velocity components) that have been described in Section 3.3. Also a smaller step-size was necessary to receive similar accuracy. The following settings were used in the propagator:

- Initial orbit: geostationary orbit
- Perturbations: $J_2$, third body Sun, third body Moon, SRP
- Start date: January 1, 1900
- Interval: 100 years
- Step-size: variable step-size of 1 to 20 Julian days (averaged model) and 1 to 120 minutes (non-averaged model)
- Reflectivity: 1.2
- AMR: 17 $m^2$/kg

The results obtained with the averaged and non-averaged models are compared to each other in Fig. 5.7. For all orbital elements the plots nearly overlap each other, which proves that the averaged model provides accurate results, while being much faster. The computation time was about 4.2 seconds for the averaged model and 10 minutes for the non-averaged model. There are some differences in the semi-major axis plot, which are caused by daily variations (i.e. the duration of one orbit revolution) that are averaged out by the averaged model. The difference between the two plots is at most 46.3 km.

The eccentricity and $\omega$ plots have been zoomed in to only show the last 10 years, because otherwise it is not possible to distinguish the separate curves. The results were similar throughout the rest of the interval as well. Also in the $\omega$ plot the peaks of the blue line (from the non-averaged results) are a bit higher. This is probably caused by the fact that there are more data points from the non-averaged results, due to the smaller step-size.

In Fig. 5.7f the amplitude of the RAAN oscillations is increasing over time. This was further investigated to ensure that it is not caused by an error. By testing cases with different starting years, it was found that the amplitude varies over time for most cases, and it is not always increasing. This is probably caused by resonance with lunar nodal regression (also called Saros resonance), because after a period of 18.61 years (the period of lunar nodal regression) roughly the same pattern is seen. There is resonance because the period of inclination and RAAN oscillations for the used area-mass-ratio is close to the lunar nodal regression period. This phenomenon has also been described by Rosengren and Scheeres (2013), who found that the resonance is most important for AMR values between 14 and 22 $m^2$/kg (with a reflectivity of 1.2). Results were also computed with an AMR of 25 $m^2$/kg, where there is no resonance.

Simulations were done with 3-year intervals, with 18.61 years after 1900 for the last test, since this is the period for lunar nodal regression. Only the most interesting results are shown here, in Fig. 5.8. At the starting year 1903 the resonance is most extreme, with the inclination amplitude increasing over time (for the low AMR value, red line). In 1912 the opposite happens; the inclination amplitude is decreasing over time, as well as the RAAN amplitude. For the higher AMR value (blue line), the inclination and RAAN amplitudes are much more consistent throughout the years, which is expected since the AMR value is outside the resonance range. In the RAAN evolution it looks like some peaks are higher than others, however this could also be because the actual peak is not perfectly sampled with the number of data points. Either way the differences between the different starting years are much smaller than with the lower AMR value. At starting year 1918.61 the results are very similar to those with starting year 1900, which further indicates that the differences can be due to the lunar nodal regression. When increasing the starting year by another 18.61 years, similar results were found again, although these are not included here.

The effects of Saros resonance can also be seen in RAAN-inclination plots such as those shown in Fig. 5.9. For the higher AMR value (blue), there is just a circular pattern with small oscillations on top of it. For the lower AMR (red), in the start years where in Fig. 5.8 the strongest resonance effects were seen (1903 and 1912), these are also visible in these plots. The lower AMR results are spiralling outwards or inwards. For 1900 and 1918.61 the results deviate a bit from the circular pattern of the blue line, but not as much. Also in the higher AMR results, there is very little variation between the different starting years.

Another test was done to compare results obtained with the propagator to results of a study by Anselmo and Pardini (2010), who also investigated HAMR debris. The same initial orbit, start date, and $C_R$·AMR were used, resulting in the following propagator settings:

- Initial orbit: $a = 42164.465$ km, $e = 0.0001$, $i = 0.097°$, $\omega = 220°$, $\Omega = 50°$ (a mean anomaly value was also given by Anselmo and Pardini (2010), but it not used here because the model is averaged and therefore does not include such a parameter)
- Perturbations: $J_2$, third body Sun, third body Moon, SRP (Anselmo and Pardini also included $J_{2,2}$ and Earth shadow effects)
- Start date: December 12, 2005, 00:00
- Interval: 40 years (Anselmo and Pardini (2010) shows plots with a 100-year interval, but the ephemerides included with the Tudat Spice Interface do not contain data beyond the year 2050. Therefore a shorter interval was used, which still provides enough data to compare the results).

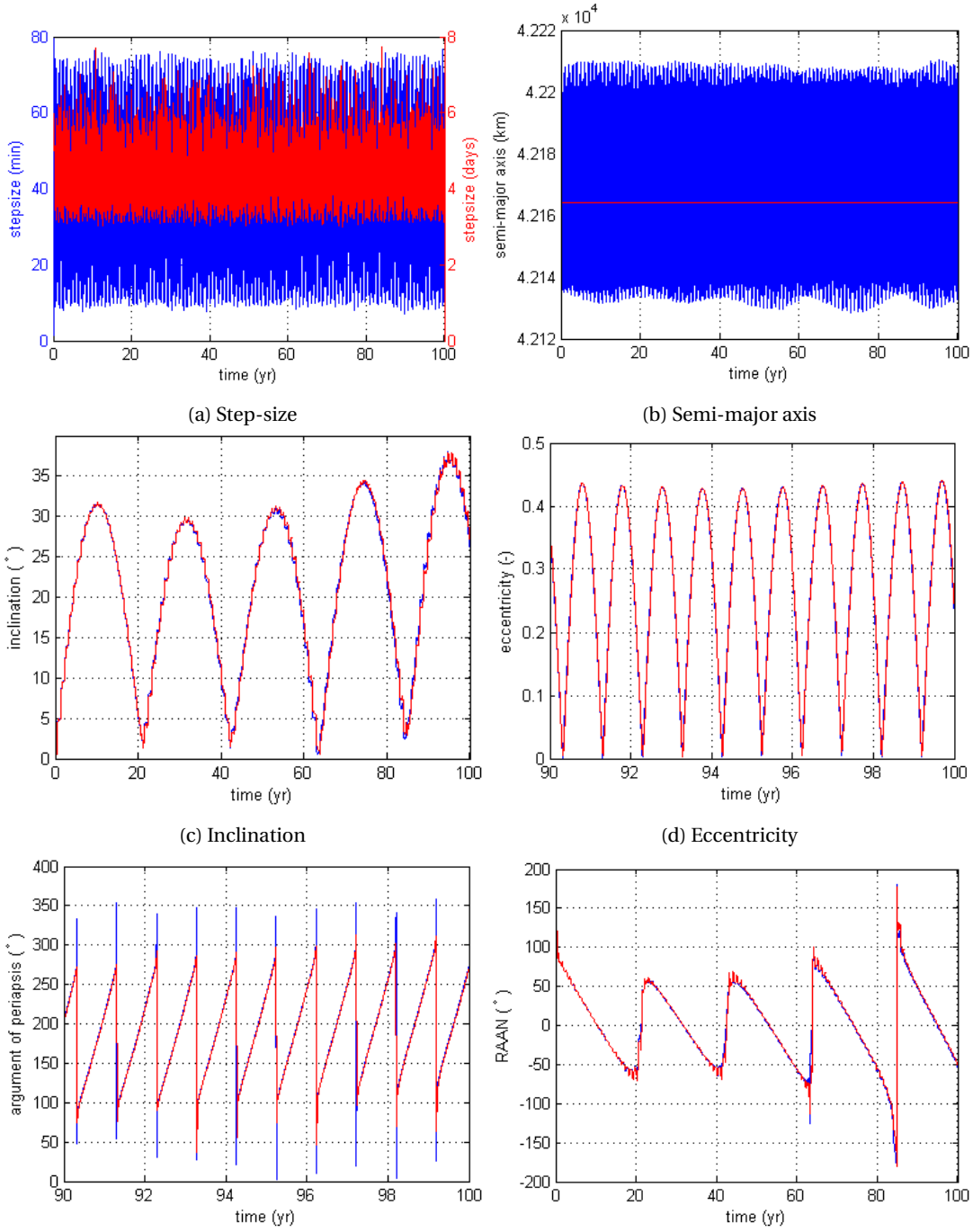


(a) Step-size

(b) Semi-major axis

(c) Inclination

(d) Eccentricity

(e) Argument of periapsis

(f) Right ascension of the ascending node

Figure 5.7: Comparison of orbit propagation with averaged model (red line) and non-averaged model (blue line).

- Step-size: variable step-size of 1 to 120 minutes
- Reflectivity: 1.2
- AMR: 17 $m^2/kg$

The results comparison is shown in Figs. 5.10 and 5.11. The general shape of the plots looks similar, but there are some small differences. For example the second inclination top in Fig. 5.10 is slightly higher (about 2°). Also at about 20 years the eccentricity in the (Anselmo and Pardini, 2010) results drops slightly below

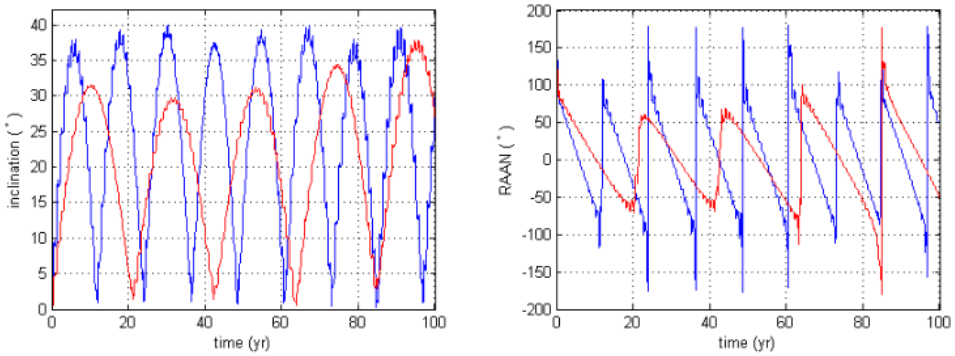


(a) Starting year: 1900

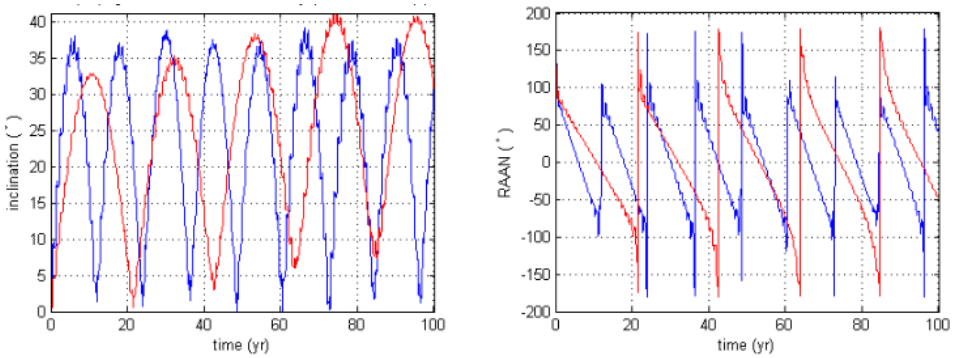


(b) Starting year: 1903

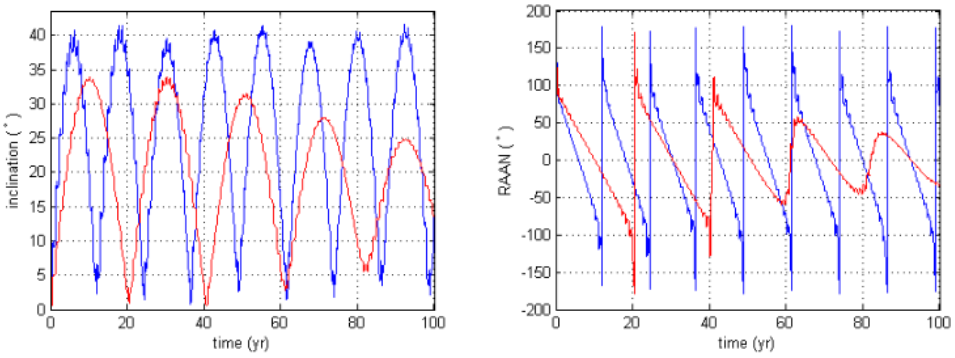


(c) Starting year: 1912

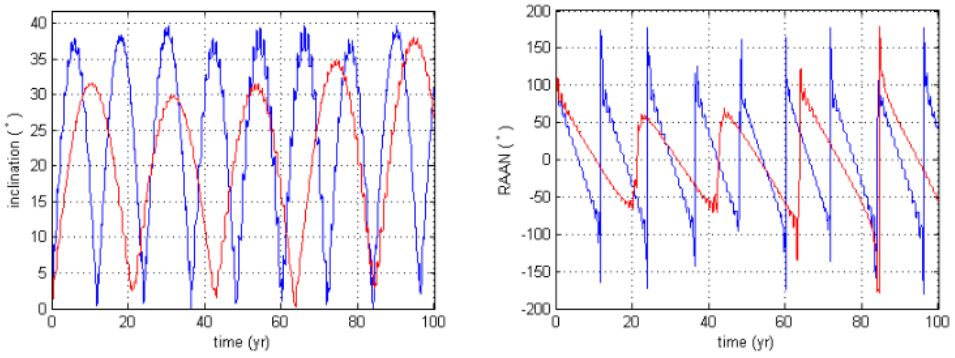


(d) Starting year: 1918.61

Figure 5.8: Comparison of inclination and RAAN evolution for different starting years, for two different area-mass-ratios (17 $m^2$/kg for the red line and 25 $m^2$/kg for the blue line).

0.4 which does not happen for the averaged propagator and (Rosengren and Scheeres, 2013) results. In general the results by the propagator more closely approximate those of Rosengren and Scheeres than those of

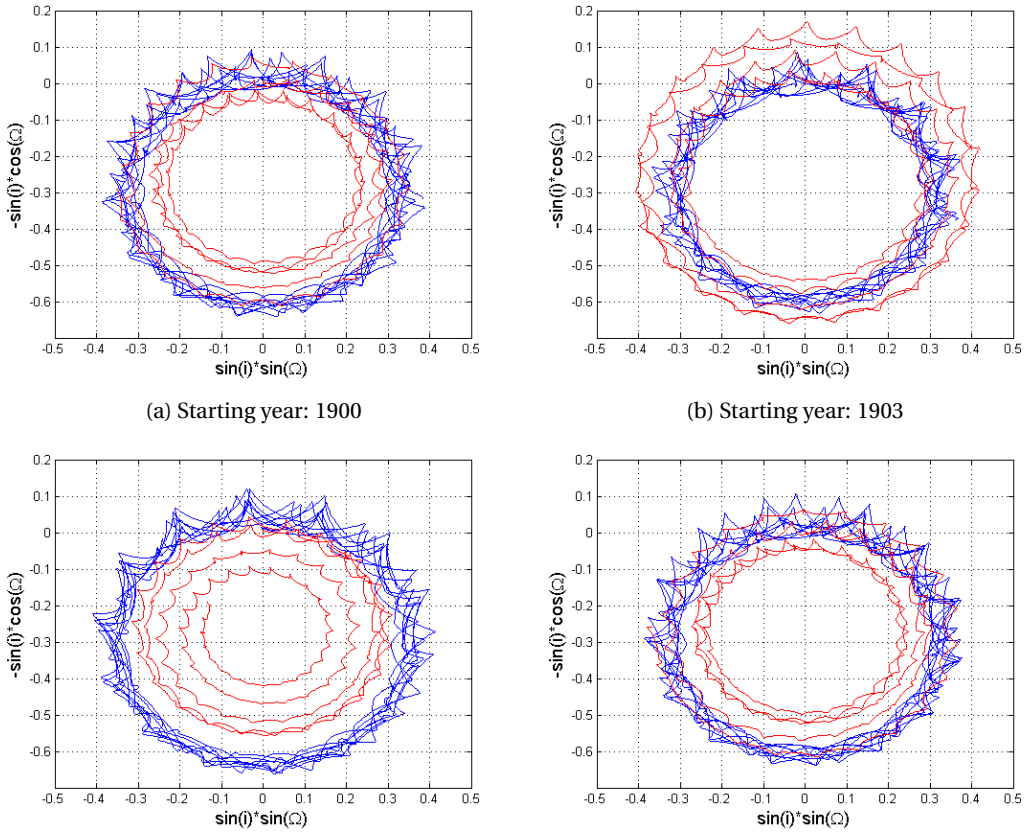


(a) Starting year: 1900

(b) Starting year: 1903

(c) Starting year: 1912

(d) Starting year: 1918.61

Figure 5.9: Comparison of RAAN-inclination plots for different starting years, for two different area-mass-ratios (17 $m^2$/kg for the red line and 25 $m^2$/kg for the blue line.)

Anselmo and Pardini, which is understandable since the averaged model that was developed by Rosengren and Scheeres (2013) is used in the propagator. Anselmo and Pardini (2010) use a non-averaged model, which includes shadow effects and an 8x8 gravity field model (as opposed to averaged, no shadow effects and only $J_2$ gravity field model). Additionally it is possible that a different ephemeris is used, since this is not specified in (Anselmo and Pardini, 2010). Since the results by the propagator do look very similar to the Rosengren and Scheeres (2013) results, the model can be concluded to have been programmed correctly.

To investigate possible causes of the differences between the results, additional simulations were done that included $J_{2,2}$, shadow effects (no SRP when the satellite in the shadow of the Earth) and a Keplerian or circular Earth orbit. For this a non-averaged RK4 propagator was used. A non-averaged model is required because the position of the satellite needs to be known, which is not the case with the averaged model. An attempt was made to use the DOPRI8 integrator with the non-averaged equations, however this resulted in errors when including shadow effects and no results could be computed, therefore an RK4 integrator was used. The results are shown in Fig. 5.12. There are small differences in the inclination and eccentricity evolution, which do bring the results slightly closer to those of (Anselmo and Pardini, 2010) in Fig. 5.10 (the second inclination peak of the blue line is lower and also the eccentricity peaks are slightly lower), however there are still visible differences. Also the semi-major axis amplitude is varying with these additional perturbations and can be more than twice as large as with the nominal perturbations. This could have an effect on the number of possible GEO crossings throughout the orbit evolution.

### 5.2.5. GEO CROSSINGS

The validation with all perturbations showed that shadow effects and $J_{2,2}$ perturbations cause small differences in the orbital elements evolution. Additionally the non-averaged model produced semi-major axis oscillations with a constant peak-to-peak amplitude of about 50 km, which are not included in the averaged

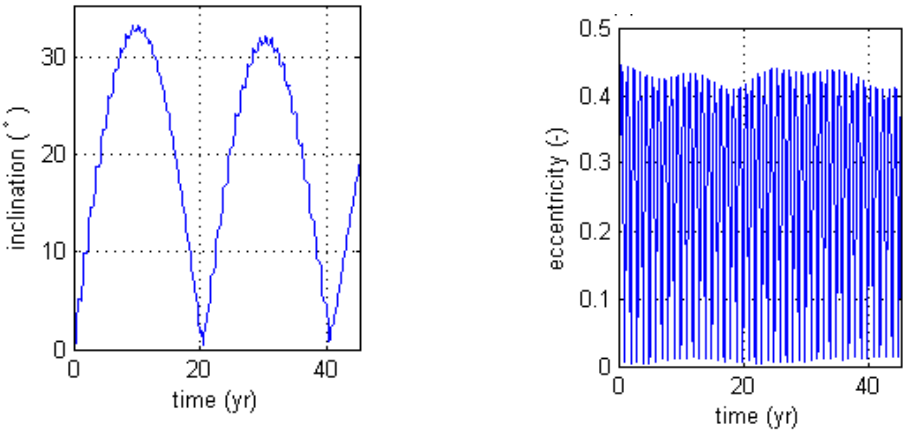


(a) Results from averaged propagator

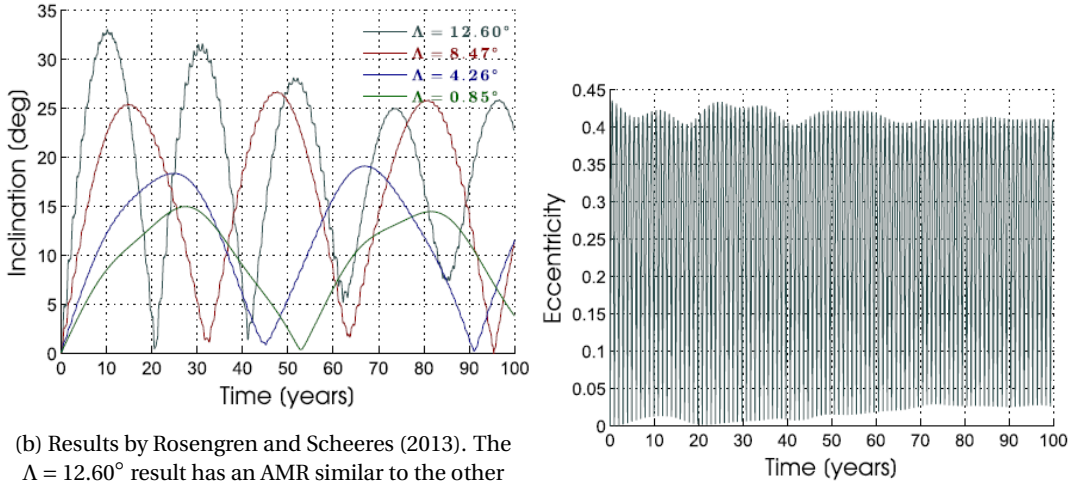


(b) Results by Rosengren and Scheeres (2013). The $\Lambda = 12.60°$ result has an AMR similar to the other figures.

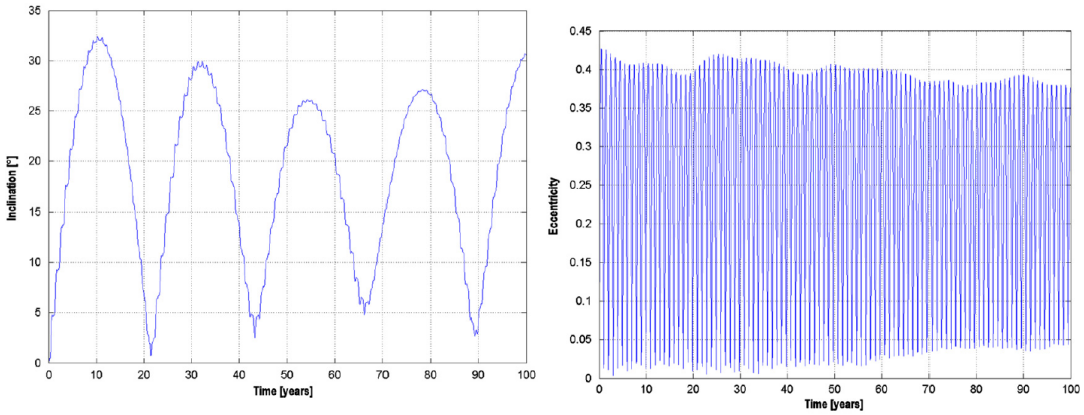


(c) Results by Anselmo and Pardini (2010)

Figure 5.10: Comparison of inclination and eccentricity evolution computed with averaged propagator (top) to results obtained by Rosengren and Scheeres (2013) (middle) and Anselmo and Pardini (2010) (bottom).

model. This amplitude becomes variable when adding shadow effects and can reach up to about 200 km. These differences could have an effect on the number of times an object is crosses the geostationary ring. For this reason tests were done comparing the crossing results from using various model options.

Simulations were done where an object is released in GEO and its orbit is propagated for 150 years. The different options tested were: averaged DOPRI8 with variable step-size and interpolation of results to 1-day steps, averaged DOPRI8 with 1 day step-size, averaged RK4 with 1 day step-size, non-averaged RK4 with standard

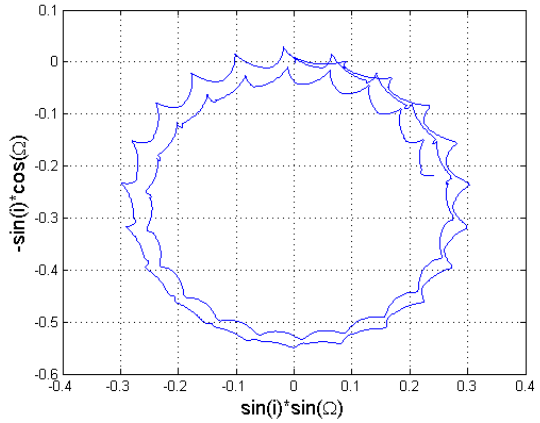


(a) Results from averaged propagator

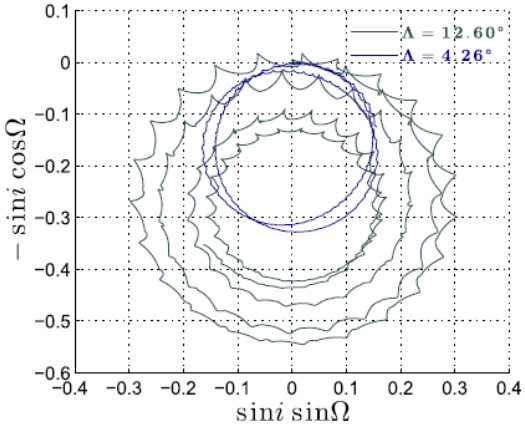


(b) Results by Rosengren and Scheeres (2013). The $\Lambda = 12.60°$ result has an AMR similar to the other figures.

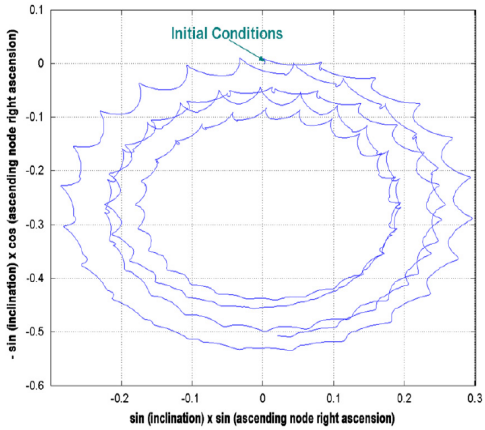


(c) Results by Anselmo and Pardini (2010)

Figure 5.11: Comparison of RAAN-inclination evolution computed with averaged propagator (top left) to results obtained by Rosengren and Scheeres (2013) (top right) and Anselmo and Pardini (2010) (bottom).

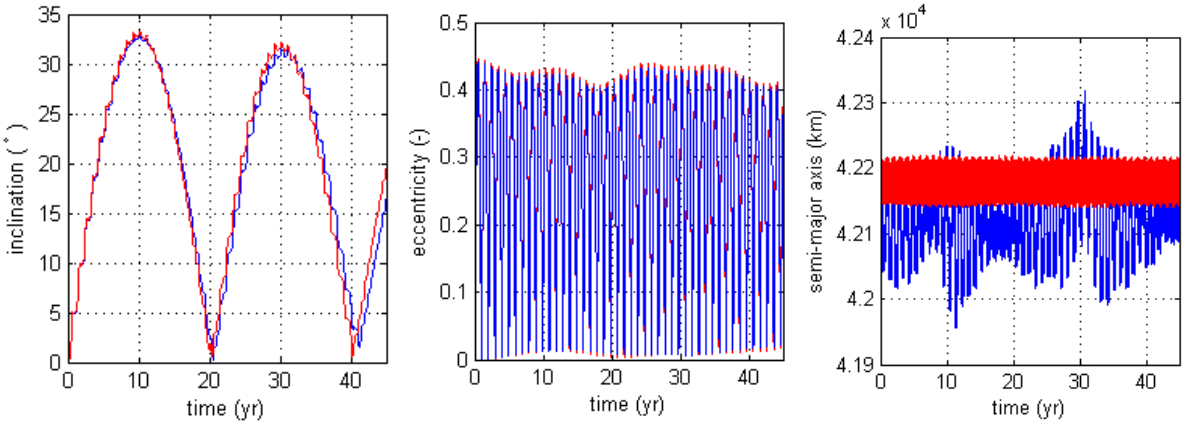


Figure 5.12: Comparison of results with nominal perturbations (red line) to results that included also shadow effects and $J_{2,2}$ (blue line).

perturbations and non-averaged RK4 with shadow effects and $J_{2,2}$ added. The interpolation when using variable step-size is required in order to compute GEO crossings for each orbital revolution. The settings for the different simulation are shown in Table 5.3, while the simulation results are shown in Fig. 5.13.

Table 5.3: Settings for GEO crossings simulations.

| Simulation | A | B | C | D | E |
|---|---|---|---|---|---|
| Propagator | Averaged DOPRI8 | Averaged DOPRI8 | Averaged RK4 | RK4 | RK4 |
| Initial orbit | GEO | | | | |
| $C_R$ | 1.2 | | | | |
| $J_2$ | Yes | | | | |
| 3rd body Sun | Yes | | | | |
| 3rd body Moon | Yes | | | | |
| SRP | Yes | | | | |
| $J_{2,2}$ | No | No | No | Yes | No |
| Shadow | No | No | No | Yes | No |
| Start date | 1-1-1900, 00:00 | | | | |
| Interval | 150 yr | | | | |
| Step-size | Variable | 1 day | 1 day | 150 s | 150 s |

The plots for A, B and C are very close to each other, with their numbers of GEO crossings well within 1% of each other (see Table 5.4, which also shows the computation time for the simulations). All averaged propagator results are therefore very similar, while the non-averaged propagator results show more variations, with a difference in GEO crossings of at most 23 (about 3% of the total). The computation time with the averaged propagators is less than 1% of the non-averaged time. Note that the time for A does not include time required for interpolating the data, as this was done separately from the simulation using Matlab. The maximum number of crossings, if each revolution resulted in 2 crossings, would be 109500. This means only about 0.7% of the equatorial plane intersections is close enough to GEO to be considered a crossing.

Case E has a lower number of GEO crossings than the other options. The reason for this is probably because it does not include shadow or $J_{2,2}$, which results in less variation in the semi-major axis evolution (the amplitude is close to constant). However, in this case one would also expect A,B and C to have less crossings, as these also do not include shadow and $J_{2,2}$. This is possible because with the averaged model, the semi-major axis stays constant. Since GEO was used as initial orbit, the semi-major axis stays at the geostationary value, which means there are at least always crossings when either eccentricity is 0 or inclination is 0 and eccentricity non-zero. I.e. there is one effect reducing the number of crossings, and another increasing it, resulting in a net number of crossings that is very close to option D. The results obtained using the averaged propagator do closely approximate those from the non-averaged propagator, which means it is possible to use the averaged model for assessing GEO crossings. Cases A and C both require a very short computation time, but A still requires interpolation of the data after the simulation, which makes it impossible to compute GEO crossings during the propagation. Therefore option C, the averaged RK4 integrator, is used for all further simulations described in this report. Since most of the validation was done using the averaged DOPRI8 integrator, the orbit evolutions of options A and C were compared to each other as well. The results were nearly identical as shown in Appendix C.

The curves in Fig. 5.13 all follow a similar trend with periods where the curve is less steep for about 20-25 years and then steeper for 5-10 years. However it not clear what is causing this behaviour. The total period is about 30 years, which does not coincide with other periods such as that of the inclination evolution (just over 20 years) or the Moon's RAAN evolution (18.61 years).

Table 5.4: GEO crossings results of simulations described in Table 5.3.

| Simulation | A | B | C | D | E |
|---|---|---|---|---|---|
| Computation time [s] | 4.2 | 16.7 | 6.8 | 2540.2 | 2411.9 |
| Total GEO crossings | 771 | 775 | 773 | 772 | 751 |

The propagator also computes catastrophic crossings and weighted crossings. These were computed for option C of Table 5.3, the results are shown in Fig. 5.14. For this simulation a fragment mass of 100 kg was used, with a target mass of 1000 kg. This fragment mass is relatively large, but it was chosen to ensure there are

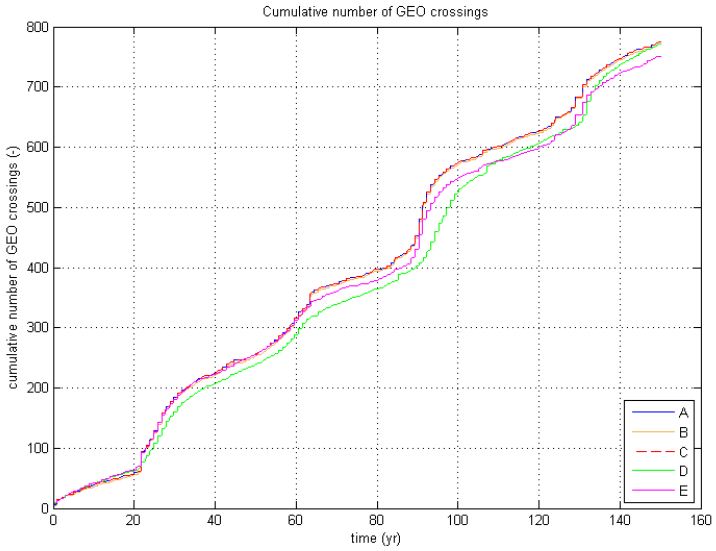


Figure 5.13: GEO crossings computed with propagator settings of Table 5.3.

catastrophic crossings. The catastrophic crossings follow a similar curve as the total crossings, only there are less of them (534 out of 773).

The weighted crossings are only slightly above the catastrophic crossings. It is expected to be above the catastrophic curve, since a catastrophic crossing has a weight of 1, but it also includes the other crossings with weights smaller than 1. The difference however is small, which means that the fragment mass created by non-catastrophic collisions is in total very small compared to that of catastrophic ones.

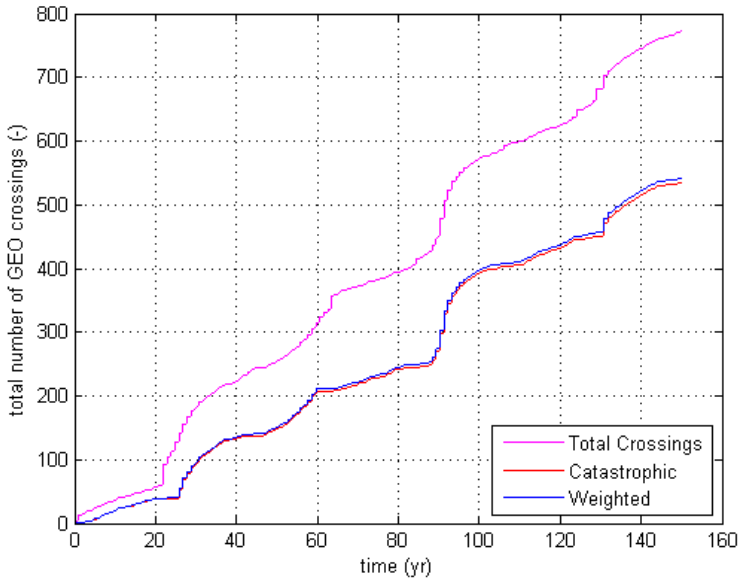


Figure 5.14: GEO crossings computed with propagator settings of Table 5.3.

For each crossing a crossing velocity is also obtained and included in the calculation of catastrophic and weighted crossings. This is the velocity difference of the object crossing GEO, relative to a geostationary satellite in the same position. The crossing velocity values are plotted versus time in Fig. 5.15a. The values follow

a similar pattern to the inclination evolution in Fig. 5.15b. This is expected since GEO has a 0° inclination, so higher values of inclination result in higher crossing velocities. For example the first peak of the inclination plot is at about 32°. If the object intersecting GEO also had a perfectly circular orbit, this would result in a relative velocity of 1629 m/s. Most of the crossing velocity values near this peak are a bit higher, which is caused by eccentricity. At the peaks it also looks as if there are two curves above each other. This has to do with the fact that there are two possible crossings for each revolution, with different true anomalies, which result in different crossing geometries and hence different velocities.

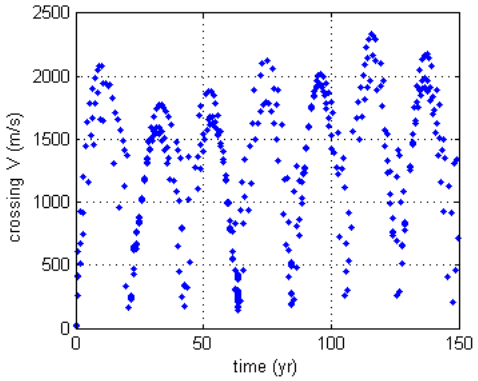


(a) Crossing velocity of GEO crossings computed with propagator settings of option C in Table 5.3.

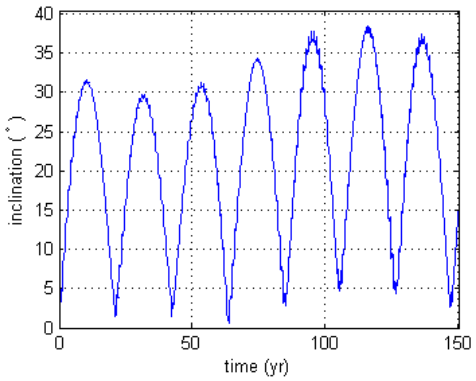


(b) Inclination evolution of orbit propagation computed with settings of option C in Table 5.3.

Figure 5.15: Crossing velocity and inclination evolution.

## 5.3. VALIDATION OF FRAGMENTATION MODEL

### 5.3.1. SIZE DISTRIBUTION

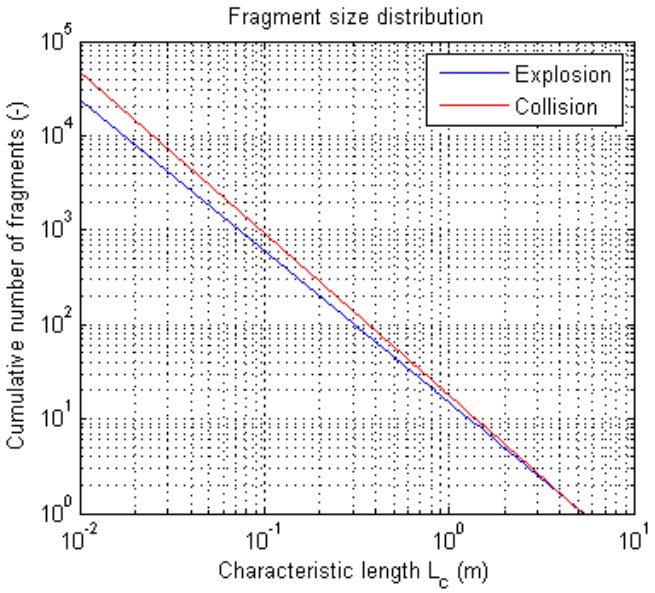


Figure 5.16: Fragment size distribution of simulated explosion with $S = 2.5$ and collision with $M_t = 1000$ kg.

The computed size distributions of an explosion and collision are plotted in Fig. 5.16. For a collision the total fragment mass is directly included in the distribution function, but for an explosion a scaling factor needs to be used. In the literature only a scaling factor of 1 was mentioned, for upper stages with a mass of 600-1000 kg. This scaling factor was tested but resulted in very low masses (around 300 kg) when adding up the mass of each fragment. This is probably caused by the different AMR distributions for upper stages

than for satellites. Through trial and error a scaling factor of 2.5 was found to result in a total mass close to 1000 kg, which was later refined to 2.57 as described in Section 5.4.1. The lines in the plot look similar to the one shown in Fig. 4.5 for an explosion with a scaling factor of 1. With a scaling factor of 2.5 the number of fragments is also 2.5 times higher, which is visible in the plots.

### 5.3.2. AMR DISTRIBUTION

To test whether the generated AMR values of fragments actually follow a normal distribution curve, a large number of fragments was generated with a single $L_c$ value. A histogram plot of the results is shown in Fig. 5.17. A normal distribution curve is fitted to the results, which follows the histogram plot closely. A characteristic length of 8 cm was used. It was necessary to use a smaller than 8 cm, because here the model only uses a single normal distribution, while for fragments larger than 11.2 cm two normal distributions are combined. For the 8 cm characteristic length, the mean and sigma values should be respectively -1.0 and 0.5203, according to Eq. 4.13. Since the numbers are randomly generated, the mean and sigma will not be exactly the same, but with a large number of fragments they should be close. Computing the mean and sigma of the generated fragments resulted in the values -1.003 and 0.5183. This is within 1% of the expected values. The AMR distribution function is therefore working correctly.

The AMR values of fragments from a simulated explosion and collision are plotted versus characteristic length in Fig. 5.18. The plots show a similar pattern, with the average AMR increasing for smaller fragments while they are also more spread out from the average. This is expected since the mean and standard deviation in the model are both larger for small fragments.

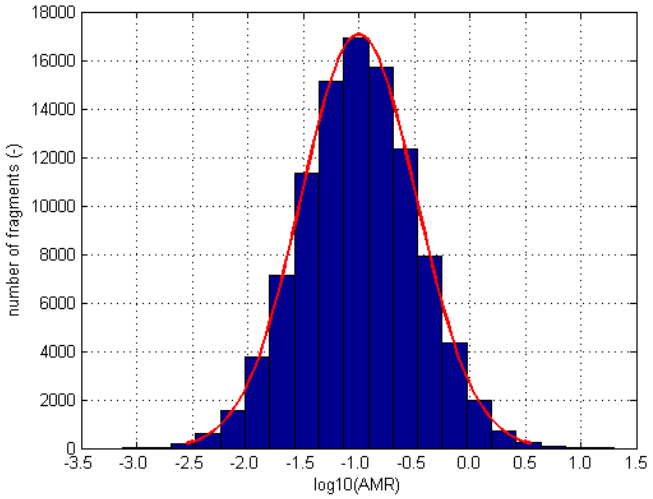


Figure 5.17: Histogram plot with fitted normal distribution curve of AMR values of $10^5$ fragments with $L_c = 8$ cm.

### 5.3.3. $\Delta V$ DISTRIBUTION

An explosion was simulated with a scaling factor of 2.57 (which results in a total mass of about 1000 kg, see Section 5.4.1) and a collision simulation of a 1000 kg mass. The $\Delta V$ results of the fragments are plotted on a logarithmic scale in Fig. 5.19. The plots look similar to the AMR distribution plots shown in Fig. 5.18, which is expected since the distribution is modelled in a similar way, only the mean and standard deviation values are different. The histogram plots also looks like a normal distribution.

Another histogram plot was made with the $\Delta V$ on a uniform scale, see Fig. 5.20. Only the fragments with $L_c \geqslant 10$ cm were plotted, so that the results can be compared to Fig. 5.21, which shows a similar plot for observed fragments from upper stage explosions. The plots have a very similar pattern, although the upper stages plot has higher $\Delta V$ values. The NASA breakup model contains a single $\Delta V$ distribution for both upper stages and satellites, however the AMR distribution for fragments $\geqslant 11$ cm is different, and this AMR is used as input for the $\Delta V$ distribution, thus resulting in different $\Delta V$ values for upper stages and satellites. Similar

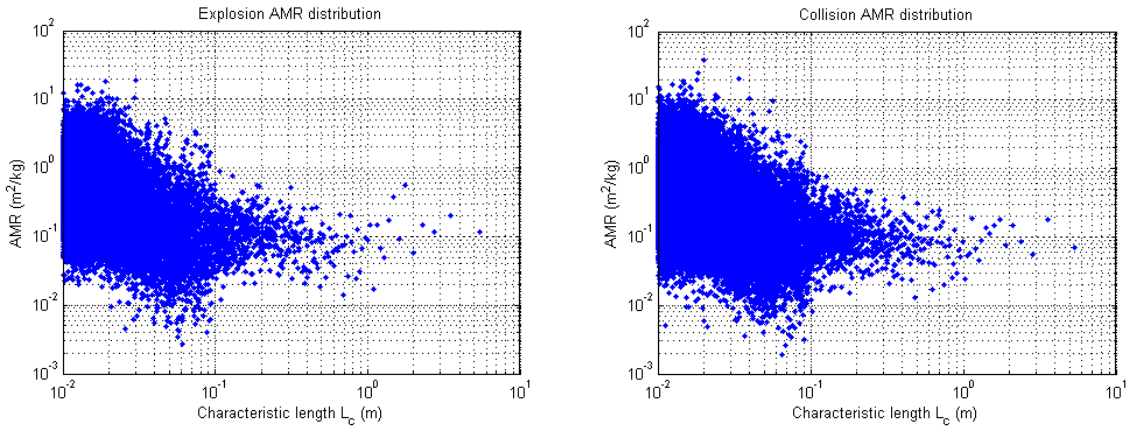


Figure 5.18: Fragment AMR distribution of simulated explosion with $S = 2.5$ and collision with $m_t = 1000$ kg.

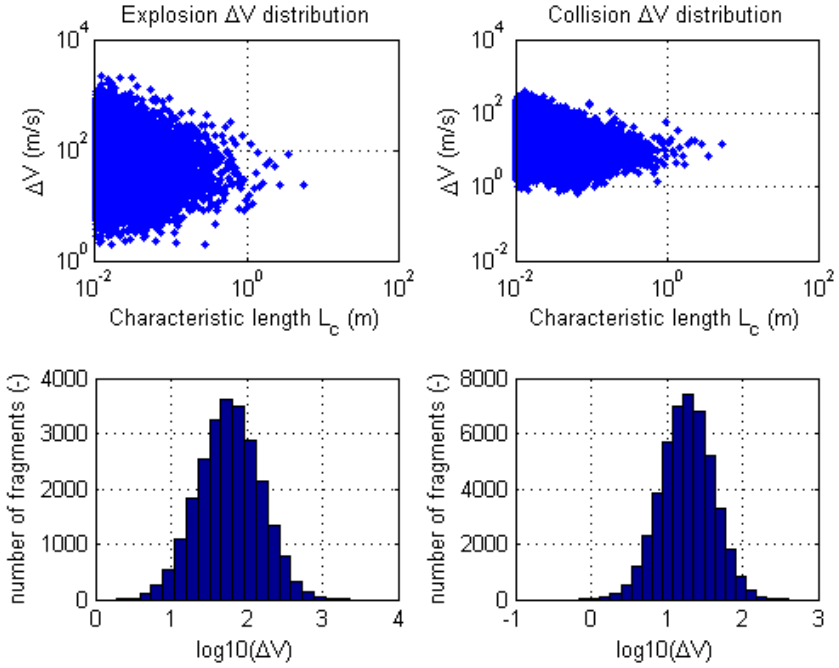


Figure 5.19: $\Delta V$ results of explosion with $S = 2.57$ and collision with $m_t = 1000$ kg.

plots for observed fragments from the Iridium 33 - Cosmos 2251 collision are also shown in Appendix A, where $\Delta V$ values of at most 600 m/s were found, which are closer to the simulations depicted in Fig. 5.20.

When the $\Delta V$ is added to the initial velocity, also a direction of the $\Delta V$ needs to be added. This in done in a random direction. The software includes a method to generate random unit vectors for this. To verify that the $\Delta V$ unit vectors are random with uniform distribution over a sphere, the $\Delta V$ vector results from the simulation were converted back to unit vectors and the x-, y- and z-components plotted against each other in 3 different plots as depicted in Fig. 5.22. Only fragments with $L_c \geq 3$ cm were included, since otherwise there would be too many fragments and the plots would just show completely filled blue spheres.

The collision plots are a bit denser than the explosion plots because the number of fragments is higher. By plotting the different components against each other, the vector components are seen from three different sides. From every side it looks similar. The points on the plot are denser towards the edges, which is expected since the vectors have a uniform distribution over a 3-dimensional sphere and it is projected on a

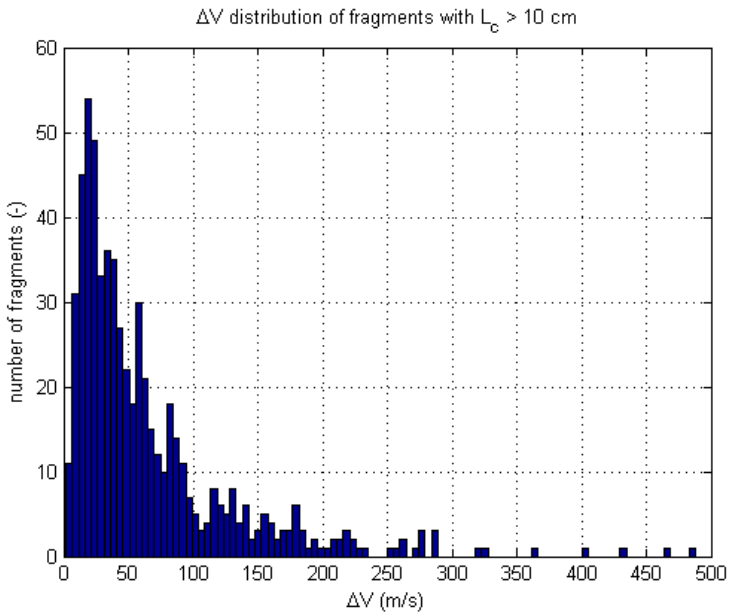


Figure 5.20: $\Delta V$ results of explosion with $S = 2.57$.

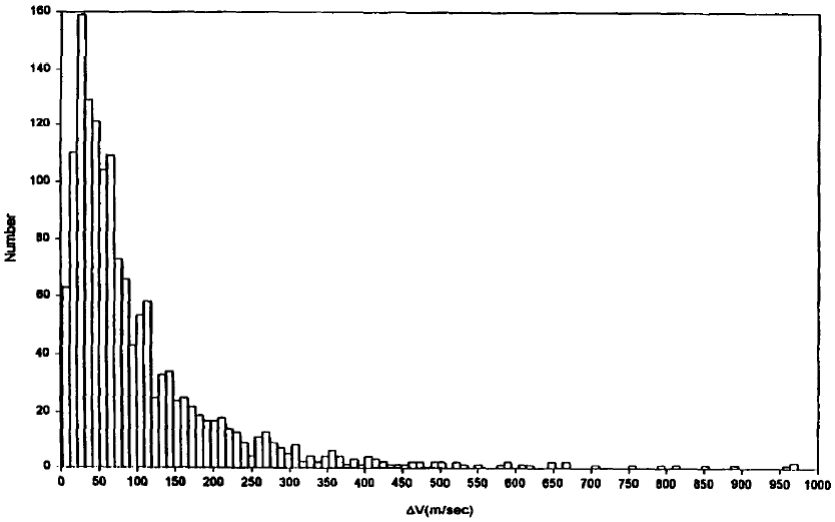


Figure 5.21: $\Delta V$ values computed for 1486 observed fragments from Delta, Ariane and Cosmos upper stages.

2-dimensional surface. In Matlab a 3-dimensional plot was also made, which can be rotated to view the results from any side, and the results always looked similar to the plots of Fig. 5.22.

One more plot was made with $\Delta V$ vectors of explosion fragments, shown in Fig. 5.23. Only fragments with $L_c \geqslant 20$ cm were included as otherwise the plot would be too cluttered. The random directions and different $\Delta V$ magnitudes are visible in this plot, which looks similar to how $\Delta V$s of the Iridium 33 - Cosmos 2251 are distributed in Fig. 4.8 (although there are obviously differences due to random effects).

### 5.3.4. FRAGMENTS PROPAGATION

The orbits of the fragments resulting from a fragmentation are propagated over a period of 100 years. Throughout the propagation GEO crossings are computed and added up. These can be used to compare the results of different fragmentation models and scenarios. Not all fragments are included in the orbit propagation. Fragments with characteristic length above 1 m are excluded because the fragmentation model is not accurate for these fragments. In Fig. 5.26 the total fragment mass is plotted against characteristic length. Several runs

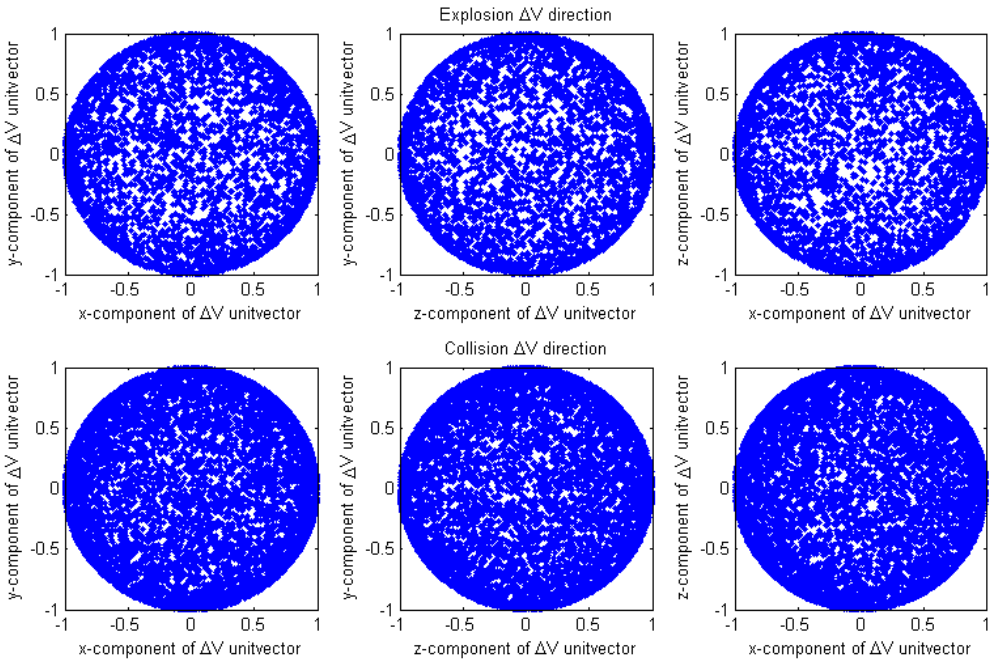


Figure 5.22: $\Delta V$ unit vector components of fragments with $L_c \geq 3$ cm from explosion simulation with $S = 2.57$ and collision simulation with $m_t = 1000$ kg.

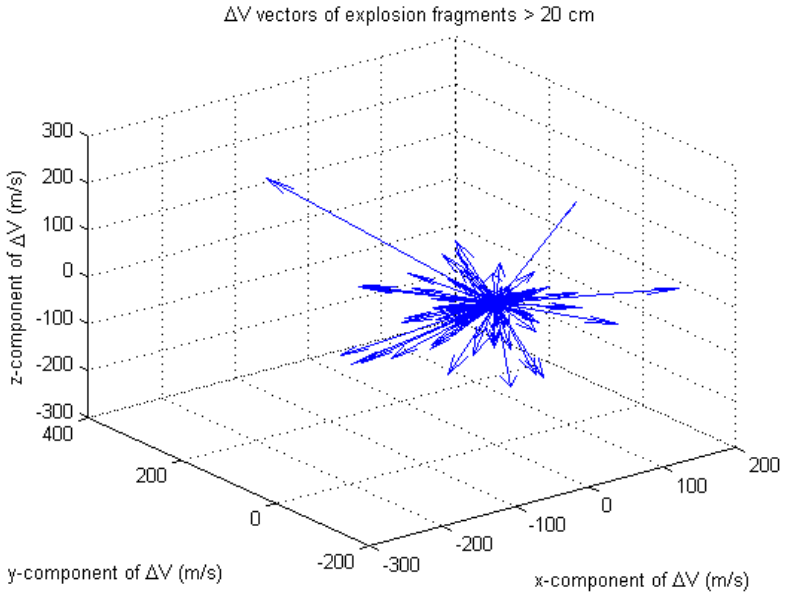


Figure 5.23: $\Delta V$ vectors of fragments with $L_c \geq 20$ cm from explosion simulation with $S = 2.57$.

were done with different RNG seeds, resulting in a different set of randomly created fragments. The resulting total mass should be close to each other for the different runs, however, the large fragments cause very large total mass differences between runs. The NASA breakup model actually also is only meant for fragments $\leq 35$ cm. However the model contains no separate distributions for the larger fragments, therefore the same distribution as for the fragments $\geq 11.2$ cm is used. Up to 1 m the results are still close to each other, therefore these are still included.

There is also a limit set for the smallest fragments that are included, because otherwise the number of frag-

ments would get too large resulting in extremely long computations. This limit is set at 1 cm. The fragment size distribution was shown already in Fig. 5.16. The number of fragments in a fragmentation of a 1000 kg satellite with $L_c \geqslant 1$ cm is 24439 for explosions and 46773 for catastrophic collisions. The number of fragments with $L_c \geqslant 1$ m is less than 20, so it is only a small part of the total that is excluded. The number of fragments increases exponentially with smaller $L_c$ limits. There are 598 (explosion) and 985 (collision) fragments with $L_c$ between 10 cm and 1 m. Since this is still a relatively small part of the total, all of these fragments are included. The larger fragments are also more dangerous, as they have higher masses, which is another reason to include all of them, to get the most accurate results. For the fragments between 1 cm and 10 cm only a fraction is included due to the large number of fragments. For explosions 1 in 20 fragments is included, and for collisions 1 in 30. This results in a total number between about 2000 and 3000 fragments. The computation of a fragment simulation and propagation of the resulting fragments takes between 90 and 120 minutes. In the computation of the total number of GEO crossings for all fragments, the number for small fragments is multiplied by 20 or 30 to compensate for the fact that only a part of the fragments is included. For other results plots are made separately for large and small fragments. For validation a test simulation was done of an explosion, with the settings described in Table 6.1 except for a different seed value of 3. The effect of using different seed values was also investigated in Section 5.4.3.

The $(\Omega, i)$ evolution of the debris cloud from an explosion of a 1000 kg satellite is shown in Figs. 5.24 and 5.25 for respectively the large and small fragments. The fragments follow a pattern similar to that of a GEO satellite, where the inclination increases up to about 15° and goes back to 0 in a period of about 53 years. The debris cloud does deviate from this pattern, because the initial orbits are slightly different and also the AMR of most fragments is larger than that of intact satellites, resulting in stronger SRP which makes them reach higher inclinations. With higher AMR values the period also becomes shorter than 53 years. In the plot it is visible that after 50 and 100 years the debris cloud is close to 0° inclination again. This pattern is visible in both the large and small fragments, although the small fragments are spread out more. This is both due to there being more of them in the plot and because they have larger differences in AMR value, due to the different mean and standard deviations in the fragmentation model; this is also visible in Fig. 5.18.

## 5.4. SOFTWARE TUNING

This section describes the methods used to optimize some of the model parameters that are included in the software.

### 5.4.1. SCALING FACTOR

While a scaling factor of 2.5 resulted in roughly 1000 kg mass for one simulation, there are still large mass variations between iterations with different RNG seeds. Mass results of 10 explosions and collisions with different seeds are shown in Fig. 5.26 The explosion masses are varying between roughly 800 and 1300 kg, while the collision masses are between 1000 and 1600 kg. The plots show that up to 1 m fragments, the differences between iterations are small, but they start to deviate more for larger fragments. In Fig. 5.16 one can see that the group of fragments > 1 m is very small, less than 20. However, these are the largest fragments, and when they get small AMR values their masses can become very high. The standard deviation is perhaps too large for these fragments, which is resulting in the large differences in total mass. The AMR model is also intended for fragments up to 35 cm. However there are no equations given for larger fragments, therefore the model was still used for these.

Since the differences between iterations turned out to be quite large, more simulations were done to find a good value for the scaling factor. An average total mass was computed based on 1000 iterations, for the scaling factors 2.0, 2.3, 2.4, 2.5, 2.6 and 2.7. The results are shown in Fig. 5.27. The plot looks linear for the range of scaling factors that is included. Through interpolation a scaling factor of 2.57 was found to obtain an average total mass of 1000 kg. This scaling factor is therefore used for further simulations.

### 5.4.2. GEO CROSSINGS METHOD

The GEO crossing computation uses the distance at which an orbit intersects the equatorial plane. However this is not necessarily the point in the orbit at which the distance to GEO is minimum. To test this, a minimum finding method is used, starting at the equatorial plane intersection, to find the true anomaly value where the orbit is closest to GEO. The method works as follows:

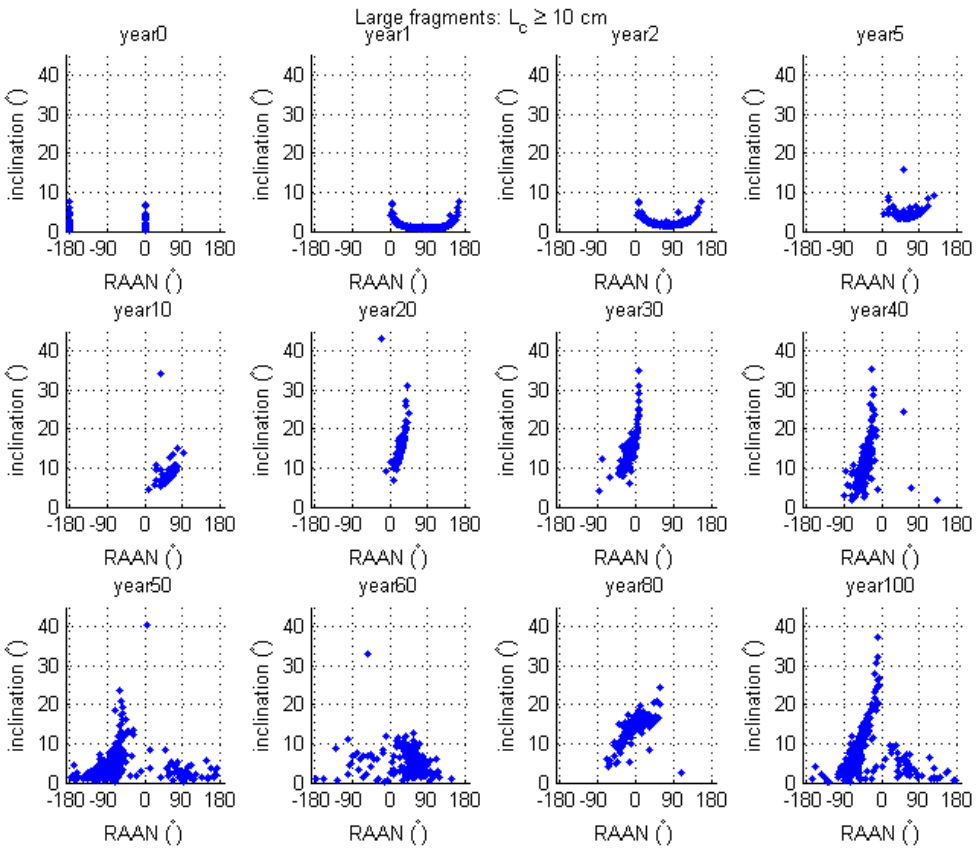


Figure 5.24: $i$-$\Omega$ evolution of fragments with $L_c \geq 10$ cm from explosion simulation with $S = 2.57$.

1. Set $\theta = -\omega$ for the first equatorial plane intersection and $\theta = 180 - \omega$ [°] for the second. Then perform the following steps for both intersections.
2. Set initial step-size to 10°.
3. Change $\theta$ by + or - the step-size, check if the distance to GEO becomes smaller. If it does, update $\theta$ to the value that results in the smaller distance. Repeat until a minimum is found.
4. Divide the step-size by 2 and repeat step 3, until the step-size becomes smaller than $10^{-4}$°.
5. Use the final $\theta$ value, at which the distance to GEO is minimum, to determine whether there is a crossing.

With both the simple equatorial plane intersection method and the minimum finding method, a single-object propagation and explosion simulation were done, to compare the number of GEO crossings that were found. For the explosion simulation the same settings were used as in Section 5.3.4. For the single object propagation the same initial orbit, year and duration were used, with the object characteristics $C_R = 1.3$, AMR = 1.0 m$^2$/kg and $m = 2.0$ kg. The results are shown in Table 5.5. For both the single object and explosion simulation a higher number of crossings was found with the minimum distance method, however the difference is only about 1%. The minimum distance method therefore gives a slightly more accurate result, while using a more complex computation method, resulting in slightly longer simulation times. Since the difference is very small, the intersection method is used as it is still very accurate for how simple it is.

### 5.4.3. RNG SEED

The fragmentation simulation program uses a random number generator to generate AMR values, $\Delta V$ magnitudes and $\Delta V$ directions for the fragments. It is possible to specify a seed number for the random number

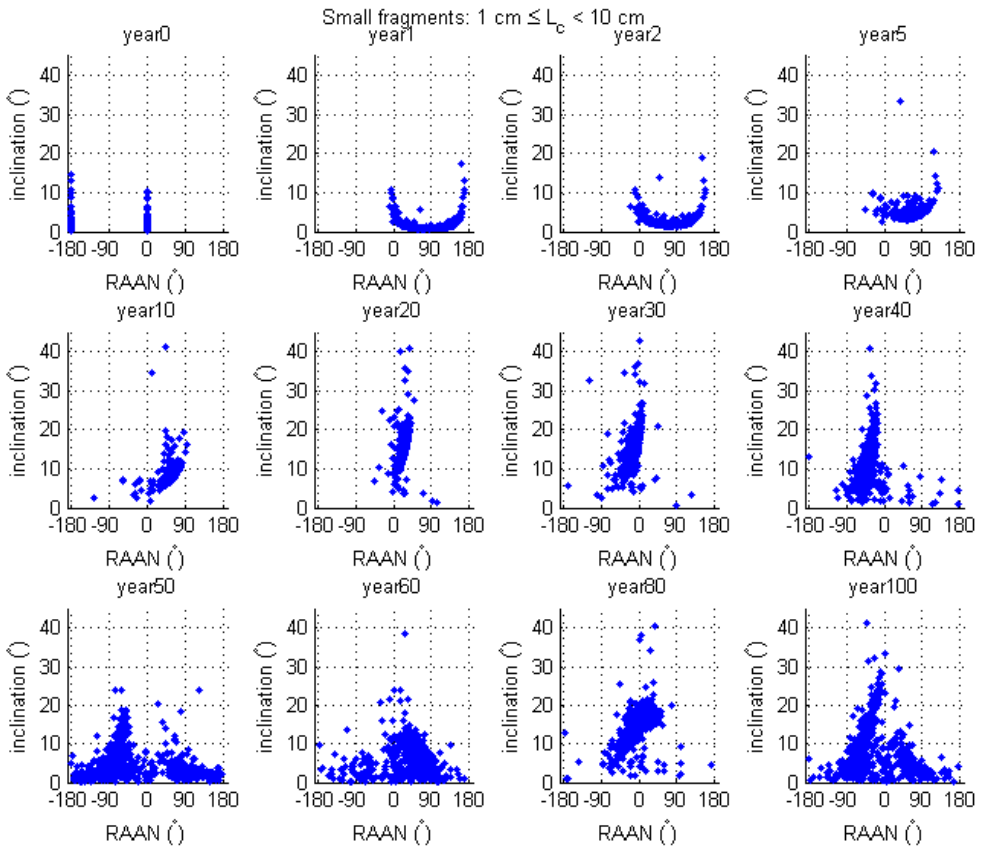


Figure 5.25: $i$-$\Omega$ evolution of fragments with $1 \leq L_c < 10$ cm from explosion simulation with $S = 2.57$.

Table 5.5: Number of GEO crossings found with different crossing computation methods.

| | Intersection Method | Minimum Distance Method | Difference [%] |
|---|---|---|---|
| single object | 3400 | 3438 | 1.1 |
| explosion | 63739022 | 64197729 | 0.72 |

generator. Using the same seed will result in the same sequence of pseudo-random numbers, and in this way the exact same results can be reproduced. If the results should be completely random, a different seed number should be used each time. With a different seed value, each fragmentation simulation will produce different fragments, which can be expected to result in different GEO crossings.

However, there is a large number of fragments, so even though individual fragments vary significantly, the total number of GEO crossings might not vary as much, since the differences average out over the large number of fragments. For the small fragments, only a part of the fragments is propagated and the crossings are multiplied to compensate for that. This will worsen the RNG effects, since if there are outliers they are also multiplied. On the other hand, the total number of small fragments that is included is still greater than the number of large fragments. To assess the consistency of the results, five explosion simulations were done with different seed values. It does not really matter which values are chosen, as long as they are five different ones. The same input settings are used as in Section 5.3.4.

For each simulation the total mass, number of GEO crossings and weighted GEO crossings were computed for the small and large fragments. Note that the total mass values are much smaller than 1000 kg, because only the propagated fragments are included in this mass computation. The fragments > 1 m, which have the highest masses, are excluded. These results are summarized in Table 5.6, along with the seed values that were

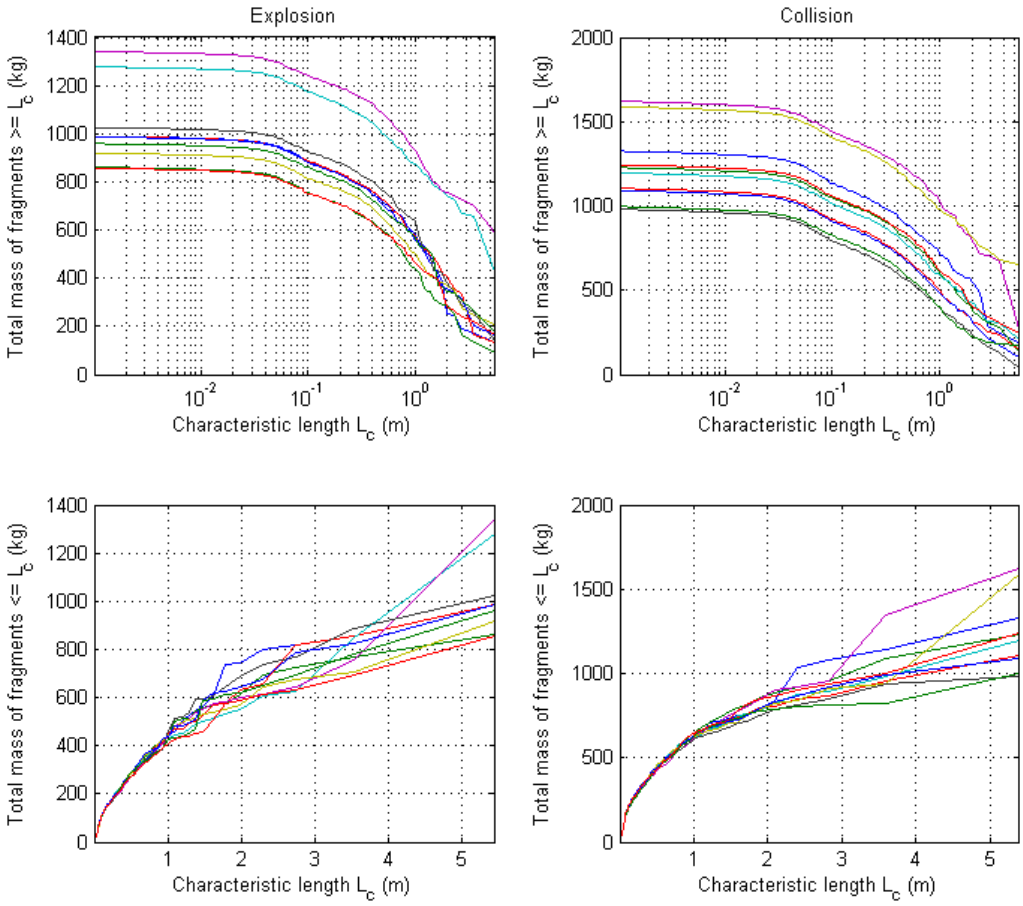


Figure 5.26: Total fragment mass of 10 simulated explosions with $S = 2.5$ and 10 collision with $m_t = 1000$ kg.

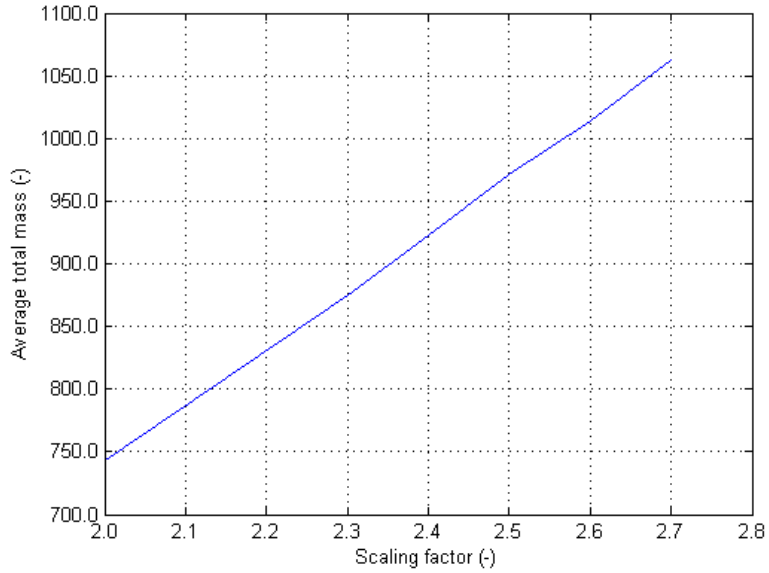


Figure 5.27: Average total fragment mass of 1000 explosion simulations, plotted versus the scaling factor.

used, so that the results can be reproduced. The bottom row shows the average of the five simulations' results. For each simulation the difference in % with respect to the average is also computed, which is shown in Table 5.7. In this table the minimum value in each column is emphasized through a grey background. The total mass values vary up to about 5%, with larger differences for the small fragments, up to 16%. For the total GEO crossings the differences are smaller, up to 2%, while there are greater differences for the large fragments. In the weighted GEO crossings the largest differences are found: up to 20% for the total, 21% for the large fragments, and 80% for the small fragments.

The weighted crossings are important for comparing the effectiveness of different graveyard orbits. The consistency of the small fragment results could be improved by including a larger number of fragments, however this will significantly increase computation time. It would also not improve the total of the weighted crossings very much, as Table 5.6 shows that the large fragments provide the greatest contribution to the weighted crossings. If completely random simulations were done each time, with different seeds, it may be difficult to determine if alternative disposal orbits are better or worse than the conventional one, because up to 20% differences can be caused by different seeds rather than different initial orbits. For this reason a single seed value will be used for each simulation, to produce the same fragments each time, so that only the effect of using different orbits can be separated and analysed.

The seed value which produced the results closest to average will be used. The results closest to average are not necessarily the best results, as it is not clear from the small number of simulations done whether results are most likely to be close to average. However, to get an accurate estimation of the distribution of the results many simulations would need to be done, which is too time-consuming as each simulation takes between 1.5 and 2 hours. Therefore it is assumed that results are more likely to be close to the average, and the seed which results in closest to average results is considered the best. Since the weighted crossings are most important and also the largest differences are found here, these are most important in selecting the seed value. The seed value of test B (5) is chosen, since both the total and large fragments difference are smallest here. The total mass difference is also the smallest and the total GEO crossings difference is only 0.5%.

Table 5.6: Mass and GEO crossings results of explosion simulations with different seeds values.

| | | Mass [kg] | | | GEO Crossings [-] | | | Weighted Crossings [-] | | |
|---|---|---|---|---|---|---|---|---|---|---|
| Test | Seed | Total | Large | Small | Total | Large | Small | Total | Large | Small |
| A | 3 | 404 | 311 | 93 | 6.4E+07 | 1.7E+06 | 6.2E+07 | 396 | 314 | 82 |
| B | 5 | 409 | 328 | 82 | 6.2E+07 | 1.6E+06 | 6.1E+07 | 436 | 380 | 56 |
| C | 42 | 388 | 295 | 93 | 6.2E+07 | 1.8E+06 | 6.0E+07 | 364 | 300 | 64 |
| D | 1337 | 404 | 310 | 94 | 6.3E+07 | 1.8E+06 | 6.1E+07 | 553 | 439 | 114 |
| E | 284 | 428 | 319 | 110 | 6.3E+07 | 1.7E+06 | 6.1E+07 | 550 | 372 | 178 |
| Average | | 407 | 313 | 94 | 6.3E+07 | 1.7E+06 | 6.1E+07 | 460 | 361 | 99 |

Table 5.7: Mass and GEO crossings differences compared to average of explosion simulations with different seeds values.

| | | Mass [%] | | | GEO Crossings [%] | | | Weighted Crossings [%] | | |
|---|---|---|---|---|---|---|---|---|---|---|
| Test | Seed | Total | Large | Small | Total | Large | Small | Total | Large | Small |
| A | 3 | -0.7 | **-0.4** | -1.4 | 1.7 | -3.1 | 1.8 | -13.9 | -13.0 | -17.36 |
| B | 5 | **0.6** | 4.8 | -13.5 | -0.5 | -3.7 | -0.4 | **-5.1** | **5.3** | -42.97 |
| C | 42 | -4.6 | -5.6 | -1.2 | -1.3 | 3.6 | -1.4 | -20.9 | -16.9 | -35.43 |
| D | 1337 | -0.7 | -0.8 | **-0.2** | **-0.2** | 5.1 | **-0.4** | 20.3 | 21.6 | **15.58** |
| E | 284 | 5.3 | 2.0 | 16.3 | 0.3 | **-2.0** | 0.4 | 19.5 | 3.0 | 80.17 |

A similar analysis is done for the collision simulations. The input settings of Table 7.1 are used with 5 different seed values. The results are summarized in Tables 5.8 and 5.9. The differences in mass and GEO crossings are similar to those found from the explosion simulations. However the differences in weighted crossings are much smaller, up to about 9% rather than 20%. This is probably because the $\Delta V$s are much smaller, which causes the fragments' orbits to deviate less from the initial orbit of the satellite. The differences between individual fragments are then also smaller and random differences between runs will have a smaller effect. There are also simply more fragments, even though only 1 in 30 of the small fragments is included.

Since all simulations have small differences in mass and GEO crossings compared to the average, the weighted crossings are again used to choose the seed value that is used for later simulations. The seed value of test C (132) is chosen, since the differences in total weighted crossings and small fragment weighted crossings are minimum and the difference in the large fragment weighted crossings is the second smallest.

Table 5.8: Mass and GEO crossings results of collision simulations with different seeds values.

| | | Mass [kg] | | | GEO Crossings [-] | | | Weighted Crossings [-] | | |
|---|---|---|---|---|---|---|---|---|---|---|
| Test | Seed | Total | Large | Small | Total | Large | Small | Total | Large | Small |
| A | 149 | 610 | 428 | 182 | 1.7E+08 | 2.5E+06 | 1.7E+08 | 550 | 370 | 180 |
| B | 79 | 625 | 464 | 160 | 1.6E+08 | 3.2E+06 | 1.6E+08 | 580 | 412 | 168 |
| C | 132 | 587 | 430 | 157 | 1.7E+08 | 3.0E+06 | 1.7E+08 | 531 | 369 | 163 |
| D | 2 | 621 | 470 | 151 | 1.6E+08 | 2.6E+06 | 1.6E+08 | 517 | 392 | 126 |
| E | 14 | 642 | 466 | 176 | 1.7E+08 | 3.0E+06 | 1.7E+08 | 482 | 328 | 154 |
| Average | | 617 | 452 | 165 | 1.7E+08 | 2.9E+06 | 1.6E+08 | 532 | 374 | 158 |

Table 5.9: Mass and GEO crossings differences compared to average of collision simulations with different seeds values.

| | | Mass [%] | | | GEO Crossings [%] | | | Weighted Crossings [%] | | |
|---|---|---|---|---|---|---|---|---|---|---|
| Test | Seed | Total | Large | Small | Total | Large | Small | Total | Large | Small |
| A | 149 | -1.1 | -5.3 | 10.3 | 1.5 | -11.7 | 1.7 | 3.4 | **-1.1** | 13.9 |
| B | 79 | 1.2 | **2.8** | **-3.0** | -3.4 | 12.2 | -3.7 | 8.9 | 10.1 | 6.3 |
| C | 132 | -4.9 | -4.8 | -5.2 | 2.2 | **4.1** | 2.2 | **-0.1** | -1.4 | **2.9** |
| D | 2 | **0.7** | 4.1 | -8.6 | -1.5 | -9.2 | -1.4 | -2.8 | 4.7 | -20.6 |
| E | 14 | 4.1 | 3.2 | 6.5 | **1.2** | 4.6 | **1.2** | -9.4 | -12.3 | -2.5 |

# 6

# EXPLOSION RESULTS

This chapter discusses the results of various explosion simulations. The first section describes the standard test case, where an explosion is simulated in a conventional disposal orbit and the results are described thoroughly. The standard test case is used as reference for the other simulations, where changes to the input settings are made and the results are compared to the standard test case. The simulations are divided in sensitivity analysis and alternative graveyard orbits. In the sensitivity analysis small changes are made to the input settings, to assess how sensitive the results are to specific parameters. With the alternative graveyard orbit results, changes are made to the initial orbit of the intact spacecraft before the explosion, to investigate whether different orbits are better for keeping explosion fragments away from GEO. At the end of the chapter the most important results are summarized.

## 6.1. STANDARD TEST CASE

The standard test case uses the input settings described in Table 6.1. The initial orbit is 300 km above GEO, which is roughly the conventional graveyard orbit. A seed value of 5 is used, as discussed in Section 5.4. The lower limit of $L_c$ is set to 1 cm. This is done because the number of fragments increases exponentially with smaller $L_c$, therefore a limit has to be set somewhere to limit the computation time required. Also small fragments are less dangerous, as a collision of a small fragment with a satellite creates less debris. The upper limit of $L_c$ is set to 1 m, since above this value the total fragment mass results are very inconsistent. The small fragment $L_c$ value defines a limit above which every fragment is included (as long as it is still below the upper limit) and below which only a fraction of the fragments is included, as the number of fragments is still very high. The small fragment factor is set to 20 and the small fragment $L_c$ to 10 cm, which means that below 10 cm only 1 in 20 fragments is included in the fragment propagation part of the simulation. To compensate for this in the results, when total GEO crossings are computed the crossings by small fragments are multiplied by the small fragment factor (20). Some results are also shown separately for small and large fragments.

The scaling factor is set to 2.57, which results in an average total mass of 1000 kg. The target mass is then also set to 1000 kg and in this way the crossing computation checks if the explosion fragments could cause catastrophic collisions with a satellite of similar mass. The start date and duration are limited by the SPICE ephemerides provided with Tudat. The ephemerides only work with years between 1900 and 2050. A longer duration would also increase computation time, by almost the same ratio as the duration increase, as the orbit propagation is the most time consuming part of the simulation. With the current settings, the simulations take between 1.5 and 2 hours. It is important that the interval is long enough to include long-term periodic behaviour in the orbit evolution of the fragments. For a GEO satellite, the $i$-$\Omega$ evolution has a period of 53 years, which means almost 2 periods are included in the simulation. For fragments with higher AMR the period is shorter, which results in them going through closer to 2 or even slightly above 2 periods. All of the possible perturbations forces are enabled.

Various plots are made from the explosion results. The $i$-$\Omega$ evolution of the fragments is shown in Figs. 6.1 and 6.2 for respectively the large and small fragments. These plots look very similar to Figs. 5.24 and 5.25 since only the seed number is different. As discussed previously, the fragments follow a pattern similar to that of

Table 6.1: Settings for standard explosion test case

| **Initial orbit of intact spacecraft** | |
|---|---|
| $a$ [km] | 42464 (300 km above GEO) |
| $e$ [-] | 0.0 |
| $i$ [°] | 0.0 |
| $\omega$ [°] | 0.0 |
| $\Omega$ [°] | 0.0 |
| $\theta$ [°] | 0.0 |
| **RNG** | |
| Seed | 5 |
| **Fragmentation simulation** | |
| $L_c$ lower limit [m] | 0.01 |
| $L_c$ small fragment [m] | 0.1 |
| $L_c$ upper limit [m] | 1.0 |
| $S$ [-] | 2.57 |
| Small fragment factor [-] | 20 |
| **Propagator** | |
| $C_R$ [-] | 1.3 |
| Target mass [kg] | 1000 |
| Crossing distance [km] | 50 |
| Start date | January 1, 1900, 00:00 |
| Duration [yr] | 100 |
| **Perturbations** | |
| $J_2$ | true |
| $3^{rd}$ body Sun | true |
| $3^{rd}$ body Moon | true |
| SRP | true |

a GEO satellite, of which an example is shown in Fig. 6.3. The fragments deviate a bit from the pattern of a satellite, since the initial orbits are different due to the ΔV from the explosion, and also higher AMR values result in higher inclinations and shorter periods.

For each fragment the total number of GEO crossings is computed throughout the orbit propagation. To see if there is a relationship between fragment characteristics and number of GEO crossings, the crossings are plotted versus the fragments' $L_c$ and AMR in Fig. 6.4. For the $L_c$ plots, it seems as $L_c$ becomes smaller, the spread in GEO crossings becomes larger and the maximum increases. This is also the case for the small fragments AMR plot. Additionally, there is a larger concentration of fragments along the x-axis (i.e. with 0 crossings) with AMR < 0.4 $m^2$/kg. Low AMR values are probably required for 0 crossings, because then eccentricity changes due to perturbations are smaller. If eccentricity changes are small, then depending on the initial orbit of a fragment (which is determined by the ΔV) it is possible that the orbits never have a perigee within 50 km of GEO altitude, which means there are no crossings. The fragments with the highest crossings are also with very low AMR values. These might have different initial orbits, which together with small eccentricity changes results in many crossings.

A histogram plot of the GEO crossings was also made. It is shown in Fig. 6.5 for the large fragments and in Fig. 6.6 for the small fragments. In this plots it is very clear that there is a large number of fragments with close to 0 crossings, which does not follow the trend of the distribution of the other fragments. A possible reason for this happening is that the fragments need to develop a certain minimum eccentricity to be able to come close to GEO, and a large number of fragments has a combination of low AMR and ΔV that results in them not reaching this eccentricity.

To gain more insight into the behaviour of the fragments with zero crossings, two of them were randomly selected and their orbit evolution was simulated with the single-object propagator, since the explosion simulation only saves results every year. The characteristics of the selected fragments are described in Table 6.2.

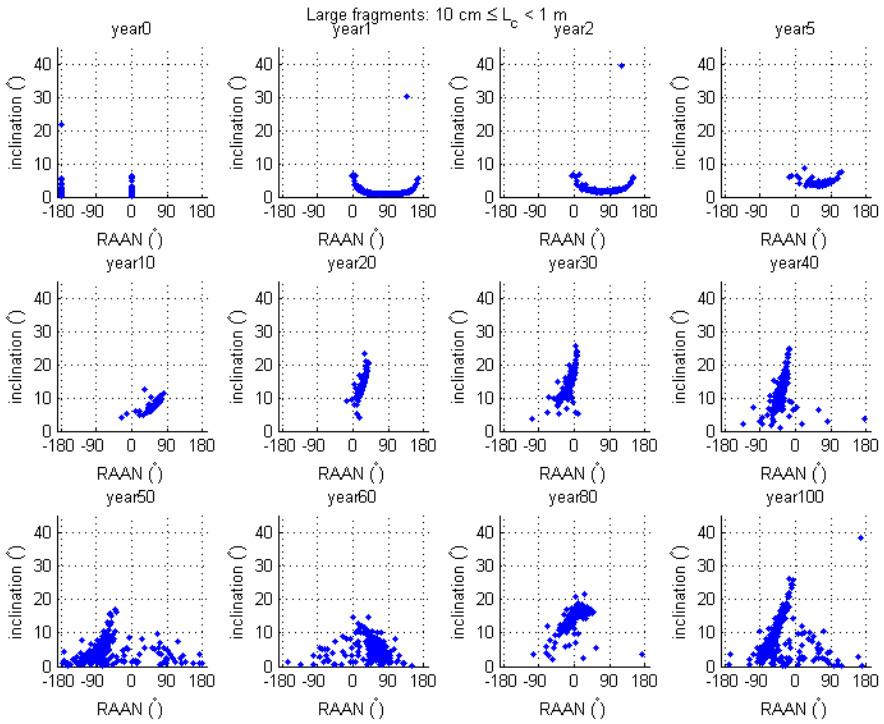


Figure 6.1: $i$-$\Omega$ evolution of large fragments from standard explosion test case.

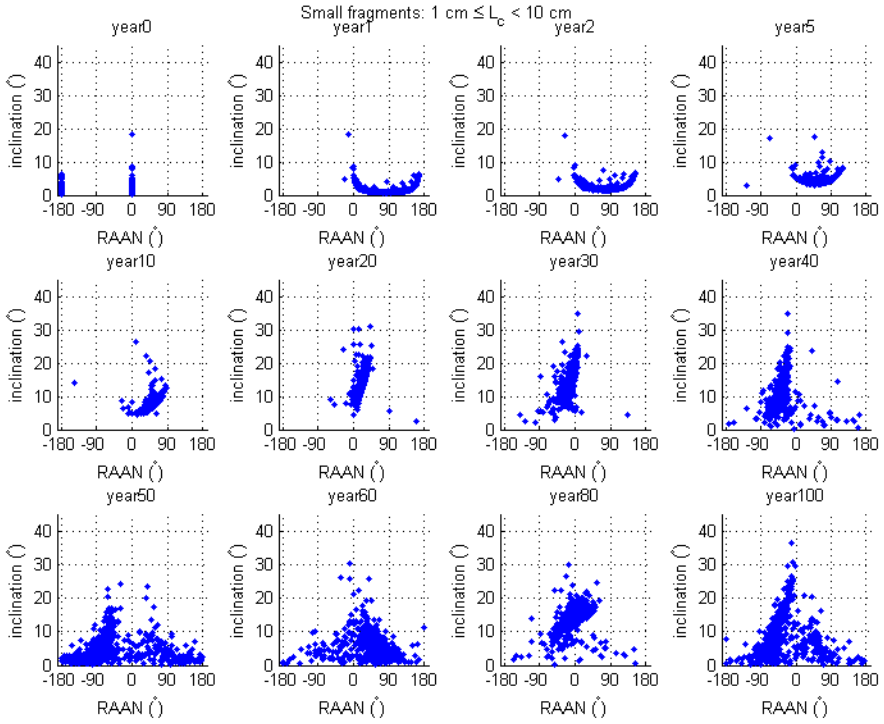


Figure 6.2: $i$-$\Omega$ evolution of small fragments from standard explosion test case.

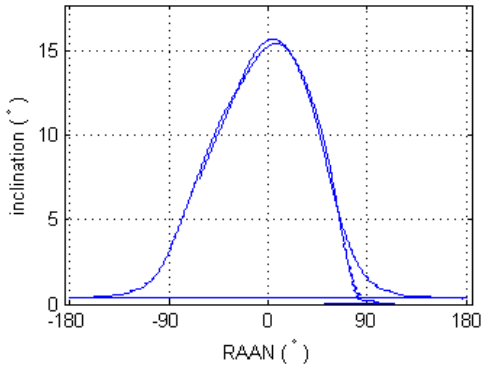


Figure 6.3: $i$-$\Omega$ evolution of a satellite with the same initial orbit, propagator and perturbations settings as the standard test case and an AMR of 0.02 $m^2$/kg.

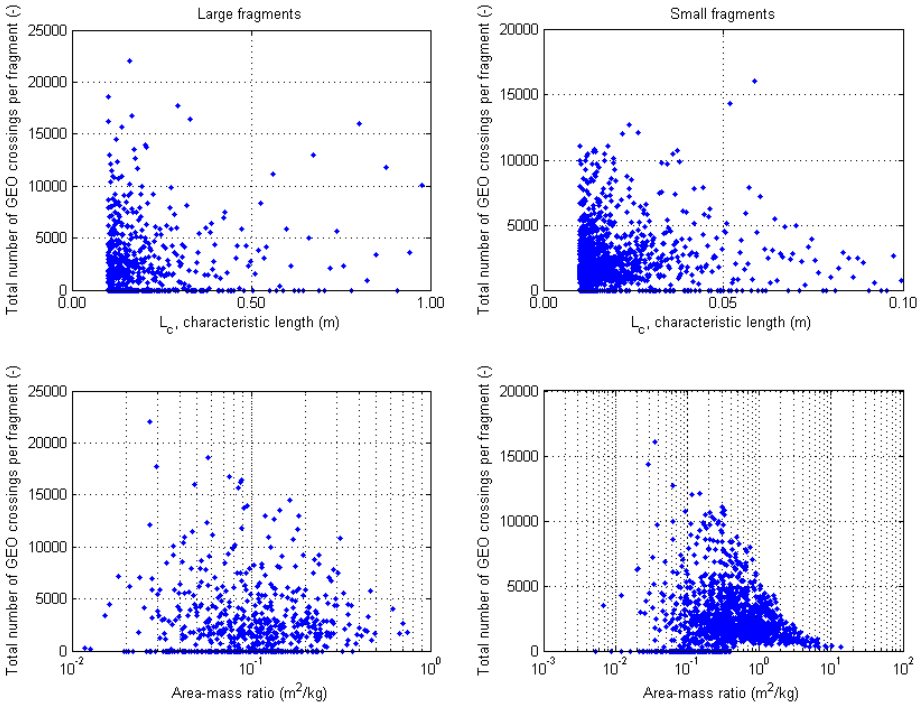


Figure 6.4: Crossings of individual fragments plotted versus $L_c$ and AMR, standard explosion test case.

The perigee evolution of the fragments is plotted in Fig. 6.7. The perigee altitude is shown relative to the GEO altitude. Since the perigee altitude never reaches below the defined 50 km limit, there are no crossings. Both fragments have a very small initial eccentricity, and also a low AMR, which means eccentricity changes due to SRP are small. The orbits then remain close to circular, and since the initial orbit is already 300 km above GEO, this results in there being no crossings.

From the analysis of the zero-crossing fragments, it seems that these fragments may also typically have a small initial eccentricity. The eccentricities of the fragments are plotted against the GEO crossings in Fig. 6.8. For both the large and small fragments the same pattern is seen. The fragments with very high eccentricities have low numbers of crossings, while the fragments with large numbers of crossings all have very low, although non-zero, eccentricities. Additionally there is a concentration of fragments in the bottom left corner of the plot, where fragments have zero of near-zero crossings and low eccentricities. It was investigated whether the AMR has an influence on whether the fragments have high eccentricities or high crossings (see Appendix E), but this turned out to not be very relevant for this test case.

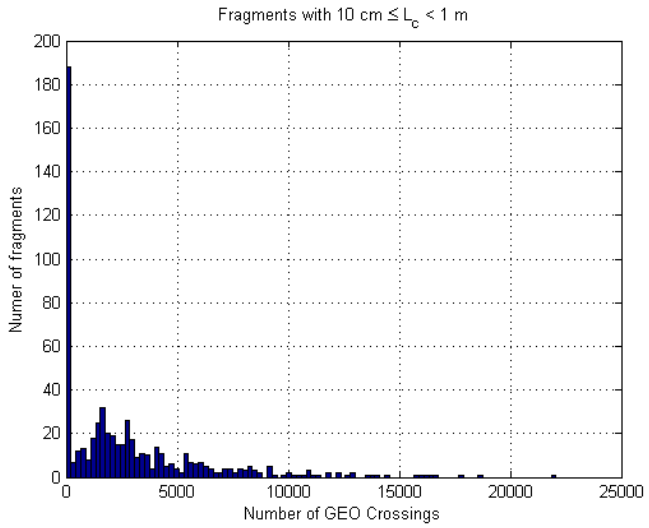


Figure 6.5: Histogram plot of GEO crossings of fragments with 10cm ⩽ $L_c$ < 1m from standard explosion test case.

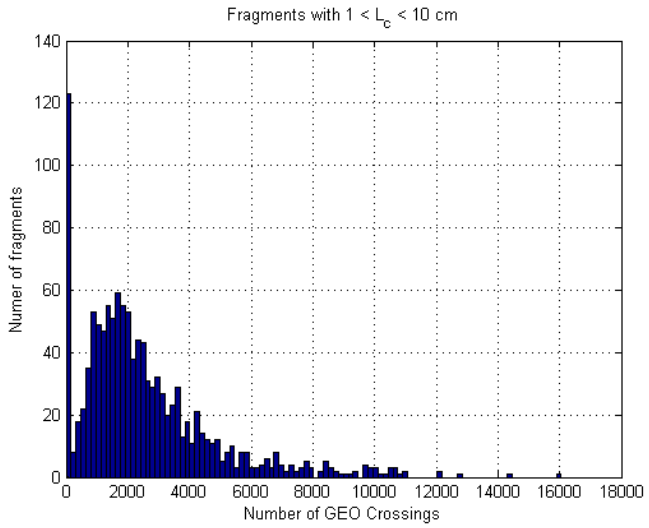


Figure 6.6: Histogram plot of GEO crossings of fragments with 1cm ⩽ $L_c$ < 10cm from standard explosion test case.

Table 6.2: Characteristics of two fragments from the standard explosion test case with 0 GEO crossings.

| Parameter | Fragment 1 | Fragment 2 |
|---|---|---|
| AMR [$m^2$/kg] | 0.159414498222891 | 0.115642559476712 |
| $m$ [kg] | 0.165357301785097 | 0.001066306940333 |
| $a$ [km] | 42418.70320059010 | 42522.00698778040 |
| $e$ [-] | 0.001965291473343 | 0.001384723742096 |
| $i$ [°] | 0.016371156919371 | 1.992977569256520 |
| $\omega$ [°] | 56.881704163350598 | 169.3549426971860 |
| $\Omega$ [°] | 180.0 | 180.0 |
| $\theta$ [°] | 123.1182958366490 | 10.645057302813900 |

From Fig. 6.8 three fragments were selected for further analysis, to better understand why it is that the high eccentricity fragments have few crossings while fragments with many crossings always have low eccentricity. One fragment with high eccentricity was selected from the upper left part of the plot, another with a high number of crossings from the lower right and also one from the lower left corner with low eccentricity and zero crossings. The characteristics of the selected fragments are shown in Table 6.3.

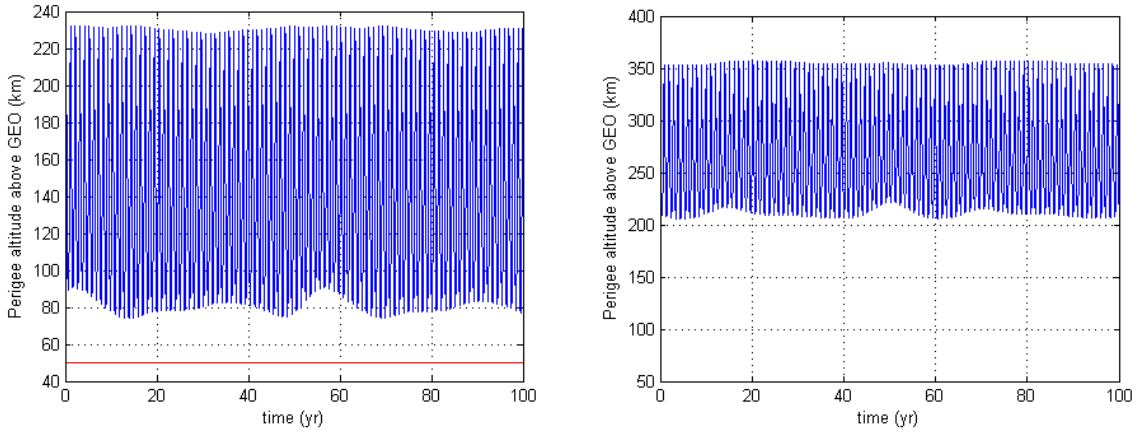


Figure 6.7: Perigee altitude evolution of fragment 1 (left) and fragment 2 (right) from Table 6.2. Both are fragments with zero crossings from the standard explosion test case.

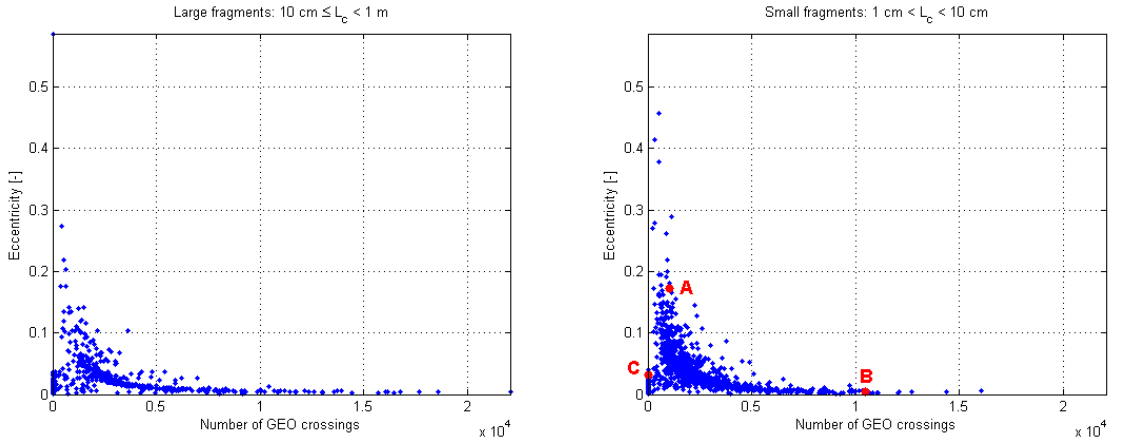


Figure 6.8: Eccentricity and GEO Crossings of large (left) and small (right) fragments from the standard test case. The red dots specify three fragments which are further analysed. Their properties are described in Table 6.3

.

Table 6.3: Characteristics of three fragments selected from the eccentricity-crossings plot (Fig 6.8) of the standard explosion test case.

| Parameter | Fragment A | Fragment B | Fragment C |
|---|---|---|---|
| AMR [$m^2$/kg] | 2.199791099642610 | 0.180415791182255 | 0.049981583110835 |
| $m$ [kg] | 0.000040568954728 | 0.004013110972845 | 0.001389777666516 |
| $a$ [km] | 36163.42273014950 | 42259.83664401780 | 43702.22484498730 |
| $e$ | 0.192292811940236 | 0.004848651204668 | 0.028385628521605 |
| $i$ [°] | 1.597860085902320 | 0.002903429107371 | 0.722620119876287 |
| $\omega$ [°] | 200.7099629456290 | 355.6225266458680 | 183.6874576494280 |
| $\Omega$ [°] | 0.0 | 180.0 | 180.0 |
| $\theta$ [°] | 159.2900370543710 | 184.3774733541320 | 356.3125423505720 |

For each of these fragments a separate propagation was done with the single-object propagator, since this saves data at each time-step rather than only once per year like the explosion simulation does. The fragment characteristics are given with many significant digits, since they are used as input in the single-object propagator and the results should be as close as possible to those from the explosion simulation.

Plots of the orbital elements and perigee/apogee evolution for each fragment are included in Appendix D. In this section only the most important results are shown. The behaviour of fragment C is similar to that of the two previously discussed fragments with zero crossings. Eccentricity changes are small due to low AMR, and

the perigee altitude is always above the 50 km limit, which means there are no crossings possible.

Both fragment A and B sometimes have periods with and without crossings. This is clearly visible in the inclination plots, however the periods without crossings do not seem related to specific inclination values. For example for fragment B, when the inclination increases during the first 25 years, there are no crossings between 7 and 11° inclination, but when the inclination later reaches this range again, there are crossings.

It seems that the crossings are actually related to the argument of periapsis evolution, which is shown for fragments A and B in Fig. 6.9. Red dots indicate points with crossings. For both fragments $\omega$ passes 360° and then repeats a similar pattern several times. The crossings are always in the same $\omega$ ranges, although these are different between the two fragments. For fragment A the ranges of $\omega$ where there are crossings are much smaller than for fragment B, which is likely the reason there are less crossings. Fragment B has a very low eccentricity throughout the propagation, varying between 0.0036 and 0.0095. The orbit of fragment B is always much closer to circular than fragment A, which has an eccentricity varying between 0.16 and 0.23. If an orbit is circular, then $\omega$ has no effect at all. If it is close to circular, then probably the effect of $\omega$ on GEO crossings is small, and it increases with increasing eccentricity. Then if eccentricity increases, there are fewer $\omega$ values were crossings are possible and the number of crossings reduced, which is why fragment A has fewer crossings than fragment B.

Not only are the ranges of $\omega$ values where crossings are possible different in size, they are also centred around different values. For fragment A the crossings are around 0° and 180°, while for fragments B there are no crossings around these values. This can be explained by looking at the apogee and perigee altitude plots. For fragment A the apogee is close to GEO and the perigee far below GEO. This means that for crossings to be possible, the apogee must be close to the equatorial plane. This is the case then $\omega$ is close to 0° or 180°. For fragment B the perigee is slightly lower than 50 km below GEO, while the apogee is more than 200 km above GEO. This means that when the apogee and perigee are on the equatorial plane, there are no crossings.

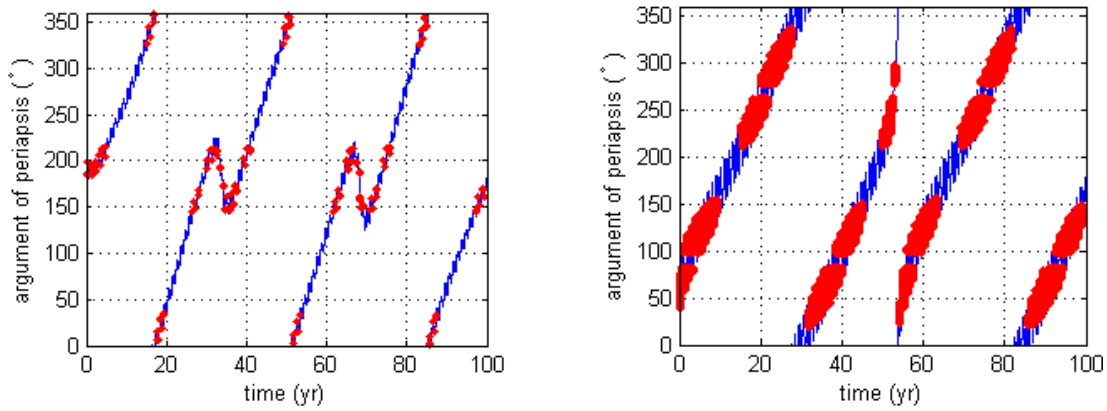


Figure 6.9: Argument of periapsis evolution of fragment A (left) and fragment B (right) from standard explosion test case. The red dots indicate data points where there were crossings. The properties of the fragments are described in Table 6.3.

Lastly the total number of GEO crossings and weighted GEO crossings for all fragments combined is plotted versus time in Fig. 6.10. The number of crossings by small fragments is multiplied by the Small Fragment Factor to compensate for the fragments that have been excluded from the propagation. The small fragments cause by far the largest number of GEO crossings, which is expected since there are many more of them. There are 23826 small fragments as opposed to 598 large fragments. However, for the weighted crossings the large fragments contribute most to the total. This is because the mass affects the weighted crossing value and the large fragments have much higher masses than the small fragments.

Between 40 and 60 years the weighted crossings curve flattens out. There are still just as many crossings happening during this time, as is visible in the total crossings plot, but the weights of these crossings are extremely small because the inclinations are very close to 0° at this time (see Figs. 6.1 and 6.2). The weighted crossing value is always much lower than the number of crossings. While the maximum weight of a crossing

is 1, in the case of a catastrophic collision, this never happens because the masses of the fragments combined with the crossing velocities in GEO are too small. From the low weighted crossings it can be concluded that if the fragments would collide with GEO satellites, only a very small number of new fragments would be created. However this does not necessarily mean the fragments are not dangerous. They might still be able to critically damage satellites if they impact important components.

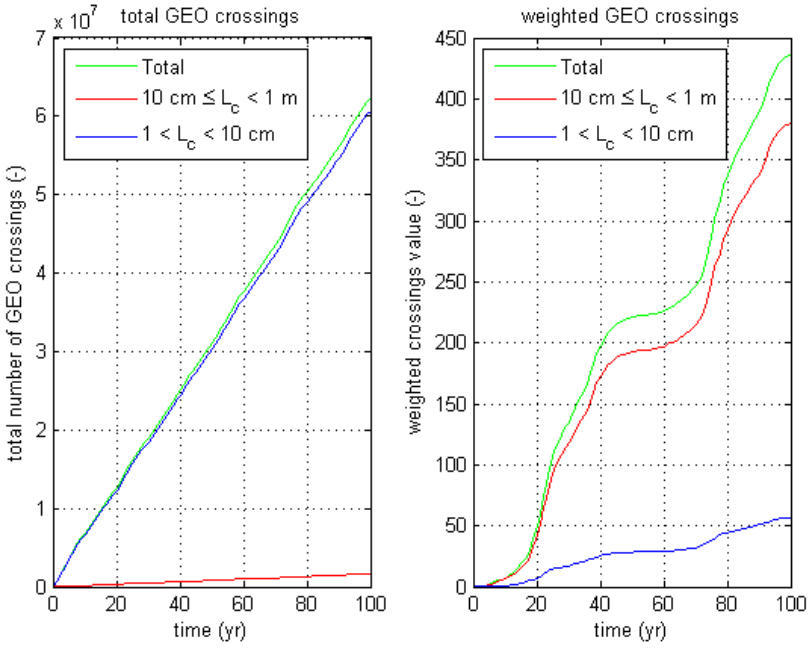


Figure 6.10: Total number of GEO crossings plotted versus time for standard explosion test case.

## 6.2. SENSITIVITY ANALYSIS

In this section the sensitivity analysis tests are described. The results of each test are described in this section, and the GEO crossings as well as the weighted crossings of all tests are shown in Table. 6.4. There is a total value (referring to the total of large and small fragments) and also the contribution of the large and small fragments to the total as a percentage. Additionally the fragments that have zero GEO crossings are shown, as a percentage of the total number of fragments for large and small fragments separately. The differences of the simulations with respect to the standard test case are shown in Table 6.5. Each of the simulations is discussed in this section.

### 6.2.1. DIFFERENT POINT IN $i$-$\Omega$ EVOLUTION: $i = 15°$

While a satellite is disposed in the graveyard orbit at (close to) 0° inclination, this changes over time due to perturbations. Since it is not predictable when an explosion could occur, it could happen at any point throughout the orbit evolution. The inclination can reach up to 15°, which is the value taken for this test, as it is the maximum. Generally if the inclination is changed, the RAAN must also be set in agreement with the typical $i$-$\Omega$ evolution. When the inclination is 15°, RAAN is back to 0°, as is visible in Fig. 6.3, therefore it does not need to be changed from the standard test case for this simulation.

Since the fragments start at a different point in the $i$-$\Omega$ evolution, the $i$-$\Omega$ plots (shown in Fig. 6.11) for the same years as the standard test case look different. However the behaviour is still the same. The fragments now pass their minimum inclination between 20 and 30 years, and again at around 80 years. In Table 6.5 the total number of GEO crossings is slightly smaller (1.7%) than for the standard test case. This is possibly caused by there being more fragments with 0 crossings. This could be a random effect. The randomized $\Delta V$ vectors are still in the same direction, however the initial velocity is slightly different due to the inclination, therefore the $\Delta V$s cause different changes in the initial orbits of the fragments.

Table 6.4: GEO crossings results of sensitivity analysis for explosions. The crossings and weighted crossings percentages of the small and large fragments are percentages of the total values, while the 0-crossing fragment percentages are of the total number of fragments.

| | GEO crossings | | | Weighted crossings | | | 0-crossing fragments | |
|---|---|---|---|---|---|---|---|---|
| **Test setup** | **Total** [-] | **Large** [%] | **Small** [%] | **Total** [-] | **Large** [%] | **Small** [%] | **Large** [%] | **Small** [%] |
| **Standard test case** | 6.24E+7 | 2.6 | 97.4 | 436 | 87.1 | 12.9 | 28.9 | 9.7 |
| $i = 15°$ | 6.13E+7 | 2.5 | 97.5 | 356 | 82.1 | 17.9 | 34.4 | 12.8 |
| $i = 15°, \theta = 180°$ | 7.02E7 | 2.4 | 97.7 | 339 | 60.2 | 39.8 | 33.4 | 9.3 |
| $0.5\Delta V$ | 7.70E+7 | 2.4 | 97.6 | 418 | 83.3 | 16.7 | 42.6 | 15.3 |
| $1.5\Delta V$ | 5.83E+7 | 2.9 | 97.1 | 380 | 85.0 | 15.0 | 20.4 | 7.1 |
| **Crossing distance 25 km** | 3.11E+7 | 2.6 | 97.4 | 220 | 87.2 | 12.8 | 31.6 | 11.0 |
| **Crossing distance 100 km** | 1.26E+8 | 2.7 | 97.3 | 903 | 87.0 | 13.0 | 21.9 | 6.6 |
| **Reflectivity 1.2** | 6.27E7 | 2.6 | 97.4 | 435 | 87.1 | 12.9 | 30.3 | 10.4 |
| **Reflectivity 1.4** | 6.21E7 | 2.7 | 97.3 | 439 | 87.2 | 12.9 | 27.8 | 8.8 |
| **Start date +0.25 years** | 4.88E7 | 3.2 | 96.8 | 408 | 86.3 | 13.7 | 34.1 | 20.1 |
| **Start date +6 years** | 6.25E7 | 2.6 | 97.4 | 461 | 87.2 | 12.8 | 28.8 | 9.6 |
| **Satellite mass 3000 kg** | 1.70E8 | 2.7 | 97.3 | 355 | 78.0 | 22.0 | 28.2 | 8.3 |

Table 6.5: GEO crossings results of sensitivity analysis for explosions, percentage difference w.r.t. standard test case. For the crossings and weighted crossings, the difference of the small fragments are w.r.t. the actual number of crossings by these fragments, not the percentage of Table 6.4.

| | GEO crossings [%] | | | Weighted crossings [%] | | | 0-crossing fragments [%] | |
|---|---|---|---|---|---|---|---|---|
| **Test setup** | **Total** | **Large** | **Small** | **Total** | **Large** | **Small** | **Large** | **Small** |
| $i = 15°$ | -1.7 | -6.3 | -1.6 | -18.5 | -23.2 | 13.1 | 19.1 | 32.1 |
| $i = 15°, \theta = 180°$ | 12.5 | 0.5 | 12.8 | -22.4 | -46.4 | 139.4 | 15.8 | -3.5 |
| $0.5\Delta V$ | 23.5 | 13.5 | 23.8 | -4.3 | -8.5 | 24.1 | 47.4 | 58.2 |
| $1.5\Delta V$ | -13.7 | -6.0 | -13.9 | -13.0 | -15.1 | 0.96 | -29.3 | -26.1 |
| **Crossing distance 25 km** | -50.2 | -50.6 | -50.2 | -49.7 | -49.6 | -50.0 | 9.3 | 13.9 |
| **Crossing distance 50 km** | 102 | 108 | 102 | 107 | 107 | 108 | -24.3 | -31.4 |
| **Reflectivity 1.2** | 0.5 | -0.6 | 0.5 | -0.4 | -0.4 | -0.4 | 4.6 | 7.8 |
| **Reflectivity 1.4** | -0.5 | 0.7 | -0.5 | 0.5 | 0.6 | 0.1 | -4.0 | -8.7 |
| **Start date +0.25 years** | -21.7 | -6.2 | -22.1 | -6.6 | -7.4 | -1.0 | 17.9 | 107.8 |
| **Start date +6 years** | 0.3 | 0.2 | 0.3 | 5.7 | 5.8 | 5.2 | -0.6 | -0.9 |
| **Satellite mass 3000 kg** | 172 | 178 | 172 | -18.6 | -27.1 | 38.5 | -2.7 | -14.4 |

The weighted crossings are also lower than the standard test case, by 18%. While part of this may also be due to the random $\Delta V$s, part of it is also caused by the different $i$-$\Omega$ evolution, in combination with the 100-year propagation period. Fragments with small AMR have a period close to 53 years, which means that in 100 years there will not be 2 full cycles completed. In the standard test case, the minimum inclination parts (where weighted crossings are low) are then around 0, 53 and 106 years. In Fig. 6.10, if one looks at the red curve on the right, if starts to flatten, but it does not fully. In Fig. 6.12, the minimum inclination parts are around 25 and 80 years, so they are both fully included, resulting in a lower value of the weighted crossings. Additionally, the maximum inclination of the fragments is a bit lower (about 22°) than the standard test case (about 26°). Perhaps inclination changes when starting at $i = 0°$ result in larger inclination differences over time. This can also cause differences in weighted crossings, as lower inclinations result in lower crossing velocities.

### 6.2.2. $i = 15°, \theta = 180°$

For this simulation one fragment with a very high $\Delta V$ ended up in a hyperbolic orbit and was therefore removed from the propagation. This did not occur for the simulation with only $i = 15°$, however initial velocity is now in the opposite direction due to the true anomaly of 180°. This again changes the effects of the $\Delta V$s. While the total weighted crossings value is not very different from that of the $i = 15°$ test case (-22.4 and -18.5% compared to the standard test case, see Table 6.5), there is a large difference in the weighted crossings

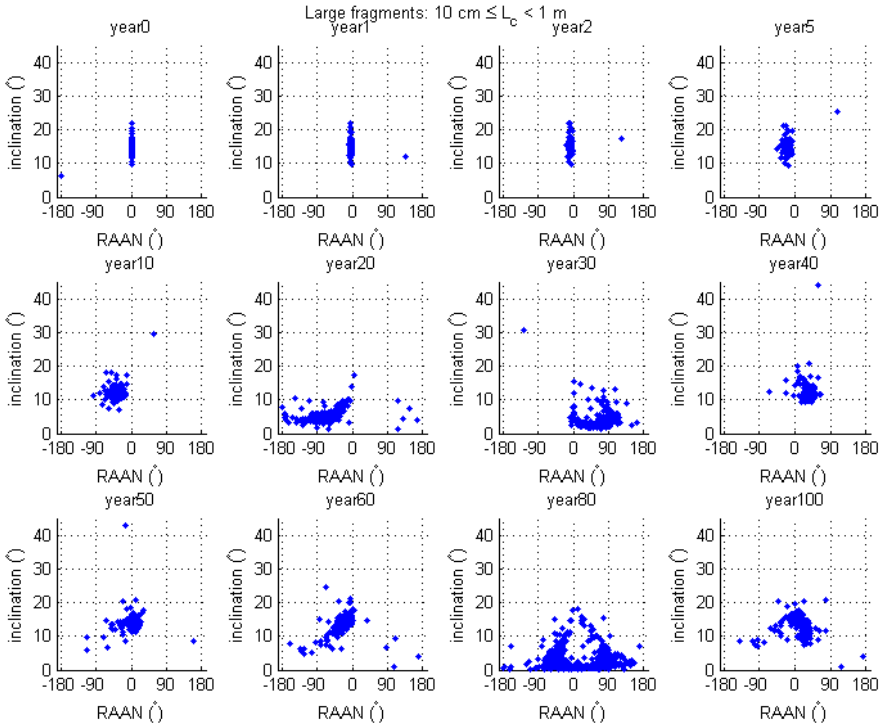


Figure 6.11: $i$-$\Omega$ evolution of large fragments from standard explosion test case.

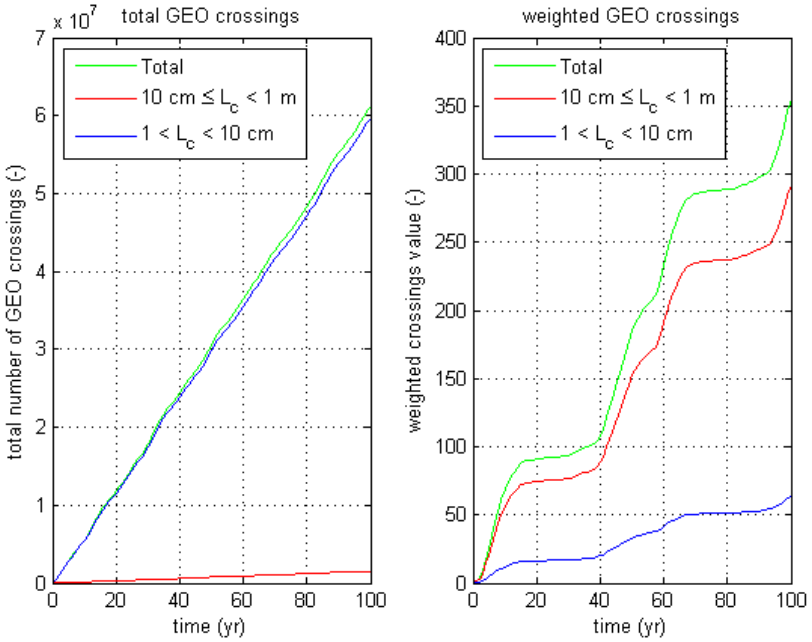


Figure 6.12: Total number of GEO crossings versus time for standard explosion test case.

by large and small fragments separately. The weighted crossings by large fragments are -46.4% and by small fragments +140% compared to the standard test case. Of course when only changing the inclination the initial velocity vector is only changed by 15°. Adding the true anomaly change, the direction of the vector is inverted and the difference is much larger, perhaps similar to using a different seed value. Tables 5.6 and 5.7

show the results of these tests, where differences of up to 80% in weighted crossings by small fragments were found, when compared to the average of the five different seed number. However if one compares the results from test C and E individually, the difference is almost 300%. It is therefore definitely possible that the results from this test case are caused by the different initial velocity which changes the effects of the random $\Delta V$s. It is difficult to see how much changing the orbit parameters affected the results, as the random differences due to $\Delta V$ might be much larger.

### 6.2.3. LOWER $\Delta V$: $0.5\Delta V$

The explosion model does not take into account anything like explosion energy. All explosions are considered equal. In reality perhaps weaker or stronger explosions may result in different $\Delta V$ magnitudes, therefore a simulation is done where all $\Delta V$s are multiplied by 0.5. The results are interesting as the number of GEO crossings increases, even though the number of 0-fragment crossings also increases. Additionally the weighted crossings slightly decrease. It can be expected that the number of 0-crossing fragments increases, because due to the smaller $\Delta V$s the initial orbits are closer to circular, which means perigees are higher. 0-crossing fragments have a combination of low AMR and high initial perigee. Therefore if fragments have higher perigees on average, it is expected that there are more 0-crossing fragments.

The fact that there are more crossings in total, means perhaps there are also more fragments with a very large number of crossings, which also typically have low eccentricities. Note that for all simulations the total number of crossings consists mainly of crossings by small fragments (97.6% in this case), therefore the change in total crossings is mainly due to changes in crossings by small fragments. Even though the number of small 0-crossing fragments increases by 58%, these are still only 15% of the total small fragments. This change therefore does not influence the total crossings by a large amount. The histogram plot of the small fragment crossings is shown in Fig. 6.13. While it does look like there might be more fragments with large numbers of crossings compared to the standard test case, it is not very clear from the plot.

To verify whether the increase in crossings is due to an increase in fragments with large number of crossings, the total number of crossings by small fragments with at least 5000 crossings is computed. For the $0.5\Delta V$ test case, this number of crossings is 1.61E07 larger than for the standard test case, which is is enough to cause the difference in total GEO crossings. Despite the higher number of crossings, the weighted crossings are actually slightly lower, by 4.3%. This is most likely caused by smaller initial inclinations due to the lower $\Delta V$, which results in lower maximum inclinations and lower crossing velocities. Lower eccentricities also result in lower crossing velocities.

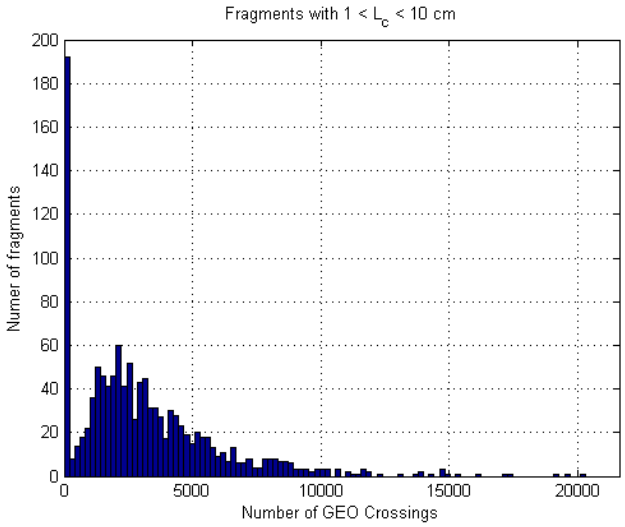


Figure 6.13: Histogram plot of GEO crossings of fragments with 1cm $\leq L_c <$ 10cm from $0.5\Delta V$ test case.

### 6.2.4. HIGHER $\Delta V$: $1.5\Delta V$

At first there were some problems running the program with increased $\Delta V$ values. There were errors during the orbit propagation which caused the program to stop. This turned out to be due to a single fragment with a hyperbolic initial orbit after applying the $\Delta V$. With the standard test case this fragment did not get a large enough $\Delta V$ for the orbit to become hyperbolic. The orbit dynamics model is only applicable to elliptical orbits, which is why the hyperbolic orbit caused problems. The program was modified to exclude fragments with hyperbolic orbits from the orbit propagation, which results in no crossings being computed for this fragment. However, that is not a problem, because a fragment with hyperbolic orbit would leave the Earth and not make any GEO crossings anyway.

The number of crossings and also the number of fragments with zero crossings decreased, which is the opposite of the results with $0.5\Delta V$, as one might expect. Fig. 6.8 showed that both fragments with zero and with many crossings typically have low eccentricities. There are less of both of these fragments in this test case because the higher $\Delta V$s cause higher eccentricities. The weighted crossings value also decreased, even though this also happened in the $0.5\Delta V$ test case. It is not clear why exactly this happens.

### 6.2.5. CROSSING DISTANCE 25 KM

When halving the crossing distance, the GEO crossings and weighted crossings are also halved as expected. This is the same for small and large fragments. This suggests that the distance of the <50 km crossings might be uniformly distributed. This cannot be verified with the current software, since the data of the individual crossings is not saved. The number of 0-crossing fragments is slightly increased, which is expected, since the crossing definition is more restrictive.

### 6.2.6. CROSSING DISTANCE 100 KM

When the crossing distance is doubled, the number of crossings increases by 102%. This behaviour is similar to the 25 km case in that the number of crossings changes by the same factor as the crossing distance. The number of 0-crossing fragments now decreases.

### 6.2.7. REFLECTIVITY 1.2

By setting the reflectivity to 1.2 it is decreased by 7.7% with respect to the reflectivity of the standard case. Changing reflectivity does not affect the initial orbits of the fragments, like changing the $\Delta V$ or inclination does, however it does change how the orbits evolve over time. A smaller reflectivity is similar to a smaller AMR. The effect of SRP is reduced and therefore the eccentricity changes due to SRP become smaller. From the results in Tables 6.4 and 6.5 it appears that this only has a small effect on the number of crossings. The values for regular and weighted crossings change by at most 0.6%. The number of fragments with 0 crossings increases slightly, by 4.6% for large and 7.8% for small fragments. It is expected that it increases, since smaller eccentricity changes mean there will be more fragments with small eccentricity, which is necessary for a fragment to have 0 crossings.

### 6.2.8. REFLECTIVITY 1.4

The results from increasing the reflectivity are very similar to when reducing it. The differences are at most 0.7%, and there are positive differences where they were negative for 1.2 reflectivity and vice versa. The number of 0-crossing fragments is now smaller than for the standard test case, since the eccentricity changes due to SRP are larger.

### 6.2.9. START DATE +0.25 YEARS

Changing the start date by 0.25 years results in the Earth being at a different point in its orbit. Since the orbit is slightly elliptical, the distance to the Sun will be different and the SRP perturbations might be different due to this. The Moon position will be different as well, which affects the third-body perturbations by the Moon's gravity.

The total number of crossings for this simulation was 22% lower than for the standard test case. This difference is of the same order of magnitude as that for the $0.5\Delta V$ simulation. The weighted crossings are also lower, although only by 6.6%. There are also many more fragments with zero crossings; 18% more for the large fragments and 108% for the small fragments. The 108% more small fragments is the greatest difference of all sensitivity analysis simulations.

For the standard test case, plots were made of the perigee altitude evolution of two fragments (shown in Fig. 6.7). For the 2nd fragment, another simulation was done with the +0.25 years start date. The two plots are shown in Fig. 6.14, they are zoomed in on the first 10 years so that the curves can be seen clearly. Both start at the same perigee altitude, but the evolution is very different. For the standard test case, the altitude first starts to decrease, there are sharp peaks in the plots, the total amplitude is larger (about 70 km) and the minimum lower (about 210 km). For the test case with the different start date the perigee altitude first starts to increase and the amplitude is only about 30 km, while the minimum at 255 km. This is probably caused by the differences in SRP perturbations, as that causes eccentricity evolution and therefore perigee altitude evolution. Only one fragment is investigated here, which does not prove that similar differences are the case for all fragments, however if this would the case that would explain why the number of GEO crossings is reduced.

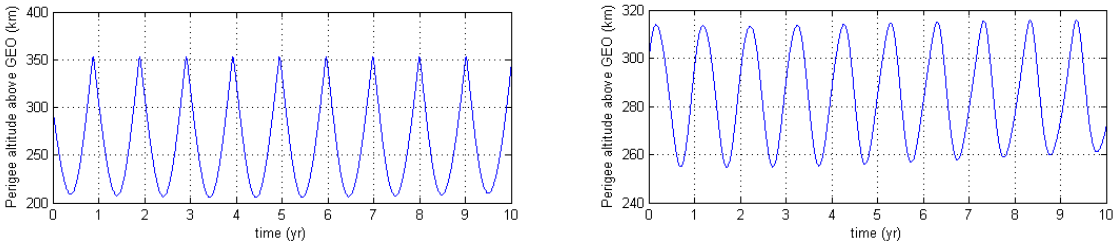


(a) Standard test case

(b) Start date +0.25 yr

Figure 6.14: Perigee altitude evolution of fragment 2 from Table 6.2, with standard test case settings and with later start date.

### 6.2.10. START DATE +6 YEARS

When the date is changed by an integer number of years, Earth will be at the same point in its orbit again, therefore the SRP will not be very different from the standard test case, as opposed to the simulation with +0.25 years. However, the Moon's orbit will be different, as it has a period in its ascending node evolution of 18.61 years. The number of GEO crossings of this simulation varies very little from the standard test case, only 0.3%, the smallest of all sensitivity analysis simulations. However the weighted crossings are 5.7% higher, which is about the same magnitude as the simulation with start date +0.25 years. The difference might be caused by differences in inclination evolution due to third-body gravitational perturbations by the Moon, since the Moon's orbit is different from the standard test case.

### 6.2.11. SATELLITE MASS 3000 KG

To change the mass of the exploding satellite the scaling factor needs to be changed. Fig. 5.27 shows the relationship of total mass to the scaling factor. This plot only includes masses from about 750 to 1050 kg, however the plot looks close to linear for this range. Assuming that the total mass is a linear function of the scaling factor, the results were extrapolated to find a scaling factor of 6.94 for a total mass of 3000 kg. The simulation with this scaling factor resulted in a total mass of the simulated fragments of 3195 kg, which is close enough, because the point of this test is to investigate the effect of increasing the mass and it does not need to be exactly 3000 kg. The target mass that is used in weighted crossing computations is also set to 3000 kg.

Increasing the satellite mass automatically results in more GEO crossings, since there are simply more fragments created in the explosion. In the standard test case 598 large and 23826 small fragments are generated. With the scaling factor set to 6.94 this is increased to 1616 (+174%) large fragments and 64337 (+170%) small fragments. The increase in fragments is close to the GEO crossings increment of 172%.

The weighted crossings are expected not to deviate much from the standard test case, since the the weighted crossings are divided by the total satellite mass, which is also set to 3000 kg. If weighted crossings were based on a 1000 kg mass like in the standard test case, they would be expected to increase by the same factor as the number of crossings (i.e. about 170%). Since the mass is 3 times as high, weighted crossings are reduced by a factor 3, which would result in a difference of about -10% with respect to the standard test case. The actual difference is -18.6% which is larger than one might expect, however this could be caused by random effects.

Due to the larger number of fragments there are more random numbers being created, which is similar to using a different RNG seed.

## 6.3. ALTERNATIVE GRAVEYARD ORBITS

In this section the effect of using different graveyard orbits is investigated. The initial orbit is changed from the standard test case, by using a different altitude and/or different inclination. In the sensitivity analysis there were also some simulations with different initial orbits, however these were orbits that are possible due to orbit evolution of a satellite starting in a conventional graveyard orbit. The simulations are discussed in a similar way to the sensitivity analysis, with the results summarized in Tables 6.6 and 6.7.

Additionally Table 6.8 shows the $\Delta V$ required for a Hohmann transfer to these alternative orbits. For the inclined orbits the plane-change $\Delta V$ is computed after the altitude increase, as it requires a slightly lower $\Delta V$ at higher altitudes. The table shows the $\Delta V$ required, the percentage difference in $\Delta V$ of the alternative graveyard orbits compared to the standard test case, as well as the station-keeping time that could be performed with the same amount of $\Delta V$. Typical values for GEO station-keeping $\Delta V$s are 50-55 m/s per year (Zandbergen, 2015). For the station-keeping time in the table 52.5 m/s per year is assumed.

Table 6.6: GEO crossings results of explosion simulations in alternative graveyard orbits. The crossings and weighted crossings percentages of the small and large fragments are percentages of the total values, while the 0-crossing fragment percentages are of the total number of fragments.

| | **GEO crossings** | | | **Weighted crossings** | | | **0-crossing fragments** | |
|---|---|---|---|---|---|---|---|---|
| **Test setup** | **Total** [-] | **Large** [%] | **Small** [%] | **Total** [-] | **Large** [%] | **Small** [%] | **Large** [%] | **Small** [%] |
| **Standard case** | 6.24E+7 | 2.6 | 97.4 | 436 | 87.1 | 12.9 | 28.9 | 9.7 |
| **500 km above GEO** | 4.49E+7 | 2.6 | 97.4 | 273 | 86.4 | 13.6 | 44.3 | 21.8 |
| **1000 km above GEO** | 2.41E+7 | 1.9 | 98.1 | 141 | 80.4 | 19.7 | 65.6 | 43.4 |
| **2000 km above GEO** | 1.07E+7 | 2.1 | 97.9 | 44 | 76.7 | 23.3 | 78.9 | 65.1 |
| $i = 7.4^\circ$ | 6.06E+7 | 2.7 | 97.3 | 230 | 84.5 | 15.5 | 39.0 | 15.8 |
| $i = 7.4^\circ$, **1000 km** | 2.40E+7 | 2.0 | 98.0 | 55 | 79.7 | 20.3 | 67.2 | 46.6 |

Table 6.7: GEO crossings results of explosion simulations in alternative graveyard orbit, percentage difference w.r.t. standard test case. Differences in crossings are differences between the absolute values of the crossings, while the difference in 0-crossing fragments is the difference in the percentage of 0-crossing fragments.

| | **GEO crossings** [%] | | | **Weighted crossings** [%] | | | **0-crossing fragments** [%] | |
|---|---|---|---|---|---|---|---|---|
| **Test setup** | **Total** | **Large** | **Small** | **Total** | **Large** | **Small** | **Large** | **Small** |
| **500 km above GEO** | -28.0 | -28.6 | -28.0 | -37.6 | -38.1 | -34.2 | 53.2 | 126.0 |
| **1000 km above GEO** | -61.4 | -72.1 | -61.1 | -67.7 | -70.2 | -50.8 | 126.6 | 349.4 |
| **2000 km above GEO** | -82.8 | -86.0 | -82.7 | -89.8 | -91.1 | -81.7 | 172.8 | 573.6 |
| $i = 7.4^\circ$ | -2.8 | -1.8 | -2.8 | -47.3 | -48.9 | -36.6 | 34.7 | 63.5 |
| $i = 7.4^\circ$, **1000 km** | -61.5 | -70.2 | -61.3 | -87.3 | -88.4 | -80.0 | 132.4 | 382.4 |

Table 6.8: $\Delta V$ required to transfer to alternative graveyard orbits. The $\Delta V$ difference is relative to the standard test case, which is 300 km above GEO. The station-keeping column describes the station-keeping time that could be performed with an equal amount of $\Delta V$.

| **Test setup** | $\Delta V$ **[m/s]** | **Difference** [%] | **Station-keeping** |
|---|---|---|---|
| **Standard case** | 8.8 | 0 | 2.0 months |
| **500 km above GEO** | 14.6 | 66 | 3.3 months |
| **1000 km above GEO** | 29.1 | 230 | 6.6 months |
| **2000 km above GEO** | 57.3 | 550 | 13.1 months |
| $i = 7.4^\circ$ | 404 | 4486 | 7.7 years |
| $i = 7.4^\circ$, **1000 km** | 421 | 4680 | 8.0 years |

### 6.3.1. DIFFERENT ALTITUDE

Three explosions were simulated with initial orbits at altitudes higher than the standard case. As expected, both the number of crossings and the weighted crossings are reduced, with larger reductions for higher altitudes. Also the number of fragments with zero crossings increases. Both these changes are expected, because with a higher graveyard orbit the fragments' orbits need to reach higher eccentricities for crossings to be possible. Of the large fragments, a larger percentage has zero crossings than of small fragments. This is probably because the small fragments can have higher AMR values, which causes them to develop larger eccentricities due to SRP, therefore they are more likely to reach the minimum eccentricity required for crossings.

The eccentricity-crossings plots, shown in Fig. 6.15 for the case where the altitude is 2000 km above GEO, look different from the standard test case plots in Fig. 6.8. The minimum eccentricity for fragments that have non-zero crossings is visibly higher and the maximum number of crossings is only about 7400, while for the standard case it is about 22000. These differences seem related to each other. In the standard test case the fragments with the highest numbers of crossings had very low eccentricities. With a higher altitude graveyard orbit, the minimum eccentricity for a fragment to have crossings increases, which results in the fragments that in the standard case had many crossings now having zero crossings, since their eccentricity is too low. The small fragments with non-zero crossings in Fig. 6.15 can have lower initial eccentricities than the large fragments, since they can have higher AMRs and therefore larger eccentricity changes due to SRP.

The largest reduction in GEO crossings is found when the altitude is 2000 km above GEO. Crossings are reduced by 83% and weighted crossings by an even larger 90%. However this does come at the cost of a $\Delta V$ that is 6.5 times as high as for the standard case, which is equal to a year of station-keeping and therefore reduced operational mission time. Further altitude increases could reduce the crossings even more, although there might be some limit at which increases become less beneficial relative to the increasing costs.

With the altitude 500 km above GEO crossings are reduced by 28% and weighted crossings by 38%, for a 66% increase in $\Delta V$ cost or 1.3 months of station-keeping. In the case where the altitude is 1000 km above GEO crossings are reduced by 61% and weighted crossings by 68%. $\Delta$ is increased by 230% which is equal to an additional 4.6 months of station-keeping.

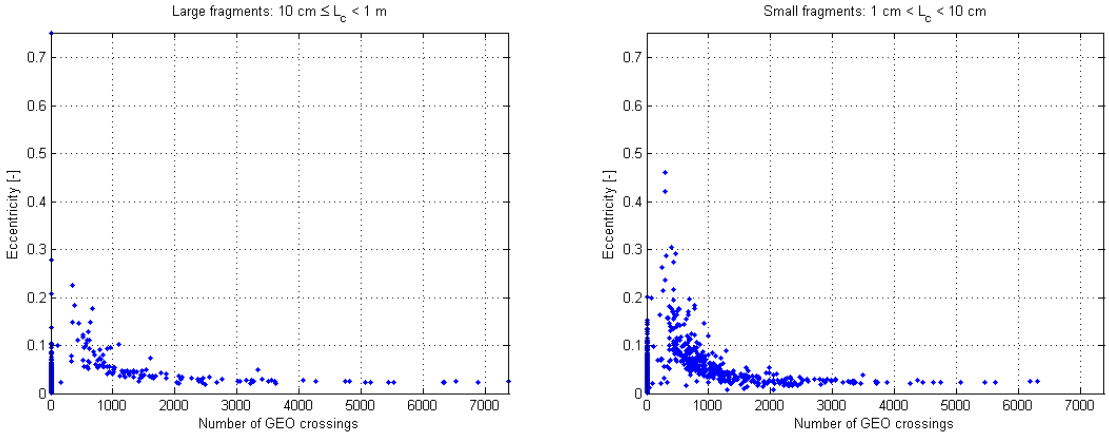


Figure 6.15: Eccentricity and GEO crossings of large (left) and small (right) fragments from the 2000 km above GEO simulation.

### 6.3.2. DIFFERENT INCLINATION

Two simulations were done with the inclination set to 7.4°, which is the Laplace plane inclination. For one of these the altitude was also changed to 1000 km above GEO. With this initial inclination, the inclination changes over time are minimized. Note that for the Laplace plane also $\Omega$ needs to be 0°, which was already the value used for the standard case.

The $i$-$\Omega$ evolution of the small fragments of the case with $i = 7.4°$ is shown in Fig. 6.16. It is clearly different from the standard test case plot in Fig. 6.2. The fragments stay much closer together, the maximum inclination is lower and the minimum inclination higher. The number of total crossings for this test case is only

slightly reduced with 2.8%, however the weighted crossings are reduced by 47%. The lower weighted crossings are caused by the difference in inclination evolution, which changes the crossing velocities. Still, the reduction in weighted crossings is small compared to the results where only the altitude was increased. For example increasing the altitude by 1000 km reduces weighted crossings by 68%, while also reducing the number of total crossings by 61%. This only requires a $\Delta V$ of 29.1 m/s, compared to 404 m/s for the inclination change to 7.4°.

When changing the altitude to 1000 km above GEO in addition to the inclination change, the reduction in number of crossings is almost equal to that of only changing the altitude (61.5% as opposed to 61.4%). The reduction in weighted crossings is increased to 87%, which is still smaller than the reduction of 90% found from increasing the altitude to 2000 km, which still requires significantly less $\Delta V$ than changing the inclination.

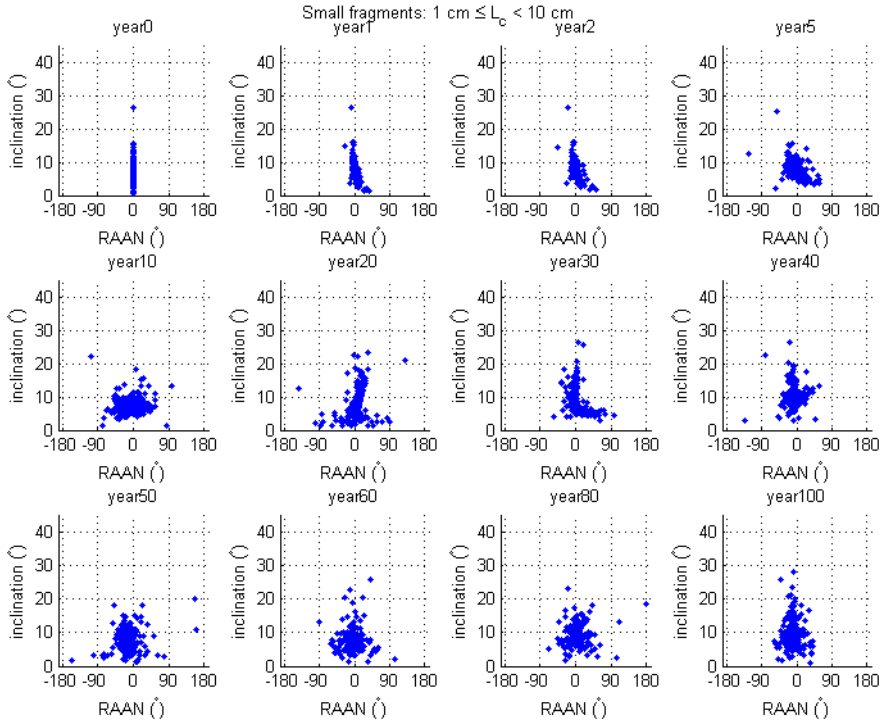


Figure 6.16: $i$-Ω evolution of small fragments from $i = 7.4°$ test case.

## 6.4. SUMMARY

A standard test case was discussed which showed the general behaviour of explosion fragments in a conventional graveyard orbit. The fragments had a $i$-Ω evolution similar to a GEO satellite, even though the initial orbits are changed with the explosion $\Delta V$. Also a pattern was found in the eccentricity-GEO crossings plot, where fragments with high eccentricities always had a small number crossings, and fragments with high numbers of crossings low eccentricities. This seems mostly related to the argument of periapsis. When eccentricity is larger, the range of $\omega$ values where crossings are possible becomes smaller and the number of crossings is reduced. There is also a concentration of fragments with zero crossings. In total three of these fragments were analysed and for each of them the perigee altitude always stayed more than 50 km above GEO, which is the reason there are no crossings.

The sensitivity analysis showed that especially parameters that affect the $\Delta V$ direction or initial velocity direction are important. For example when the initial inclination or the true anomaly was changed. This produced changes in weighted crossings of about 20%, similar to when different RNG seeds are used. Changing the magnitude of the $\Delta V$ by ±50% actually produced smaller differences in weighted crossings than chang-

ing the inclination to 15°. When the mass was changed to 3000 kg the number of crossings is increased by 172%, due to an increased number of fragments, while the weighted crossings are decreased by 19%, as the weighted crossing computation compensates for the increased mass.

Several simulations were done with alternative graveyard orbits, which means the initial orbit where the explosion takes place was changed. Different altitudes were investigated, as well as an inclination of 7.4° (the Laplace plane inclination). The results showed that increasing the altitude can be very effective at reducing both the number of crossings and the weighted crossings. A graveyard orbit 2000 km above GEO reduces the number of crossings from explosion fragments by 83% and the weighted crossings by 90%, compared to the standard graveyard orbit 300 km above GEO. The differences are also much larger than those found in the sensitivity analysis, which shows the results are reliable. However a large $\Delta V$ is required to reach an altitude of 2000 km above GEO, equal to the $\Delta V$ for 13 months of station-keeping. This is very expensive for satellite operators, as it would reduce the operational lifetime of a satellite and hence the corresponding revenues. The altitude increase was shown to be more effective in reducing crossings than changing the inclination, which requires an extremely large $\Delta V$ equal to 7.7 years of station-keeping. However the 2000 km increase may still be too expensive to actually use.

# 7

# COLLISION RESULTS

This chapter discusses the results of collision simulations, in a way similar to the explosion results chapter. First the standard test case is described, which is similar to the explosion standard test case except for some input parameters that are specific to collisions. This is followed by the sensitivity analysis and alternative graveyard orbits sections, which both contain simulations with small changes from the standard test case. The chapter is concluded with a summary of the results.

## 7.1. STANDARD TEST CASE

The standard collision test case is similar to the standard explosion test case, except for some collision-specific input parameters. Also a different seed value is used. Using the same seed would not make the results of the explosion and collision more comparable anyway, since the number of fragments is different. Therefore the same method was used with five different seed values, of which one was chosen for the standard test case.

The input settings for the standard collision test case are shown in Table 7.1. The differences with the explosion test case are the following. The small fragment factor is set to 30, since the number of small fragments is larger (45861 as opposed to 23826). This still results in a total computation time between 1.5 and 2 hours. The scaling factor is not part of the collision simulation model. Instead, the intact satellite mass and collision velocity are used. A projectile mass is also required, to compute whether the collision is catastrophic and how large the fragment mass is if it is not catastrophic. The masses are both set to 1000 kg, which means a simulation is done of two 1000 kg satellites colliding with each other. The collision velocity is set to 810 m/s, which is the relative velocity when satellites collide at a 15° angle (the maximum inclination difference between two satellites in GEO). Note that only the fragments of one of the satellites are propagated, the 'intact satellite mass' satellite, with the initial orbit specified in the input. The fragments of the 'target mass' could also be simulated with a separate simulation, where the initial orbit is changed and the two masses are interchanged (if they are not equal).

The standard collision test case resulted in a catastrophic collision with 17 fragments with $L_c > 1$ m, 895 fragments with 10 cm $\leqslant L_c < 1$ m and 45861 with 1 cm $\leqslant L_c < 10$ cm. The number of large fragments is 50% higher than for the explosion test case, while the number of small fragments is 92% higher. This difference between the increase of large and small fragments is due to the exponential characteristic length distribution function.

Although the mass is given as an input, the total mass of all the fragments will never be exactly equal to the input mass, since the AMR is randomly generated (although the mean and standard deviation are specified by the fragmentation model). The area is also computed, as a function of the characteristic length (without random numbers). The AMR and area are then used to compute the mass of each fragment, therefore the mass is random as well. For the standard test case the total mass of the fragments is 1100 kg. Fig. 5.26 shows that there can be large variations in total mass, in fact all masses in this plot were above 1000 kg, probably because the model is not accurate for very large fragments, which are therefore excluded from the simulation.

Table 7.1: Settings for standard collision test case

| **Initial orbit of intact spacecraft** | |
|---|---|
| $a$ [km] | 42464 (300 km above GEO) |
| $e$ [-] | 0.0 |
| $i$ [°] | 0.0 |
| $\omega$ [°] | 0.0 |
| $\Omega$ [°] | 0.0 |
| $\theta$ [°] | 0.0 |
| **RNG** | |
| Seed | 132 |
| **Fragmentation simulation** | |
| $L_c$ lower limit [m] | 0.01 |
| $L_c$ small fragment [m] | 0.1 |
| $L_c$ upper limit [m] | 1.0 |
| Small fragment factor [-] | 30 |
| Intact satellite mass [kg] | 1000 |
| Projectile mass [kg] | 1000 |
| Collision velocity [m/s] | 810 |
| **Propagator** | |
| $C_R$ [-] | 1.3 |
| Target mass [kg] | 1000 |
| Crossing distance [km] | 50 |
| Start date | January 1, 1900, 00:00 |
| Duration [yr] | 100 |
| **Perturbations** | |
| $J_2$ | true |
| $3^{rd}$ body Sun | true |
| $3^{rd}$ body Moon | true |
| SRP | true |

The limit above which fragments are excluded is set to 1 m, which is the same as for the explosion test case.

The $i$-$\Omega$ evolution of the collision fragments is shown in Figs. 7.1 and 7.2. The fragments again follow a pattern similar to that of a GEO satellite (shown in Fig. 6.3). Compared to the explosion test case both the small and large fragments are closer together in the plots, which is caused by the smaller $\Delta V$s in the collision model. For the same reason, the $i$-$\Omega$ evolution periods of the fragments are closer to the typical 53 years, which is visible in the 50 and 100 year plots, where most fragments have not yet completed a full cycle.

The GEO crossings of the fragments are plotted versus their $L_c$ and AMR in Fig. 7.3. A similar pattern is found as with the explosion test case (Fig. 6.4), except for the lower left plot. For the collision, there is a similar pattern for the large and small fragments, although for the large fragments it is less dense (due to the smaller number of fragments) and the maximum AMR is lower, which is related to the different AMR distribution function for small and large fragments. For the explosion test case this pattern is not visible for the large fragments. This might be related to the lower $\Delta V$s of the collision simulation. Both the $\Delta V$ and AMR values have influence on the number of crossings. The $\Delta V$ determines the initial orbit of a fragment, while the AMR affects how the orbit evolves over time. If $\Delta V$s are lower, then the influence of AMR becomes relatively larger, and perhaps that is why their is a clearer pattern for the collision test case.

Histogram plots of the GEO crossings by the fragments are shown in Figs. 7.4 and 7.5 for respectively the large and small fragments. There is a peak of 0-crossing fragments for both the large and small fragments. This peak is higher than it was for the explosion test case. For the explosion 29% of the large fragments and 9.7% of the small fragments had 0 crossings, while for the collision it is 57% and 20%. This is again caused by the smaller $\Delta V$s. In fact similar results were found in the explosion sensitivity analysis when the $\Delta V$ was halved, the percentages of 0-crossing fragments were then 43 and 15% (see Table 6.4).

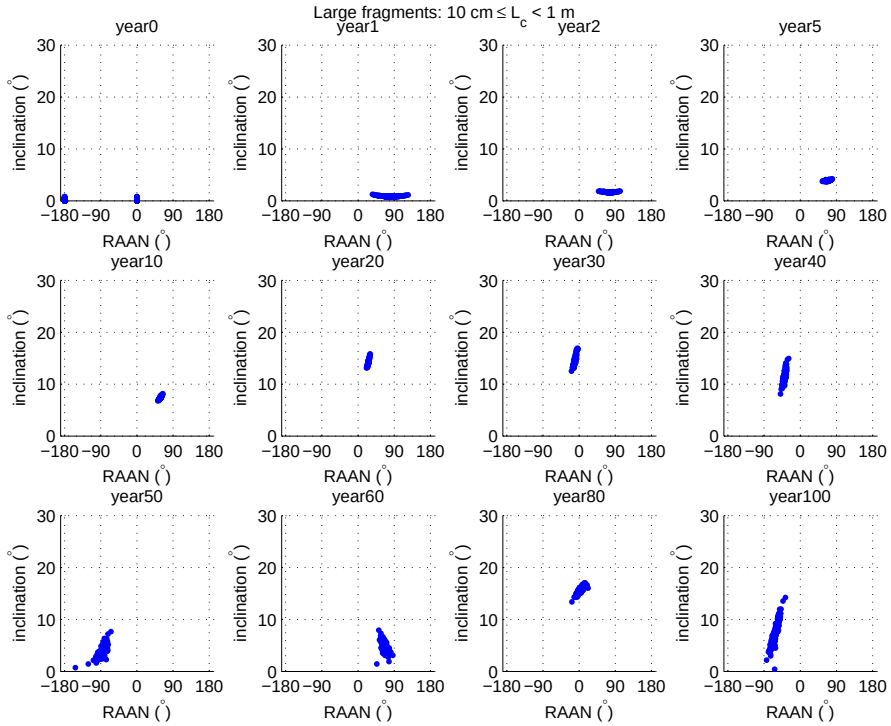


Figure 7.1: $i$-$\Omega$ evolution of large fragments from standard collision test case.

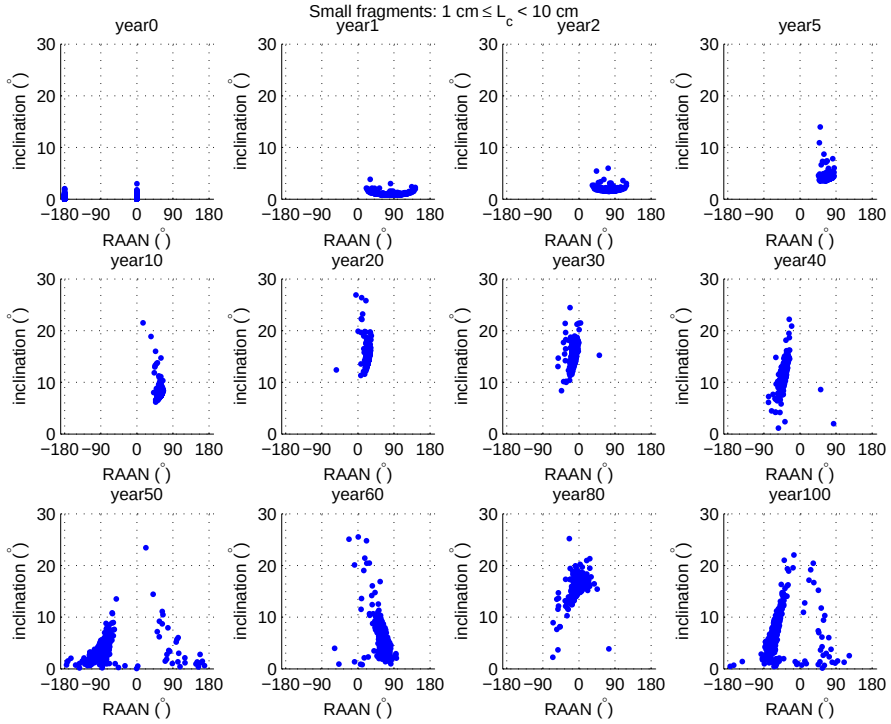


Figure 7.2: $i$-$\Omega$ evolution of small fragments from standard collision test case.

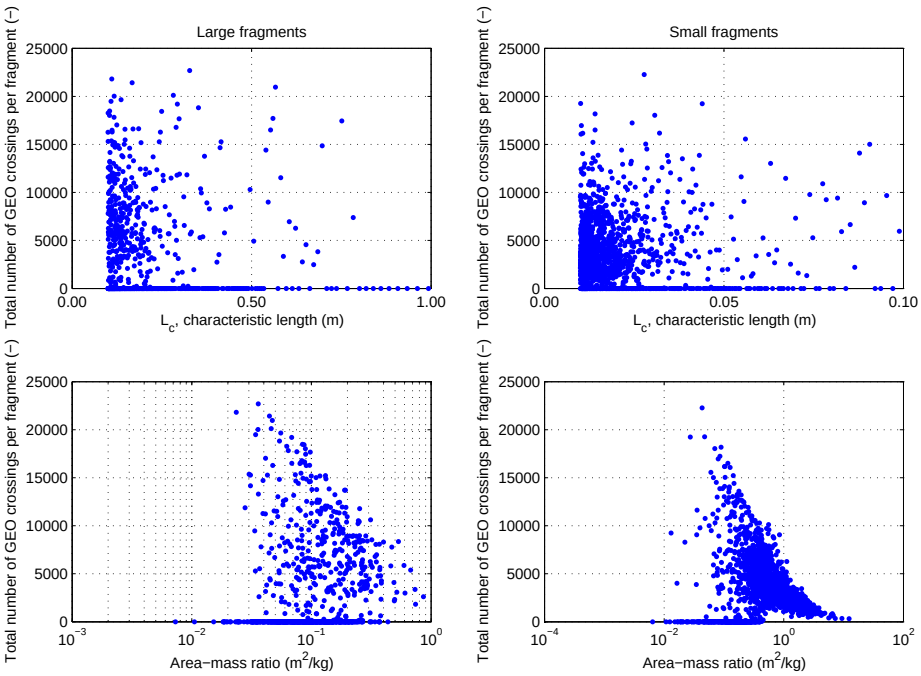


Figure 7.3: Crossings of individual fragments plotted versus $L_c$ and AMR for standard collision test case.

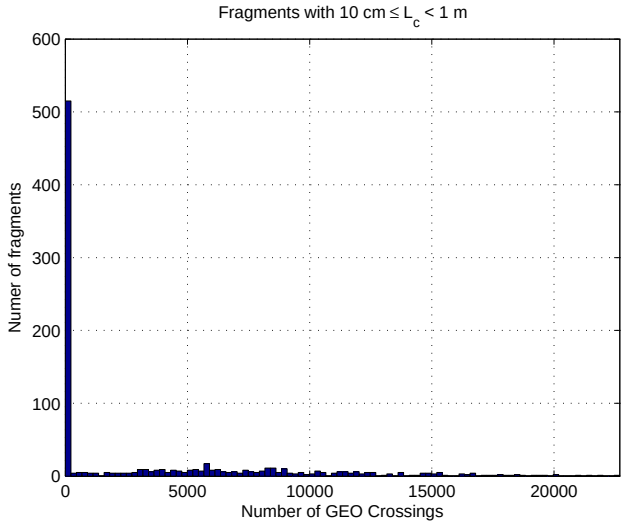


Figure 7.4: Histogram plot of GEO crossings of fragments with 10cm $\leqslant L_c <$ 1m from standard collision test case.

The eccentricity-crossings plots are shown in Fig. 7.6. There is a significant difference between the small and large fragments plot, which was not the case for the explosion test case. The maximum eccentricity for the large fragments is only about 0.05, while for the small fragments it is over 0.25. For the explosion these were 0.6 and 0.45; the large fragments actually had a higher maximum than the small fragments, but this was due to a single outlier, the second highest is below 0.3. The reason the small fragments have lower eccentricities than those of the explosion test case is that the $\Delta V$ values are lower. The mean of the $\Delta V$ distribution increases with AMR, which is the reason that in both cases the small fragments typically have higher eccentricities than the large fragments. However, for the collision test case the difference between the small and large fragments is much larger. This is also caused by differences in the $\Delta V$ distribution function (see Eqs. 4.17 and 4.20). For collisions the mean $\Delta V$ increases more strongly with AMR, which means higher AMR values are more likely to have high $\Delta V$ values, which are required to reach high eccentricities. This is also illustrated by the

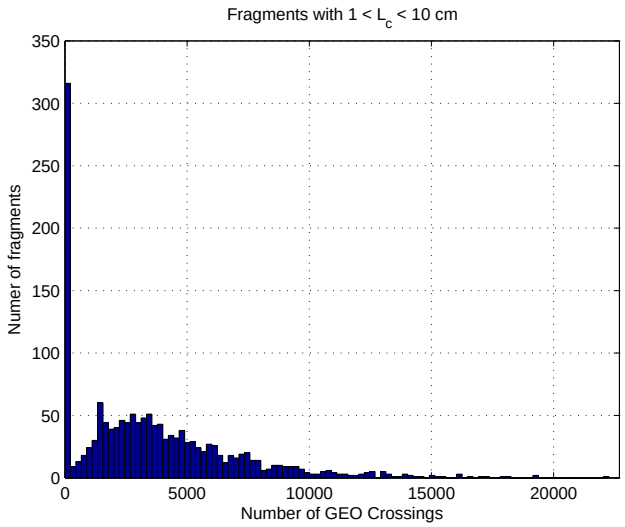


Figure 7.5: Histogram plot of GEO crossings of fragments with 1cm ≤ $L_c$ < 10cm from standard collision test case.

eccentricity-crossings-AMR color plots in Appendix E. It is clear that the large fragments have lower AMR values and also the for the small fragments the ones with high eccentricities have the highest AMR values.

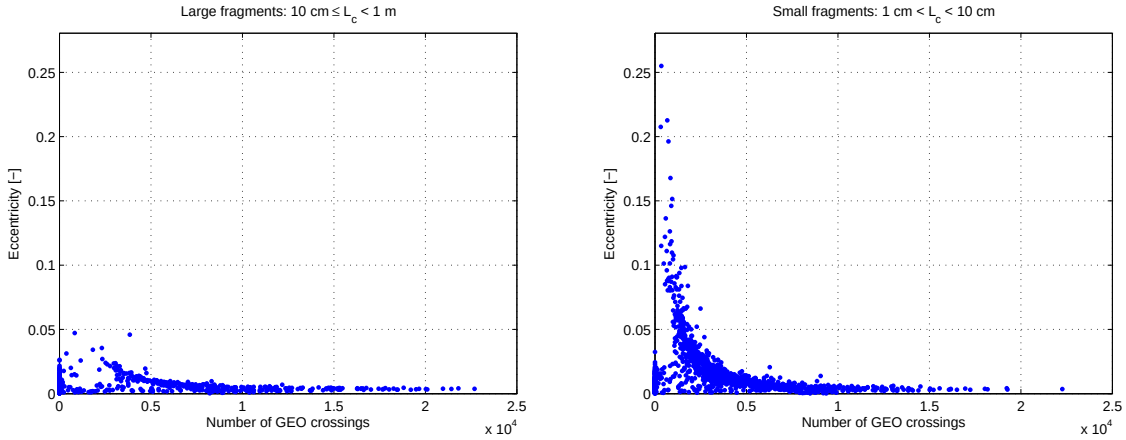


Figure 7.6: Eccentricity and GEO crossings of large (left) and small (right) fragments from the standard collision test case.

The total GEO crossings of all fragments are plotted versus time in Fig. 7.7. The number of GEO crossings increases almost linearly with time, while for the weighted crossings the curve flattens around 50 years when the inclinations of the fragments are low. This is similar to the standard explosion test case. The total number of crossings after 100 years is 1.70E8, which is 172% higher than for the explosion test case. This is partially due to the number of fragments, which is 92% higher (mostly due to the increase in small fragments). It may also be caused by the lower $\Delta V$s resulting in more low eccentricity-high crossings fragments. At the same time, low eccentricities result in low crossing velocities, which in addition to lower inclinations may explain why the weighted crossings are only 22% higher than the explosion test case, despite the much higher number of crossings.

## 7.2. SENSITIVITY ANALYSIS

This section discusses the sensitivity analysis of the collision model. The collision model is very similar to the explosion model. Only the number of fragments is computed differently and the $\Delta V$ distribution is different, although it is still a normal distribution just like the explosion $\Delta V$ distribution. Since it is very similar, most of the simulations that were done for the explosion sensitivity analysis are not repeated here. Only the

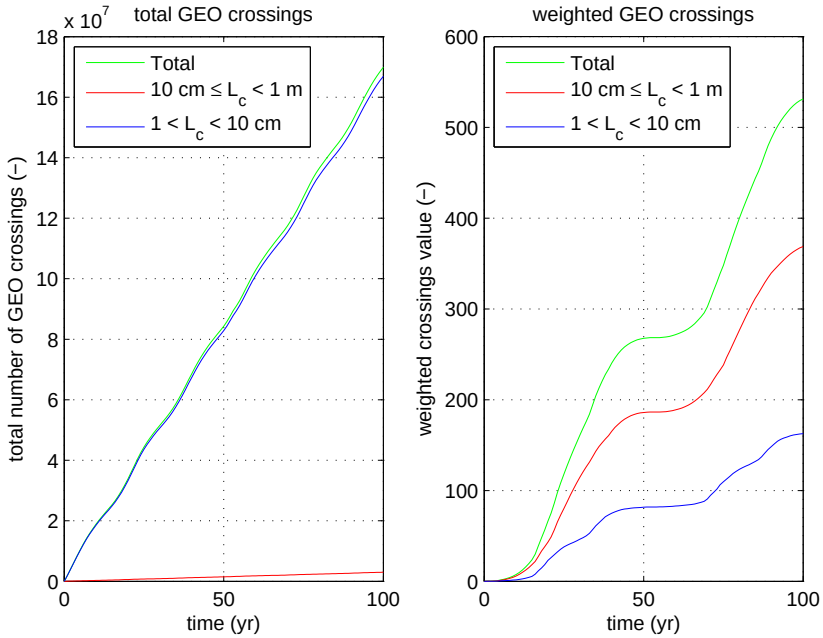


Figure 7.7: Total number of GEO crossings plotted versus time for standard explosion test case.

simulation with $i = 15°$ and $\theta = 180°$ is repeated, since this was one of the simulations that produced the largest differences from the standard test case. The other simulations are for parameters that are specific to the collision model. The results of each simulation are discussed in this section.

Table 7.2: GEO crossings results of sensitivity analysis for collisions. The crossings and weighted crossings percentages of the small and large fragments are percentages of the total values, while the 0-crossing fragment percentages are of the total number of fragments.

| | **GEO crossings** | | | **Weighted crossings** | | | **0-crossing fragments** | |
|---|---|---|---|---|---|---|---|---|
| **Test setup** | **Total** [-] | **Large** [%] | **Small** [%] | **Total** [-] | **Large** [%] | **Small** [%] | **Large** [%] | **Small** [%] |
| **Standard test case** | 1.70E8 | 1.8 | 98.2 | 531 | 69.4 | 30.6 | 56.7 | 19.6 |
| $V_{COL} \cdot 0.5$ | 1.70E8 | 1.8 | 98.2 | 531 | 69.4 | 30.6 | 56.7 | 19.6 |
| **Non-uniform $\Delta V$ direction** | 1.32E8 | 1.5 | 98.5 | 284 | 76.2 | 23.8 | 68.5 | 25.8 |
| **NASA $\Delta V$ distribution** | 5.63E7 | 3.4 | 96.6 | 715 | 77.2 | 22.8 | 13.6 | 5.3 |
| $i = 15°, \theta = 180°$ | 1.75E8 | 1.7 | 98.3 | 499 | 81.9 | 18.1 | 55.2 | 19.2 |

Table 7.3: GEO crossings results of sensitivity analysis for collisions, percentage difference w.r.t. standard test case. For the crossings and weighted crossings, the difference of the small fragments are w.r.t. the actual number of crossings by these fragments, not the percentage of Table 7.2.

| | **GEO crossings [%]** | | | **Weighted crossings [%]** | | | **0-crossing fragments [%]** | |
|---|---|---|---|---|---|---|---|---|
| **Test setup** | **Total** | **Large** | **Small** | **Total** | **Large** | **Small** | **Large** | **Small** |
| $V_{COL} \cdot 0.5$ | 0.0 | 0.0 | 0.0 | 0.0 | 0.0 | 0.0 | 0.0 | 0.0 |
| **Non-uniform $\Delta V$ direction** | -22.2 | -34.3 | -21.9 | -46.5 | -41.2 | -58.4 | 20.9 | 32.1 |
| **NASA $\Delta V$ distribution** | -66.9 | -35.3 | -67.4 | 34.5 | 49.6 | 0.1 | -76.1 | -73.1 |
| $i = 15°, \theta = 180°$ | 3.2 | -0.7 | 3.3 | -6.1 | 10.9 | -44.5 | -2.6 | -1.7 |

### 7.2.1. $V_{COL} \cdot 0.5$

The standard test case uses a collision velocity based on an inclination difference of 15°. This is the maximum difference possible in the standard graveyard orbit, which means usually the collision velocity will be lower. This is why one simulation was done where the collision velocity is multiplied by 0.5, resulting in a velocity of

410 m/s. The results are exactly the same as for the standard test case, with all the differences equal to 0. This may seem surprising, however it can be explained by the way the collision model works. The collision velocity is used to compute whether a collision is catastrophic or not. If it is catastrophic, then the fragment mass is equal to the satellite mass. This mass is then used to compute the fragments. If a collision is not catastrophic, the fragment mass is computed based on the relative kinetic energy of the collision.

This simulation with lower crossing velocity still resulted in a catastrophic collision, therefore the fragment mass and the subsequently generated individual fragments are exactly the same as for the standard test case. The model is such that there are no differences in catastrophic collisions with different collision velocities. For a collision to be catastrophic, the impact energy must be at least 40 J/g. This means that when two objects of equal mass collide, a collision velocity of at least 283 m/s is required for the collision to be catastrophic.

### 7.2.2. NON-UNIFORM $\Delta V$ DIRECTION

In the standard test case the $\Delta V$ directions are randomly generated in a way that they would have a uniform distribution over a sphere. This distribution was chosen since the NASA breakup model does not actually describe any distribution for the $\Delta V$ direction, only for the magnitude. The Iridium-Cosmos collision, discussed in Section 4.4, shows that it is also possible for the distribution to be non-uniform. In this collision the $\Delta V$ of the fragments slightly favoured the direction of impacting satellite's velocity. This sensitivity analysis investigates how such a non-uniform distribution might affect the simulation results.

The $\Delta V$ direction is usually computed by generating a random vector as described in Section 5.1.3. For this simulation the mean of the y-component was set to 0.5. This means the $\Delta V$ is more likely to be in the positive y-axis direction. With the chosen initial orbit and position, this direction is the velocity direction of the satellite. This is not ideal, since it should be towards the direction of the other satellite. However in this simulation the differences between the satellites' velocity vectors is only 15°, so the difference in the $\Delta V$ directions is small.

From the fragments of the standard test case 1203 out of 2424 (49.6%) have a $\Delta V$ with a positive y-component. With the modified distribution this is increased to 1672 (69%). This greatly affects the number of crossings, which is reduced by 22%. The weighted crossings are reduced by an even greater 46%. Perhaps the 0.5 mean value for the y-component was a bit high (there is not quite enough data to find a realistic number), however it does show that the $\Delta V$ direction is very influential. This was also concluded from some of the simulations of the explosion sensitivity analysis, where changing parameters that change the initial velocity direction of the satellite produced the largest differences compared to the standard test case.

### 7.2.3. NASA $\Delta V$ DISTRIBUTION

For most of the fragmentation simulation the NASA breakup model is used, however for the collision $\Delta V$ distribution a modification for low-velocity collisions is used, since the NASA model is based on hyper-velocity collisions. One simulation has been done using the distribution from the NASA model, to investigate the differences.

At first there was actually an error during the orbit propagation part of the simulation. This was caused by a fragment that obtained an eccentricity larger than 1 during the propagation, while the orbit dynamics model only works for elliptical orbits. Fragments with initial eccentricities larger than 1 due to the applied $\Delta V$ were already removed. There were 108 such fragments, which is much larger than for the explosion simulations, where at most 1 was found. This part of the software was further modified by setting the limiting value for the initial eccentricity to 0.99. This caused one additional fragment to be removed (resulting in a total of 109), and the software was able to run without problems again.

The large number of fragments with hyperbolic orbits is caused by the higher $\Delta V$s with this distribution. There are also 76 and 73% fewer large and small 0-crossing fragments, although the total number of crossings also reduces by 67%. Both these differences are caused by higher eccentricities, since small eccentricities are required both for 0-crossing fragments and for fragments with many crossings. Part of the reduction in crossings is also caused by the fragments with hyperbolic orbits, which cannot have crossings.

Also the $i$-$\Omega$ evolution and eccentricity-GEO crossings plots look very different from the standard test case,

especially for the small fragments. These are shown in Figs. 7.8 and 7.9. The fragments have extremely high inclinations, some even close to 180°. The eccentricities are also very high, with many close to 1. The eccentricity-GEO crossings plot actually showed a single outlier with e > 5. This fragment probably developed an eccentricity larger than 1 due to perturbations, after which the software was not able to accurately propagate the orbit, since the models used are only applicable to elliptical orbits. The results of this fragment are therefore unreliable, however they do not affect the total crossing results since the fragment has zero crossings.

The high inclinations and eccentricities cause the fragments to have high crossing velocities, which is likely the reason that the weighted crossings are 34% higher than the standard test case even though the number of crossings is reduced by 67%.

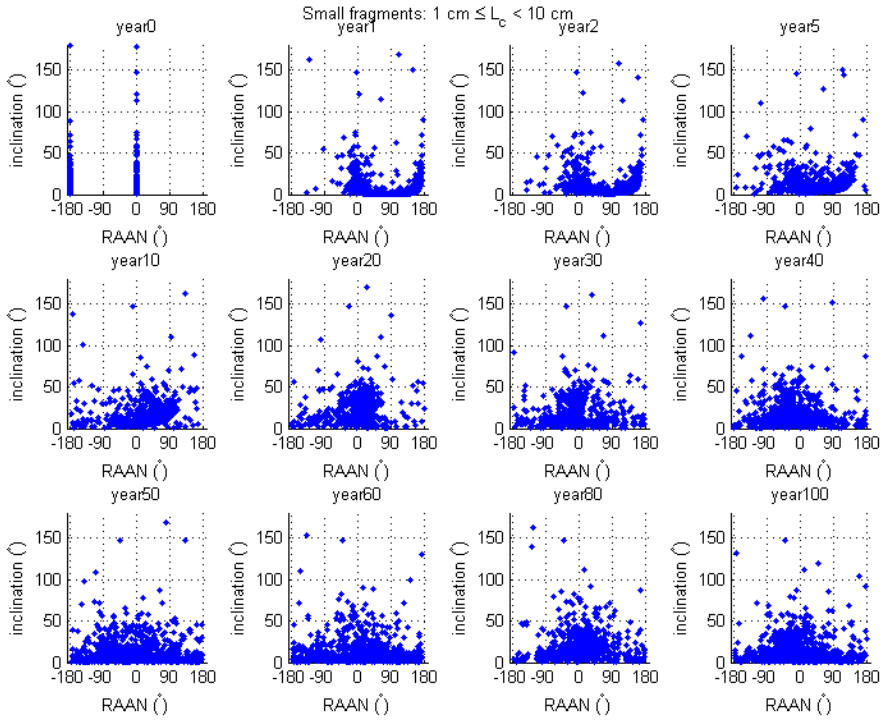


Figure 7.8: $i$-$\Omega$ evolution of small fragments from collision test case with NASA model $\Delta V$ distribution.

### 7.2.4. $i = 15°, \theta = 180°$

This simulation is included since it it was found to be one of the most influential ones in the explosion sensitivity analysis, where it reduced the weighted crossings by 22% relative to the standard test case. This difference was similar to the differences between different seeds values. For the collision test case the difference is only -6.1%, which is in line with the results from the different seeds where differences were also much smaller than for explosions with at most 9.4%.

## 7.3. ALTERNATIVE GRAVEYARD ORBITS

In this section the effects of using different graveyard orbits for collision simulations is analysed. An important difference with respect to the explosion simulations is that for collisions the $\Delta V$s are on average smaller. Also it is possible for collisions to be non-catastrophic if the impact energy is too low (due to low projectile mass or low collision velocity). In such a case only a fraction of the total satellite mass is fragmented, resulting in fewer fragments and crossings. The simulation results are summarized in Tables 7.4 and 7.5

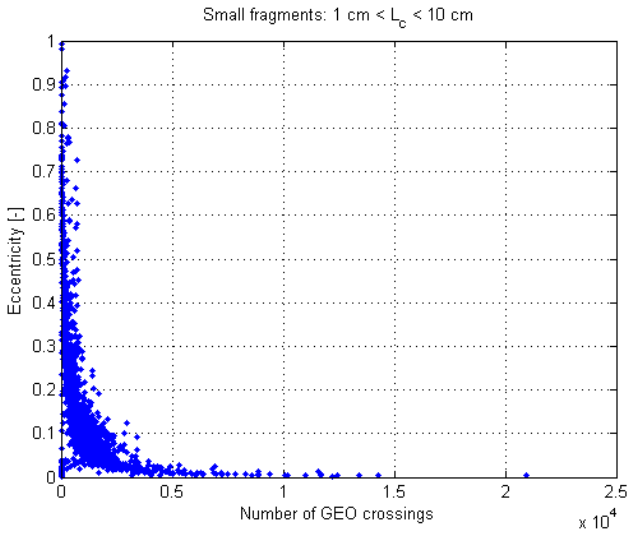


Figure 7.9: Eccentricity-GEO crossings plot of small fragments from collision test case with NASA model $\Delta V$ distribution.

Table 7.4: GEO crossings results of collision simulations in alternative graveyard orbits. The crossings and weighted crossings percentages of the small and large fragments are percentages of the total values, while the 0-crossing fragment percentages are of the total number of fragments.

| | GEO crossings | | | Weighted crossings | | | 0-crossing fragments | |
|---|---|---|---|---|---|---|---|---|
| **Test setup** | **Total [-]** | **Large [%]** | **Small [%]** | **Total [-]** | **Large [%]** | **Small [%]** | **Large [%]** | **Small [%]** |
| **Standard case** | 1.70E8 | 1.8 | 98.2 | 531 | 69.4 | 30.6 | 56.7 | 19.6 |
| **500 km above GEO** | 1.02E8 | 1.0 | 99.0 | 202 | 46.5 | 53.5 | 78.4 | 35.4 |
| **1000 km above GEO** | 3.65E7 | 0.5 | 99.5 | 30 | 62.5 | 37.5 | 95.3 | 62.0 |
| **2000 km above GEO** | 7.93E6 | 0.2 | 99.8 | 2.3 | 70.7 | 29.3 | 99.2 | 84.0 |
| $i = 7.4°$ | 7.66E6 | 2.2 | 97.8 | 26 | 86.8 | 13.2 | 54.8 | 22.3 |

Table 7.5: GEO crossings results of collision simulations in alternative graveyard orbit, percentage difference w.r.t. standard case. Differences in crossings are differences between the absolute values of the crossings, while the difference in 0-crossing fragments is the difference in the percentage of 0-crossing fragments.

| | GEO crossings [%] | | | Weighted crossings [%] | | | 0-crossing fragments [%] | |
|---|---|---|---|---|---|---|---|---|
| **Test setup** | **Total** | **Large** | **Small** | **Total** | **Large** | **Small** | **Large** | **Small** |
| **500 km above GEO** | -39.8 | -65.3 | -39.3 | -61.9 | -74.5 | -33.5 | 38.5 | 80.9 |
| **1000 km above GEO** | -78.5 | -94.4 | -78.2 | -94.4 | -95.0 | -93.2 | 68.2 | 217 |
| **2000 km above GEO** | -95.3 | -99.5 | -95.3 | -99.6 | -99.6 | -99.6 | 75.1 | 329 |
| $i = 7.4°$ | -95.5 | -94.5 | -95.5 | -95.1 | -93.9 | -97.9 | -3.3 | 14.1 |

### 7.3.1. DIFFERENT ALTITUDE

Similar to the explosion results, increasing the altitude of the graveyard orbit significantly reduces the crossings by collision fragments, with increasing differences for higher altitudes. With a graveyard altitude 2000 km above GEO the number of crossings is reduced by 95.3% and the weighted crossings by 99.6%. This reduction is higher than for the explosion test case with the same altitude, where crossings were reduced by 83% and weighted crossings by 89.9%. Note that an altitude 1000 km above GEO also greatly reduces crossings. The total number of crossings is reduced by 78.5%, while the number of crossings by large fragments as well as the total weighted crossings are reduced by 94.4%. The altitude 500 km above GEO results in the smallest differences, with a reduction in total number of crossings by 40% and total weighted crossings by 62%. For the altitudes of 500 and 1000 km above GEO the reduction in crossings is also higher for collisions than for explosions

The difference between the collision and explosion results is caused by the smaller $\Delta V$s in the collision simu-

lations. With smaller $\Delta V$s the initial orbits of the fragments have lower eccentricities which causes the altitude increase to more effectively reduce crossings.

### 7.3.2. DIFFERENT INCLINATION

With the inclination set to 7.4° the initial orbit of the satellite before the fragmentation is in the Laplace plane, where inclination changes over time are minimized. An inclination difference of 2.4° was assumed to compute the collision velocity, this is the maximum possible when starting in the Laplace plane, even if it is not optimized by setting the inclination and RAAN in phase with the lunar nodal regression to further reduce the amplitude of the inclination evolution.

The low collision velocity causes a non-catastrophic collision, which means only a part of the satellite's total mass is fragmented. In this scenario a total fragment mass of 16.6 kg should be produced. After generating the fragments with this mass as input, which includes a random number generator for AMR, a mass of 32.8 kg was found, which quite far from the intended mass. This could be due to random effects and a small number of total fragments. The total number of fragments is much smaller than for the standard test case: 42 large and 2119 small fragments. With this small number of fragments there would probably be much larger difference between simulations with different RNG seeds, compared to the tests that were done with standard case settings and different seeds. This could be the cause for the large difference between the input fragment masses and the actual mass of the generated fragments.

In the equivalent explosion case the number of crossings was almost equal to that of the standard test case. However since the collision is non-catastrophic and the number of fragments is very small, the number of GEO crossings is also much smaller. It is 95.5% smaller than for the standard test case, a similar reduction as for the 2000 km above GEO test case. However the altitude increase is more effective at reducing the weighted crossings, with a 99.6% reduction as opposed to 95.1% with the Laplace plane inclination, mainly because the altitude increment reduces crossings by large fragments more. Note that also for the crossing results there could be large differences between runs with different seeds, due to the small number of fragments, since the sensitivity analysis has shown that the $\Delta V$ directions have a large influence on the results, and these are also determined through generating random numbers. This is especially the case for the weighted crossings since they are mostly due to large fragments, of which there are only 42.

## 7.4. SUMMARY

The results of several simulations have been discussed in this chapter. First a standard test case simulation was performed, with input settings similar to those used for the standard explosion test case. Generally a similar behaviour was seen in the orbits of the fragments just after the fragmentation event and in the orbit evolution over a 100 year period. For example the typical $\Omega$-$i$ evolution of the fragments, which was even clearer for the collision test case since the $\Delta V$s are smaller, which causes the fragments to be closer together in the $\Omega$-$i$ plots. The difference in the $\Delta V$ model is the main source of differences between the explosion and collision results. Due to this the fragments have lower eccentricities and there are more fragments with zero crossings. Also the mean $\Delta V$ increases more with higher AMR, which results high AMR fragments typically having higher initial eccentricities and fewer crossings.

The sensitivity analysis showed that if the collision velocity is half of the maximum, the results are exactly equal to the standard test case since the collision is still catastrophic. In fact a collision velocity of at least 283 m/s is required for a collision between two objects of equal mass to be catastrophic, while the maximum collision velocity for satellites in the standard graveyard orbit is 810 m/s. Any velocity between these two values would result in the same catastrophic collision.

Using the $\Delta V$ distribution of the NASA breakup model resulted in extremely high $\Delta V$s, as the initial inclination of some of the fragments was changed to nearly 180°, meaning the velocity was flipped towards the opposite direction. The fragments also had very large eccentricities, with several ending up in hyperbolic orbits. This proves the necessity of a modified model for low velocity collisions like those in GEO.

The results for higher-altitude graveyard orbits were similar to those of the explosions, although for the collisions the reduction in GEO crossings is even higher due to the lower eccentricities of the fragments due to lower $\Delta V$s. With a graveyard orbit 2000 km above GEO, crossings are reduced by 95.3% compared to the

standard test case, while for explosions this is only 82.8%. This could make higher-altitude graveyard orbits more worth the $\Delta V$ cost, depending on whether there is a higher chance of explosions or collisions to occur. Also a smaller altitude increase still results in large reductions in crossings by collision fragments. For example an altitude 1000 km above GEO results in a reduction of 78.5% in total number of crossings and 94.4% in the number of crossings by large fragments, which are most dangerous. This would require a $\Delta V$ equal to 6.6 months of station-keeping, compared to 2.0 months for the standard disposal orbit. This is more reasonable than the explosion case, where an altitude 2000 km above GEO results in a similar reduction (83%) in crossings, which requires a $\Delta V$ equal to 13.1 months of station-keeping.

One simulation was also done with the Laplace plane as disposal orbit. For explosions this only reduced crossings by 2.8%, however for collisions it is different. Since the maximum inclination difference between satellites in such a graveyard orbit is only 2.4°, the maximum collision velocity is very small and a collision cannot be catastrophic. Because of this only 16.6 kg of the total 1000 kg mass is fragmented, resulting in a much smaller number of fragments and a reduction in the number of crossings by 95.5%. Still it is not much better than using a graveyard orbit 2000 km above GEO, which requires significantly less $\Delta V$.

# 8

# CONCLUSIONS AND RECOMMENDATIONS

The objective of this research was to investigate whether debris from satellite fragmentations in the GEO graveyard orbit is able to intrude into GEO. Additionally it was investigated whether alternative graveyard orbits could be more effective at keeping such debris away from GEO. To investigate this a C++ program was developed to simulate fragmentations and propagate orbits of the resulting fragments. For the fragmentation simulations the NASA standard satellite breakup model was used, along with a modification to the $\Delta V$ distribution for low-velocity collisions, which are typical to GEO. The orbit propagator was based on an averaged orbit dynamics model with Milankovitch orbital elements for fast computations.

The orbit propagator includes the effects of perturbations by $J_2$, solar radiation pressure and third body gravitational perturbations by the Moon and Sun. The propagator was validated by comparing results to other studies that investigated behaviour of debris near GEO. Also various propagator versions with different integrators were compared to each other: averaged orbit dynamics with either a DOPRI8 or RK4 integrator and non-averaged Cowell's method integration with RK4, with both the standard perturbations and added $J_{2,2}$ and Earth shadow effects. An object in GEO was propagated over a 150-year period and the computation time and GEO crossings were compared to each other. A GEO crossing is defined as an object passing within 50 km of GEO. The GEO crossing results were within 3% of each other, however the computation time required for the non-averaged propagation was about 40 minutes, while for averaged propagation it was in the order of seconds. Therefore the averaged orbit dynamics model was used. The RK4 integrator was chosen, because for the GEO crossings computation it is convenient to have constant step-sizes equal to one orbital revolution and with these step-sizes RK4 provided sufficiently accurate results. The propagator was able to simulate the orbit evolution of a single object over a 100-year period within 5 seconds of computation time.

The fragmentation model includes normal distributions for some of the fragment characteristics. In the simulation software a random number generator is used to generate values for these characteristics. This causes every simulation to produce different results, if a new seed value is used. There were very large differences in total masses between iterations with different seed numbers, mostly due to fragments larger than 1 m. The AMR distribution model is probably not accurate for these fragments, as it is meant for fragments up to 35 cm. Since the mass results are still consistent up to 1 m, it was decided to still include these fragments and only exclude the ones larger than 1 m. There are typically only about 20 fragments of this size for a 1000 kg satellite, which means excluding them does not greatly affect GEO crossing results. A lower limit for the fragment size was set to 1 cm. With these fragment size limits, five explosion and collision simulations were performed to asses the consistency of the results. The results showed small variations, within 5% of the average, in total mass and crossings. However weighted crossings were also computed, which are weighted by the total fragment mass that would be produced in the event of a collision, which is affected by the mass of the initial fragment and also the collision velocity. The variations in weighted crossings were up to 21% for explosions and 9% for collisions. For collisions the variations are smaller because the $\Delta V$s are smaller.

A standard test case with a graveyard orbit 300 km above GEO was simulated for both an explosion and collision. This was used as a reference to compare results of a sensitivity analysis as well as simulations in alternative graveyard orbits. The standard explosion test case resulted in 15 fragments larger than 1 m (which are

excluded), 598 large fragments with sizes between 10 cm and 1 m and 23826 small fragments with sizes between 1 cm and 10 cm. The fragments together made a total of 6.24E7 GEO crossings over a 100-year period, or about 1710 per day.

A sensitivity analysis was performed to investigate how changes to input parameters affect the results. The largest differences were caused by parameters that affect the velocity direction of the satellite (for example inclination or true anomaly). Because the initial velocity direction is different, adding the fragment $\Delta V$s produces different results. The results are similar to when using different seed numbers, with variations of about 20% in weighted crossings. Changing the start date by +0.25 years caused a surprisingly large difference of -22% in total number of crossings, which might be caused by differences in perigee altitude evolution.

Various alternative graveyard orbits were compared to the standard one. The investigated orbits had either higher altitudes (at 500, 1000 and 2000 km above GEO) or an inclination of 7.4°, which is the Laplace plane inclination. With the higher altitudes, total crossings are reduced by 28, 61 and 83% for respectively 500, 1000 and 2000 km above GEO. The weighted crossings are reduced slightly more, by 38, 78 and 90%. The reductions in crossings are much higher than differences found in the sensitivity analysis, which shows that the results are reliable. The $\Delta V$s required for transfers to these orbits are equal to the amounts required for respectively 3.3, 6.6 and 13.1 months of station-keeping, which is significantly higher than 2.0 months for the standard case. The Laplace graveyard orbit is very ineffective at reducing crossings, with a reduction of only 2.8%. It does reduce weighted crossings by 47%, however the $\Delta V$ required for a transfer to such an orbit is extremely high, equal to 7.7 years of station-keeping.

The standard collision case resulted in 17 fragments larger than 1 m, 895 large fragments (50% more than the explosion case) and 45861 small fragments (92% more than the explosion case). These fragments made a total of 17.0E7 GEO crossings which equals about 4658 per day.

The sensitivity analysis showed that if the collision velocity is half of the maximum, the results are still the same because the collision is still catastrophic. For two objects of equal mass to be in a catastrophic collision, a minimum collision velocity of 283 m/s is required, while the maximum for satellites in the standard graveyard orbit is 810 m/s. Another simulation was done using the NASA model's $\Delta V$ distribution, for which otherwise a modification was used. This resulted in extremely large $\Delta V$s and fragments obtaining initial inclinations up to 180°, which shows the importance of having a separate distribution for low-velocity collisions.

The alternative graveyard orbits for collisions resulted in larger crossing reductions than for explosions. For altitudes of 500, 1000 and 2000 km above GEO, total crossings were reduced by respectively 40, 78 and 95%. The reductions in weighted crossings are again higher, with 62, 94.4 and 99.6%. The Laplace plane graveyard orbit, which was not effective at reducing crossings for explosions, is also very effective for collisions, with a reduction in crossings by 95.5%. The reason for this is not so much that individual fragments have less crossings, but that a catastrophic collision between satellites is not possible due to the small maximum inclination difference, which result in small collision velocities. With a non-catastrophic collision the number of fragments is significantly smaller, resulting in fewer crossings. Still, the reduction in crossings is about equal to the case with an altitude 2000 km above GEO, which requires far less $\Delta V$.

Although GEO crossings can be greatly reduced by the investigated alternative graveyard orbits, actually using them would be difficult due to the higher $\Delta V$ required to move a satellite from GEO to such an orbit. There would be less $\Delta V$ available for station-keeping, resulting in a shorter operational lifetime of the satellite, which would be expensive for satellite operators while there are no short-term benefits. Also with the current graveyard orbit guidelines already only about one third of the satellites is actually successfully placed in the graveyard orbit, while another one third reaches a lower orbit and the remaining one third is simply abandoned in GEO (Jehn et al., 2005).

Based on the research presented in this report, a graveyard altitude 1000 km above GEO is recommended as it will significantly reduce GEO crossings by debris from fragmentations. Although this is twice as expensive as the 500 km option, the reduction in GEO crossings is also twice as high, while further increasing the altitude to 2000 km above GEO does not further reduce crossings as much. However further research is recommended, to investigate how using alternative graveyard orbits would actually affect the long-term evolution of the entire GEO debris population and the risk for active GEO satellites to be critically damaged by debris. These topics were not considered during this work but could be relevant in determining whether it is necessary to use a different graveyard orbit.

The fragmentation model could also be improved to better simulate the different possible fragmentation events. Currently there is no difference between a high or low energy explosion or catastrophic collisions. If a satellite has an explosion with only a small amount of propellant left, which would be the case for a satellite in a graveyard orbit, then perhaps it is possible that not the entire satellite is fragmented or that de $\Delta V$s of the fragments are lower. There is a similar issue with the collision model. For a catastrophic collision between two equal masses a collision velocity of at least 283 m/s is required, while collision velocities up to 810 m/s are possible in GEO. With the current model these collisions would be identical and result in the same fragment characteristics.

The model also does not include a $\Delta V$ direction distribution, it only includes a distribution for the magnitude of the $\Delta V$. The $\Delta V$ direction has therefore been assumed to be random, but this may not be appropriate for collisions, as observations from the Iridium 33 - Cosmos 2251 collision have shown that $\Delta V$s are more likely to be in the direction of the velocity of the impacting object. However this is only one example, more research would be required to know if this happens for all collisions and if it is the same for low-velocity collisions in GEO as for hyper-velocity collisions in LEO. This would be difficult to investigate though, considering that the Iridium-Cosmos collision up to now has been the only catastrophic collision.

# A

# IRIDIUM 33 - COSMOS 2251 COLLISION ΔV

This appendix shows $\Delta V$ distributions of fragments from the Iridium-Cosmos collision, which have been computed by propagating observed fragments backwards to the time of the collision. The plots show that fragments are more likely to have $\Delta V$s in the direction of the impacting satellite than in other directions.

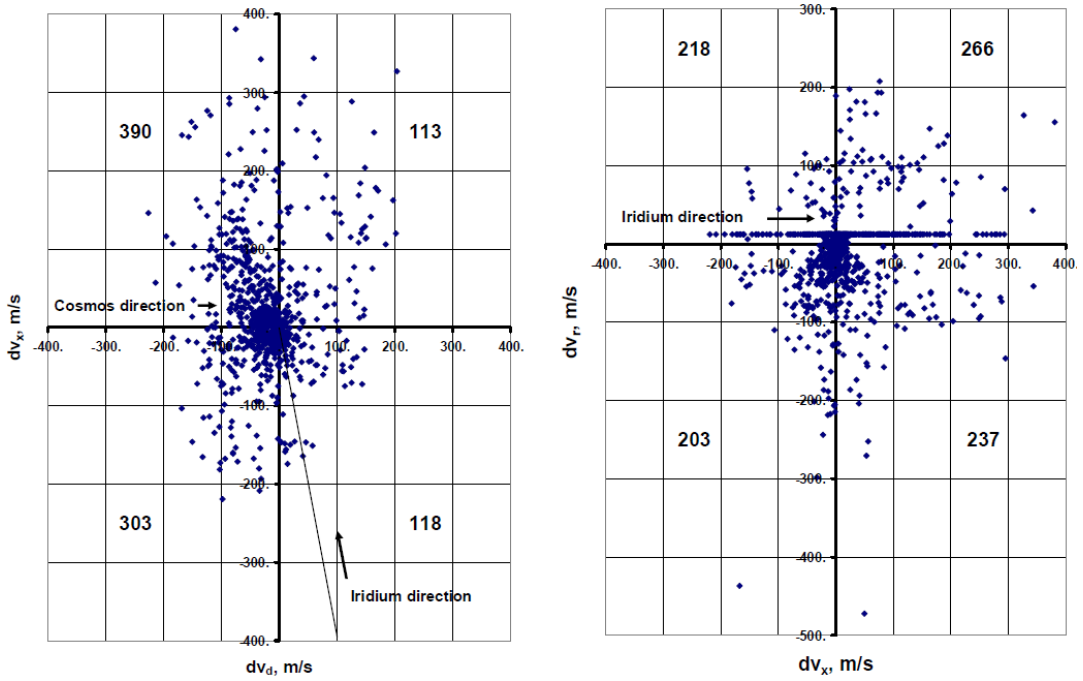


Figure A.1: Cosmos 2251 fragments $\Delta V$ in down-range ($dv_d$), cross-range ($dv_x$) and radial ($dv_r$) directions. The directions of the colliding satellites and the number of fragments in each quadrant is also shown (Tan et al., 2013).

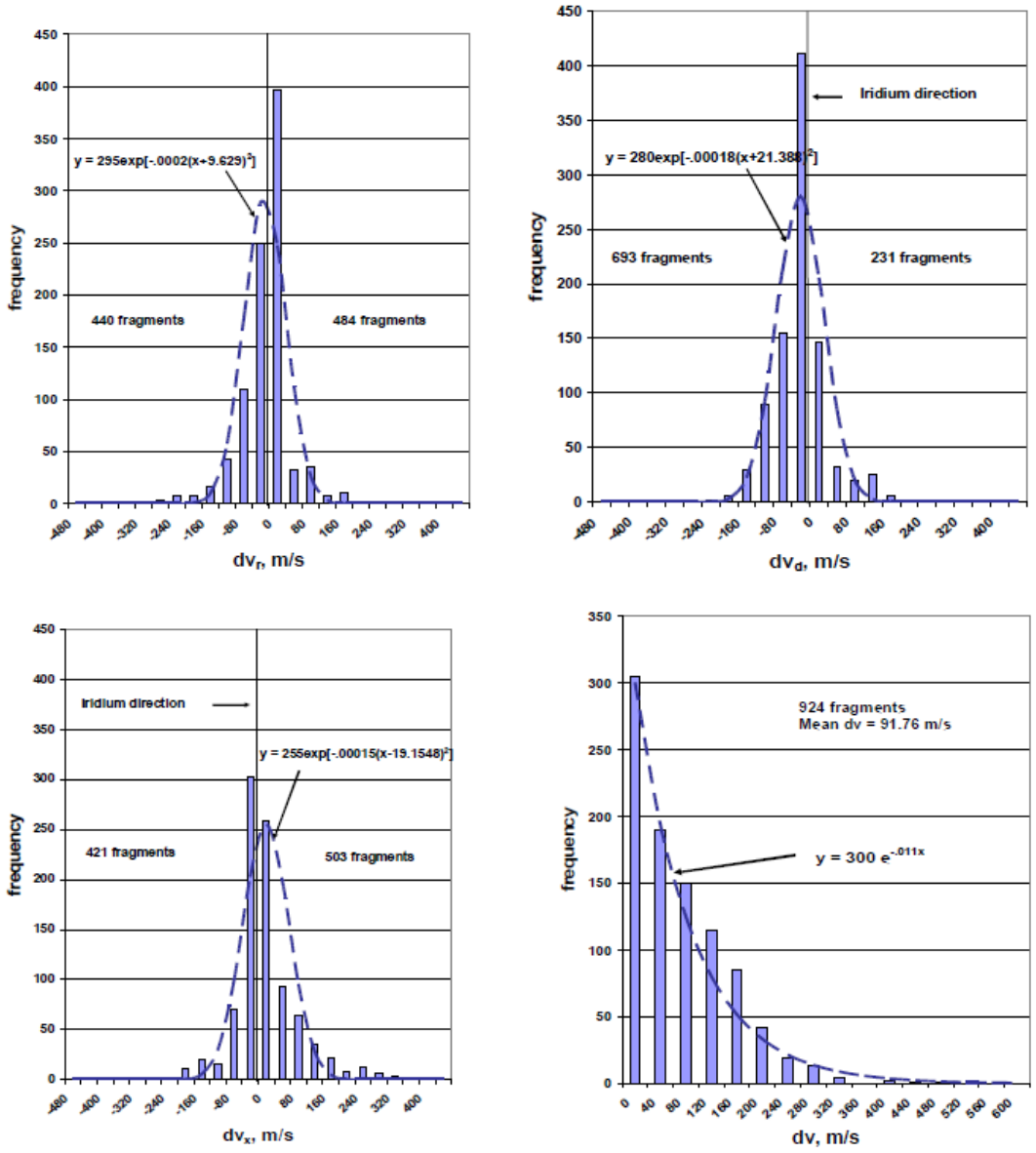


Figure A.2: Histogram plots with fitted normal distribution curve of Cosmos 2251 fragments $\Delta V$, including components in down-range ($dv_d$), cross-range ($dv_x$) and radial ($dv_r$) directions. The number of fragments with positive and negative $\Delta V$ is also displayed in the plots (Tan et al., 2013).

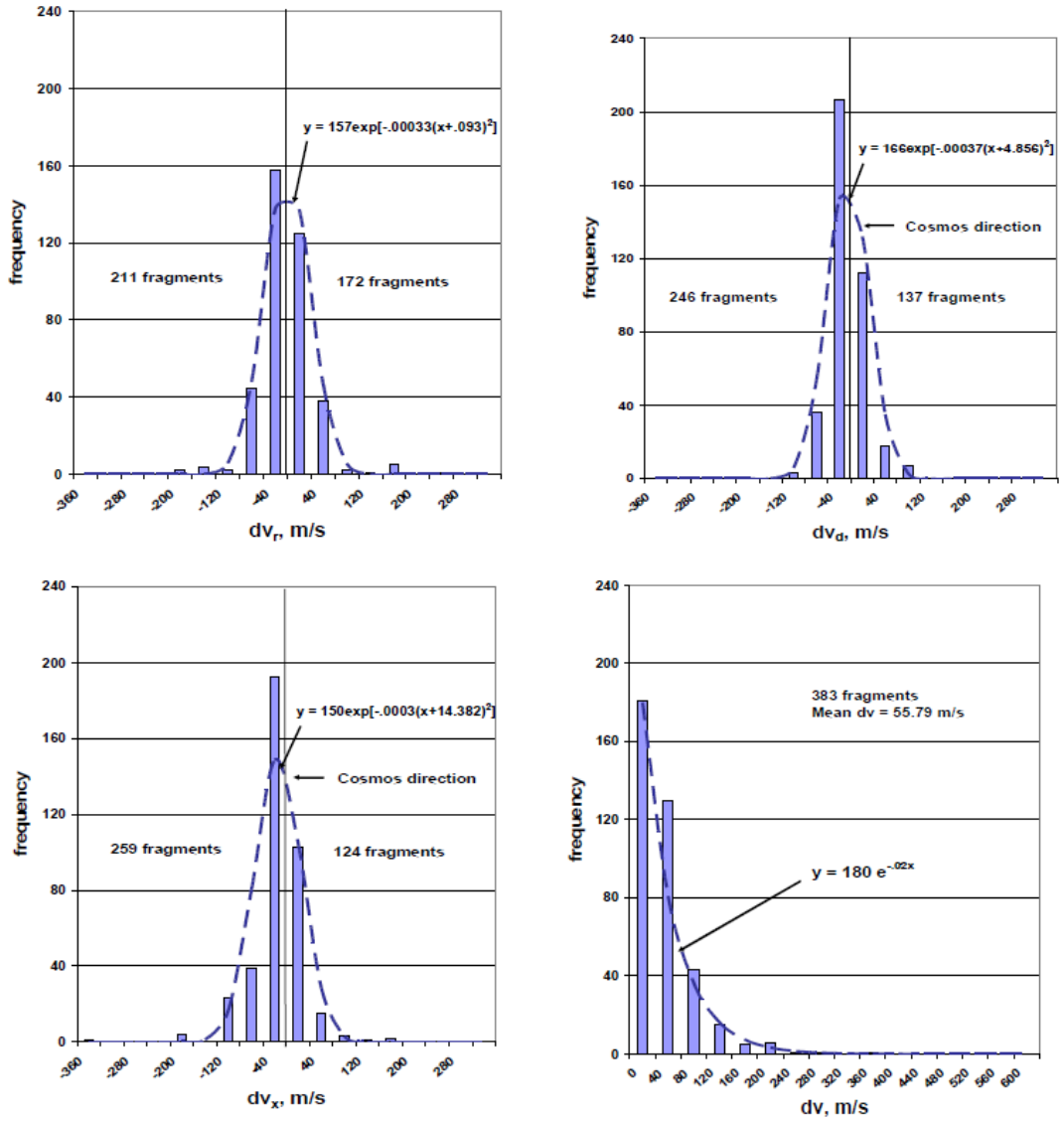


Figure A.3: Histogram plots with fitted normal distribution curve of Iridium 33 fragments $\Delta V$, including components in down-range ($dv_d$), cross-range ($dv_x$) and radial ($dv_r$) directions. The number of fragments with positive and negative $\Delta V$ is also displayed in the plots (Tan et al., 2013).

# B

# PROPAGATOR RESULTS WITH KEPLERIAN EARTH ORBIT

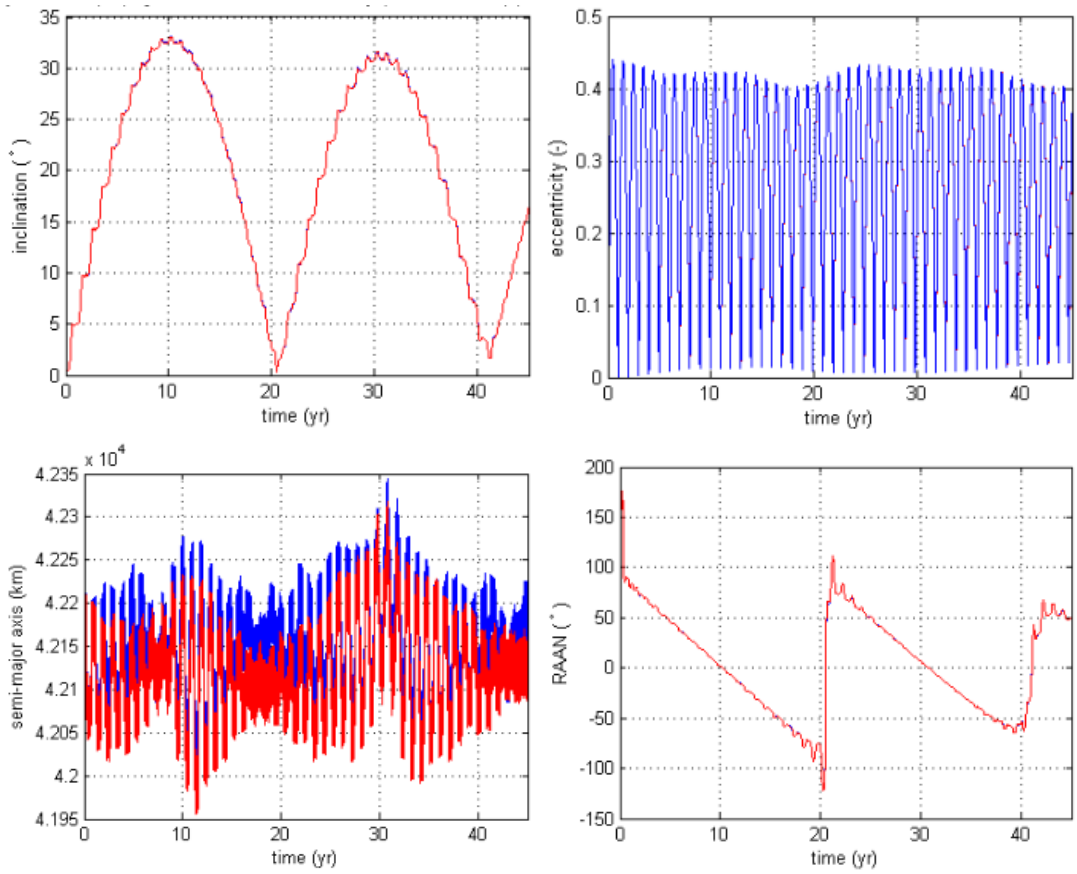


Figure B.1: Non-averaged RK4 propagator results with $J_{2,2}$ and shadow effects included. Comparison of using spice ephemeris (red line) and Keplerian Earth orbit (blue line) for Earth position relative to Sun.

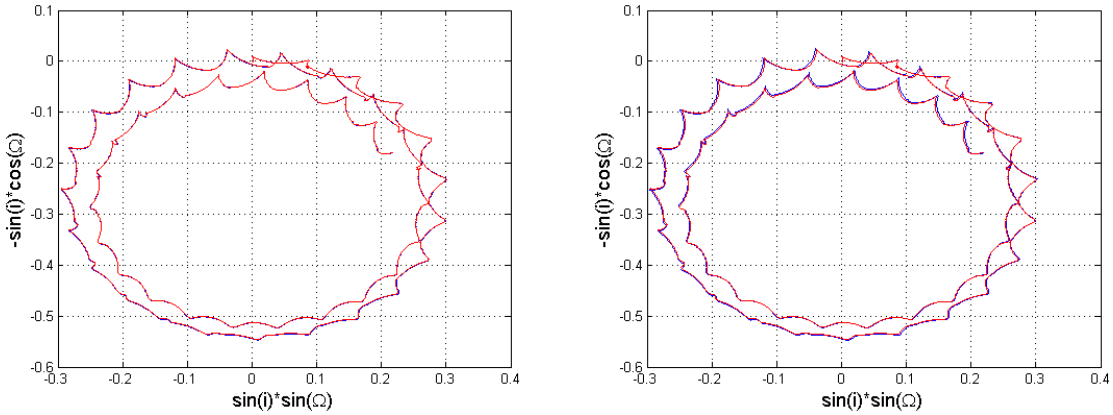


Figure B.2: Non-averaged RK4 propagator results with $J_{2,2}$ and shadow effects included. Comparison of using spice ephemeris (red line) and Keplerian (left) or circular (right) Earth orbit (blue line) for Earth position relative to Sun.

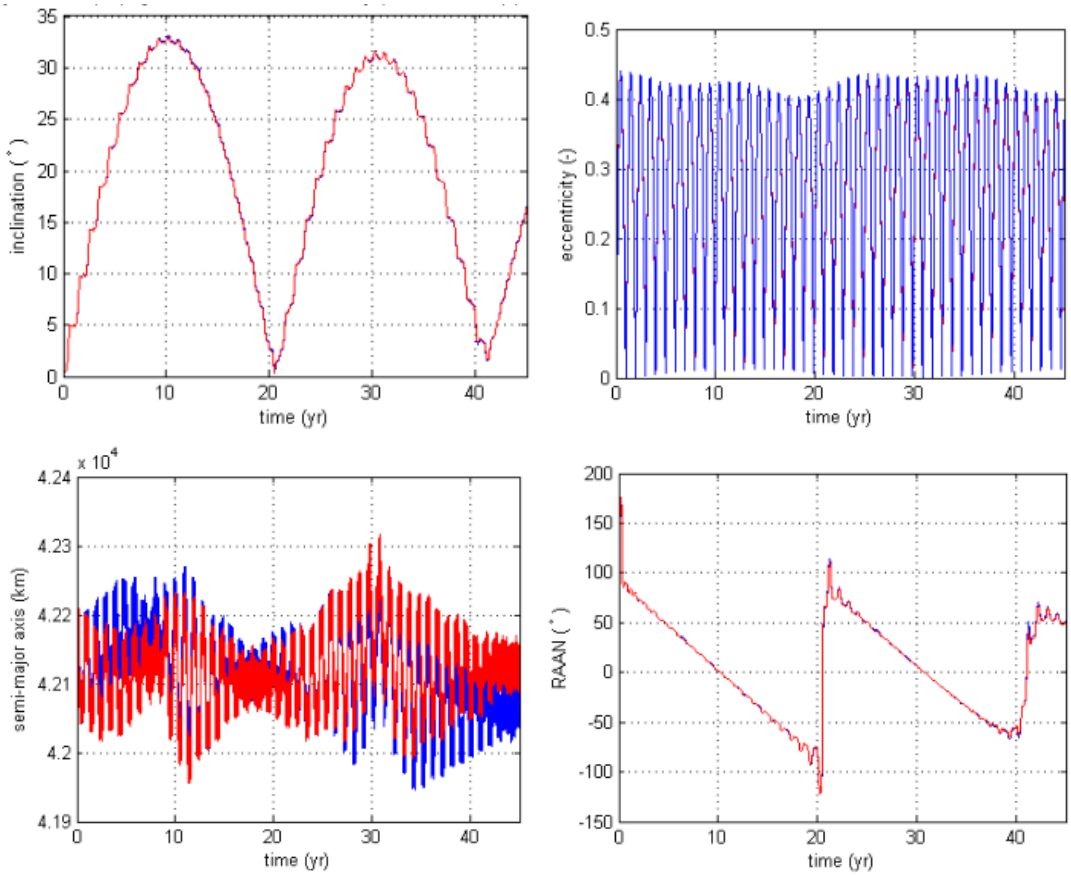


Figure B.3: Non-averaged RK4 propagator results with $J_{2,2}$ and shadow effects included. Comparison of using spice ephemeris (red line) and circular Earth orbit (blue line) for Earth position relative to Sun.

# C

# DOPRI8-RK4 Results Comparison

This Appendix shows a comparison of averaged orbit propagation results using DOPRI8 and RK4 integrators, with the input settings described in Table 5.3 options A and C. The orbital elements evolutions are plotted in Fig. C.1. The curves are nearly identical except for the semi-major axis, where RK4 causes a positive integration error and DOPRI8 a negative one. The differences between the results are up to $5 \cdot 10^{-3}$ km for the semi-major axis. For the inclination evolution the differences are mostly within $2 \cdot 10^{-4}$° with peaks up to $1.2 \cdot 10^{-3}$°. Eccentricity differences are within $5 \cdot 10^{-4}$ and $\Omega$ differences most of the time within $2 \cdot 10^{-3}$° with some peaks up to 0.12°.

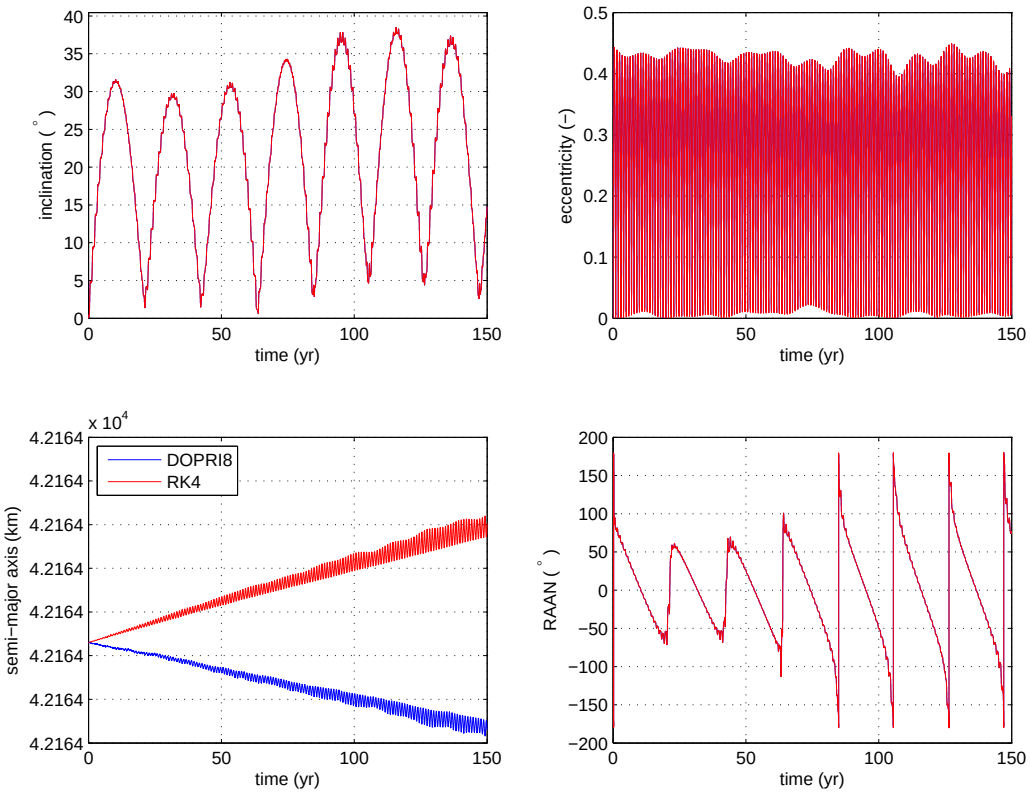


Figure C.1: Comparison of averaged propagator results obtained using DOPRI8 (blue) and RK4 (red) integrators. All plots contain both RK4 and DOPRI8 results, although the blue curves are mostly not visible due to the red curve overlapping them.

# D

# ECCENTRICITY-GEO CROSSINGS FRAGMENTS

This appendix contains the orbit propagation results of 3 fragments selected from the standard explosion test case. Fragment A has a high eccentricity and low number of crossings, while fragment B has a low eccentricity and high number of crossings. Additionally fragment C has zero crossings.

The fragments were shown in the eccentricity-crossings plot of the standard test case in Fig. 6.8 and their characteristics were described in Table 6.3. In this appendix the evolution of the fragments' orbital elements and perigee and apogee are shown for each of the 3 fragments.

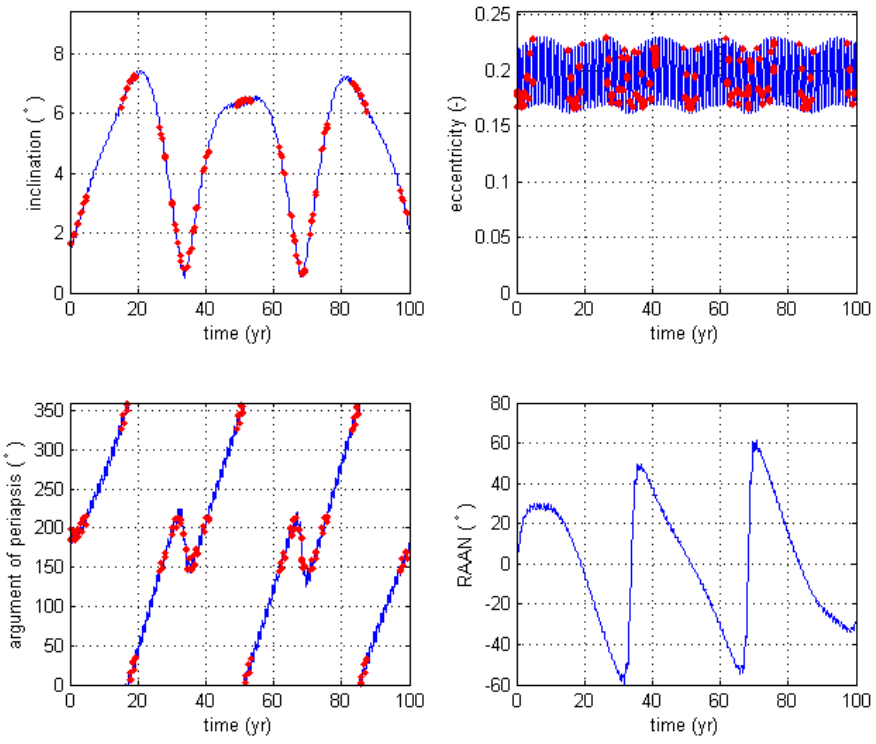


Figure D.1: Orbital element evolution of fragment A. Red dots indicate points in time with crossings.

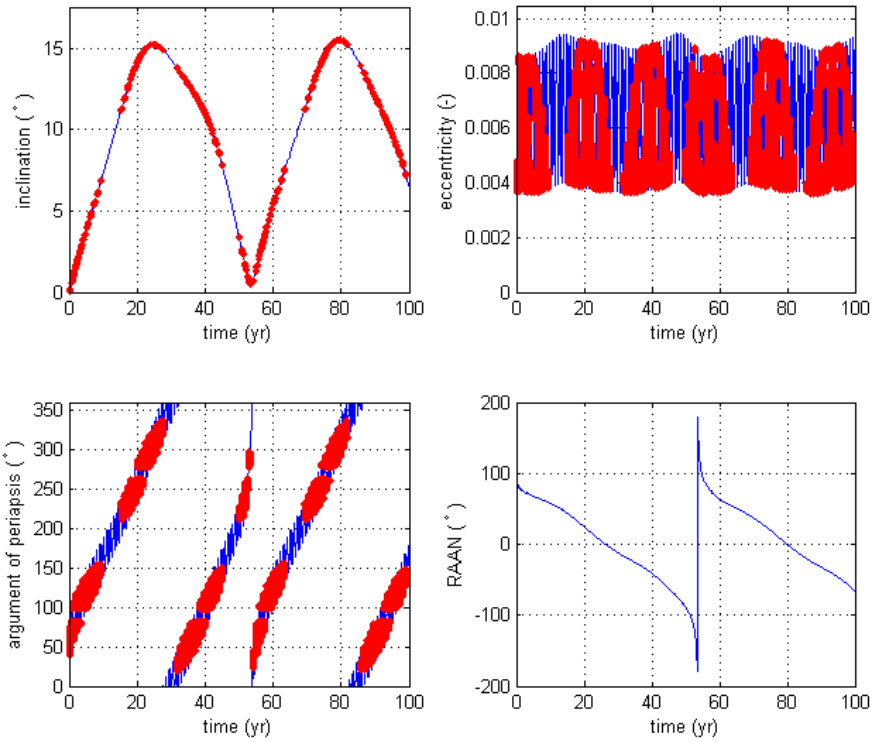


Figure D.2: Orbital element evolution of fragment B. Red dots indicate points in time with crossings

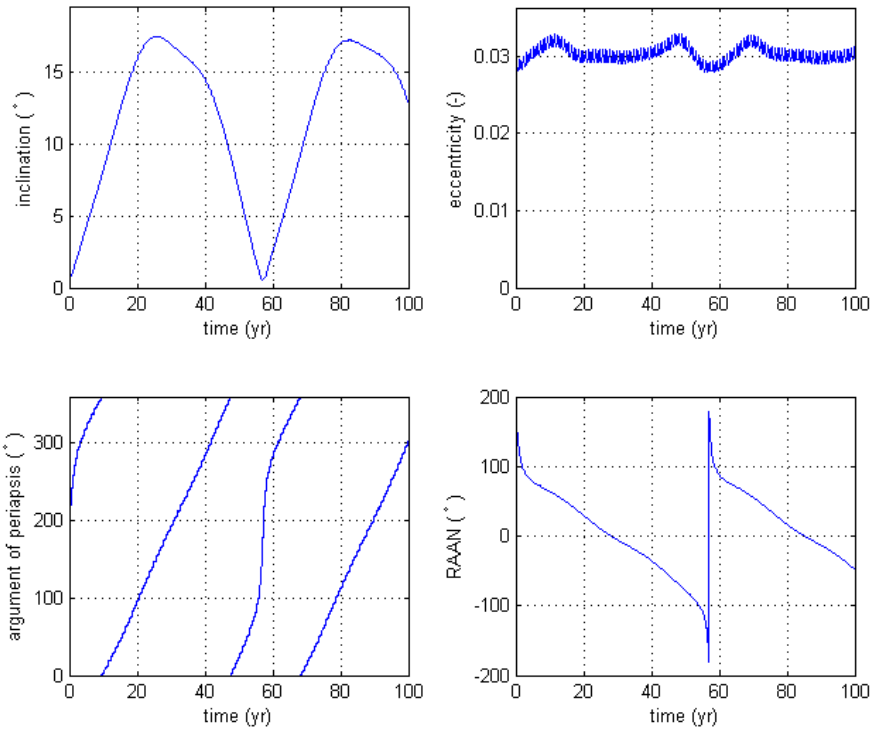


Figure D.3: Orbital element evolution of fragment C. Red dots indicate points in time with crossings

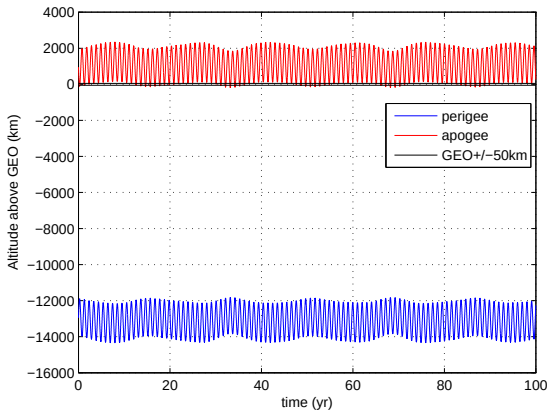


(a) Fragment A

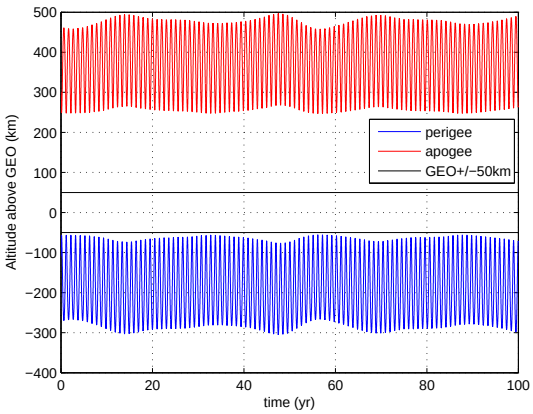


(b) Fragment B

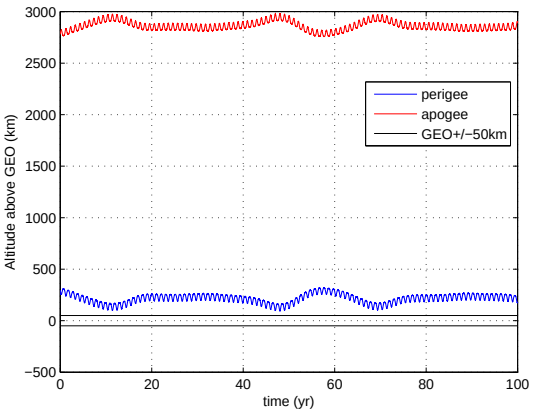


(c) Fragment C

Figure D.4: Apogee and perigee altitude evolution of fragments A, B and C. The altitude is relative to the GEO altitude.

# E

# ECCENTRICITY-GEO CROSSINGS-AMR COLOR PLOTS

This appendix contains eccentricity-crossings plots of the standard explosion and collision test cases, with colors indicating the AMR values. The plots show that the large fragments have both lower AMR and lower eccentricities. Also for the small fragments of the collision test case all of the high eccentricity fragments have high AMR values, while for the other plots the high AMR fragments are more randomly distributed through the plots.

(a) Standard Explosion Test Case

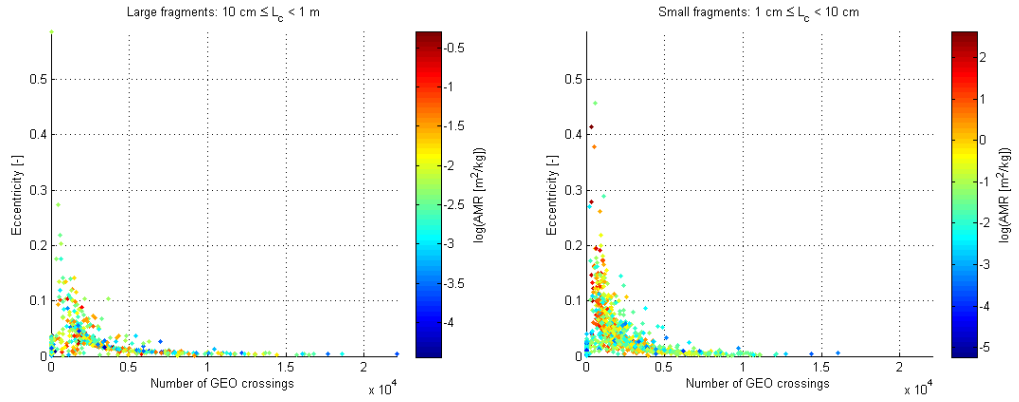


(b) Standard Collision Test Case

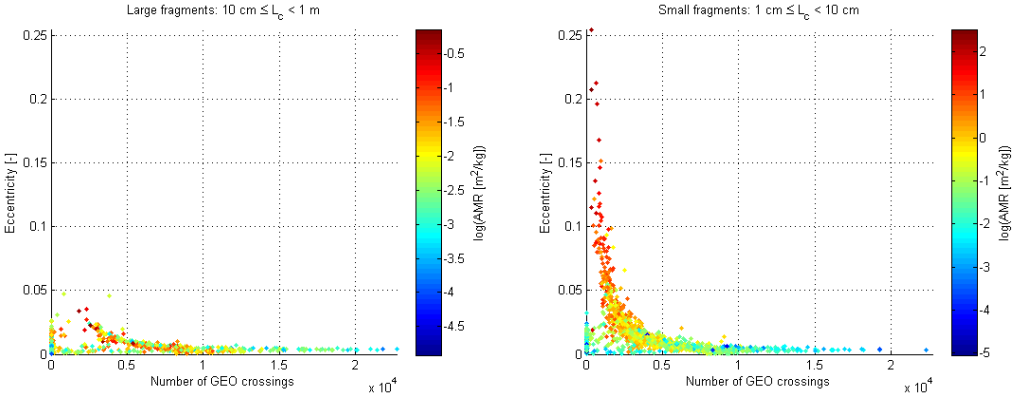


Figure E.1: Eccentricity-crossings plots of standard explosion and collision test cases.

# BIBLIOGRAPHY


R.R. Allan and G.E. Cook. The long-period motion of the plane of a distant circular orbit. Space 52, Royal Aircraft Establishment, 1963.

L. Anselmo and C. Pardini. Long-term dynamical evolution of high area-to-mass ratio debris released into high earth orbits. *Acta Astronautica*, 67(1-2):204–216, July-August 2010. doi: 10.1016/j.actaastro.2009.10.017.

C.C. Chao. Analytical investigation of GEO debris with high area-to-mass ratio. In *AIAA/AAS Astrodynamics Specialist Conference*, 2006.

ESA. Analysis and prediction. online, April 2013. URL `http://www.esa.int/Our_Activities/Operations/Space_Debris/Analysis_and_prediction`. Date accessed: 18 July, 2015.

L.J. Friesen, A.A. Jackson, A.H. Zook, and D.J. Kessler. Analysis of orbital perturbations acting on objects in orbits near geosynchronous earth orbit. *Journal of Geophysical Research*, 97(E3):3845–3863, March 1992. doi: 10.1029/92JE00032.

L.J. Friesen, D.J. Kessler, and H.A. Zook. Reduced debris hazard resulting from a stable inclined geostationary orbit. *Advances in Space Research*, 13(8):231–241, 1993.

T. Hanada. Developing a low-velocity collision model based on NASA standard breakup model. *Space Debris*, 2(4):233–247, 2000. doi: 10.1023/B:SDEB.0000029903.61467.cd.

T. Hanada and J.C. Liou. Comparison of fragments created by low- and hyper-velocity impacts. *Advances in Space Research*, 41(7):1132–1137, 2008. doi: 10.1016/j.asr.2007.05.062.

T. Hanada, T. Yasaka, H. Hata, and Y. Akahoshi. Using NASA standard breakup model to describe low-velocity impacts on spacecraft. *Journal of Spacecraft and Rockets*, 2005. doi: 10.2514/1.11600.

T. Hanada, J.C. Liou, T. Nakajima, and E. Stansbery. Outcome of recent satellite impact experiments. *Advances in Space Research*, 44(5):558–567, 2009a. doi: 10.1016/j.asr.2009.04.016.

T. Hanada, J. Murakami, J.C. Liou, and E. Standbery. Micro-satellite impact tests to investigate multi-layer insulation fragments, 2009b. URL `http://ntrs.nasa.gov/archive/nasa/casi.ntrs.nasa.gov/20090007798.pdf`.

H. Hata, Y. Akahoshi, S. Harada, Y. Kurakazu, T. Hanada, and T. Yasaka. Modifying the NASA standard breakup model to be applied to low-velocity collision. In *54th International Astronautical Congress of the International Astronautical Federation, the International Acadamy of Astronautics, and the International Institute of Space Law*, volume 54. International Astronautical Federation, October 2003. doi: 10.2514/6.IAC-03-IAA.5.2.01.

R. Jehn, V. Agapov, and C. Hernandez. The situation in the geostationary ring. *Advances in Space Research*, 35 (7):1318–1327, 2005. doi: 10.1016/j.asr.2005.03.022.

N.L. Johnson, P.H. Krisko, J.C. Liou, and P.D. Anz-Meador. NASA's new breakup model of evolve 4.0. *Advances in Space Research*, 28(9):1377–1384, 2001. doi: 10.1016/S0273-1177(01)00423-9.

E. Johnston. List of ssatellite in geostationary orbit, 2016. URL `http://www.satsig.net/sslist.htm`. Date accessed: 8 August, 2016.

T.S. Kelso. Analysis of the Iridium 33-Cosmos 2251 collision, 2009. URL `https://celestrak.com/publications/AAS/09-368/AAS-09-368.pdf`. Date accessed: 12 March, 2016.

J. Leloux. Filtering techniques for orbital debris conjunction analysis. Master's thesis, Delft University of Technology, 2012.

A. Lemaitre, N. Delsate, and S. Valk. A web of secondary resonances for large A/m geostationary debris. *Celestial Mechanics and Dynamical Astronomy*, 104:383–402, 2009.

J.C. Liou. Orbital debris modeling, March 2012. URL `http://ntrs.nasa.gov/archive/nasa/casi.ntrs.nasa.gov/20120003286.pdf`. Date accessed: 18 July, 2015.

J.C. Liou and J.K. Weaver. Orbital dynamics of high area-to-mass ratio debris and their distribution in the geosynchronous region. In *Proceedings of the Fourth European Conference on Space Debris*, 2005.

M. Matney, E. Barker, P. Seitzer, K.J. Abercromby, and H.M. Rodriguez. Calculating statistical orbit distributions using GEO optical observations with the Michigan Orbital Debris Survey Telescope (MODEST). In *AIAA 57th International Astronautical Congress*, volume 6, pages 3740–3747. American Institute of Aeronautics and Astronautics, 2006.

C. Pardini and L. Anselmo. Dynamical evolution of debris clouds in geosynchronous orbit. *Advances in Space Research*, 35(7):1303–1312, 2005. doi: 10.1016/j.asr.2005.02.089.

R.C. Reynolds. Review of current activities to model and measure the orbital debris environment in low-earth orbit. *Advances in Space Research*, 10(3-4):(3)359–(3)371, 1990. doi: 10.1016/0273-1177(90)90370-F.

L. Roelen. Satellite fragmentations and the orbit evolution of debris in an inclined GEO disposal orbit, MSc Literature Study (AE4020), Delft University of Technology, 2015.

A.J. Rosengren and D.J. Scheeres. Long-term dynamics of high area-to-mass ratio objects in high-earth orbit. *Advances in Space Research*, 52(8):1545–1560, October 2013. doi: 10.1016/j.asr.2013.07.033.

A.J. Rosengren and D.J. Scheeres. On the Milankovitch orbital element for perturbed Keplerian motion. *Celestial Mechanics and Dynamical Astronomy*, 118(3):197–220, March 2014. doi: 10.1007/s10569-013-9530-7.

A.J. Rosengren, D.J. Scheeres, and J.W. McMahon. The classical Laplace plane as a stable disposal orbit for geostationary satellites. *Advances in Space Research*, 53(8):1219–1228, April 2014. doi: 10.1016/j.asr.2014.01.034.

T. Schildknecht, R. Musci, M. Ploner, G. Beutler, W. Flury, J. Kuusela, J. de Leon Cruz, and L. de Fatima Dominguez Palmero. Optical observations of space debris in GEO and in high-eccentric orbits. *Advances in Space Research*, 34:901–911, 2004.

L. Shengwei, L. Sen, L. Yi, and H. Jie. Recent progress on satellite breakup model. *Journal of Experiments in Fluid Dynamics*, 28(2), April 2014. doi: 10.11729/syltlx2014pz34.

S.Y. Su and D.J. Kessler. Contribution of explosion and future collision fragments to the orbital debris environment. *Advances in Space Research*, 5(2):25–34, 1985. doi: 10.1016/0273-1177(85)90384-9.

A. Tan, T.X. Zhang, and M. Dokhanian. Analysis of the Iridium 33 and Cosmos 2251 collision using velocity perturbations of the fragments. *Advances in Aerospace Science and Applications*, 3(1):13–25, 2013.

K.F. Wakker. *AE4-874I lecture notes: Astrodynamics-I*. TU Delft, 2010a.

K.F. Wakker. *AE4-874II lecture notes: Astrodynamics-II*. TU Delft, 2010b.

J.R. Wertz. *Orbit & Constellation Design & Management*. Microcosm Press, 2009.

B.T.C. Zandbergen. lecture notes ae1222-ii: Aerospace design & systems engineering elements i: Part: Spacecraft (bus) design and sizing, November 2015.